



## Namensnennung-Keine kommerzielle Nutzung-Keine Bearbeitung 2.5 Schweiz

---

### Sie dürfen:



das Werk vervielfältigen, verbreiten und öffentlich zugänglich machen

### Zu den folgenden Bedingungen:



**Namensnennung.** Sie müssen den Namen des Autors/Rechteinhabers in der von ihm festgelegten Weise nennen (wodurch aber nicht der Eindruck entstehen darf, Sie oder die Nutzung des Werkes durch Sie würden entlohnt).



**Keine kommerzielle Nutzung.** Dieses Werk darf nicht für kommerzielle Zwecke verwendet werden.



**Keine Bearbeitung.** Dieses Werk darf nicht bearbeitet oder in anderer Weise verändert werden.

- Im Falle einer Verbreitung müssen Sie anderen die Lizenzbedingungen, unter welche dieses Werk fällt, mitteilen. Am Einfachsten ist es, einen Link auf diese Seite einzubinden.
- Jede der vorgenannten Bedingungen kann aufgehoben werden, sofern Sie die Einwilligung des Rechteinhabers dazu erhalten.
- Diese Lizenz lässt die Urheberpersönlichkeitsrechte unberührt.

#### Die gesetzlichen Schranken des Urheberrechts bleiben hiervon unberührt.

Die Commons Deed ist eine Zusammenfassung des Lizenzvertrags in allgemeinverständlicher Sprache: <http://creativecommons.org/licenses/by-nc-nd/2.5/ch/legalcode.de>

#### Haftungsausschluss:

Die Commons Deed ist kein Lizenzvertrag. Sie ist lediglich ein Referenztext, der den zugrundeliegenden Lizenzvertrag übersichtlich und in allgemeinverständlicher Sprache wiedergibt. Die Deed selbst entfaltet keine juristische Wirkung und erscheint im eigentlichen Lizenzvertrag nicht. Creative Commons ist keine Rechtsanwalts-gesellschaft und leistet keine Rechtsberatung. Die Weitergabe und Verlinkung des Commons Deeds führt zu keinem Mandatsverhältnis.

Electronic Spectroscopy of  
Transient Molecules by  
Mass-Selected  
Resonance Enhanced  
Multi-Photon Ionization

Inauguraldissertation zur  
Erlangung der Würde eines Doktors der Philosophie  
vorgelegt der  
Philosophisch-Naturwissenschaftliche Fakultät  
der Universität Basel

vorgelegt von

Varun Gupta

aus

Kanpur, Indien

Basel, 2013

Referent: Prof. Dr. John P. Maier

Korreferent: Prof. Dr. Stefan Willitsch

Genehmigt von der Philosophisch-Naturwissenschaftliche Fakultät  
auf Antrag von  
Prof. Dr. John P. Maier und Prof. Dr. Stefan Willitsch

Basel, den 26.03.2013

Prof. Dr. Jörg Schibler

*Dedicated to my parents  
for their endless love, support  
and encouragement.*

# Acknowledgement

This work would not have been possible without the guidance and support of several individuals. First and foremost, I would like to thank Prof. Dr. John P. Maier for this great opportunity to work in his research group, and his support and guidance throughout my doctoral studies.

I would like to thank Prof. Dr. Stefan Willitsch for being the co-referee of my thesis. Prof. Thomas Pfohl is thanked for agreeing to chair my Ph.D. defence.

Special thanks to Prof. Dr. Timothy C. Steimle and his group for the wonderful collaboration we had on transition-metal dioxides. It was great to work with him during his two visits to Basel.

Words are not enough to thank Dr. Corey A. Rice who has been a constant source of support and encouragement throughout my doctoral studies. I would also like to thank Dr. Ramya Nagarajan, Dr. Fabio J. Mazzotti and Dr. Lindsay N. Zack for their help and guidance. Dr. Satrajit Chakrabarty, Dr. Adam Nagy, Dr. Iryna Garkusha-Roth, Dr. Bohan Wu, Dr. Rainer Dietsche and Mr. Mathias Holz are thanked for all the scientific and non-scientific discussions we had over the years.

Many people made my life much easier during the course of my studies. I would like to thank Dr. Anatoly Johnson for his assistance with the lasers, Mr. Georg Holderield for his help with the electronics and Mr. Jacques Lecoultre for taking care of all the chemicals. Further, Mr. Grischa Martin, Mr. Philipp Knöpfel and Mr. Dieter Wild from the mechanical workshop are thanked for construction and maintenance of various scientific devices. I would also like to thank Ms. Maya Greuter and Ms. Daniela Tischauser for taking care of all the administrative mat-

ters. The Swiss National Science Foundation and the University of Basel are thanked for financial support.

I would take this opportunity to thank all the wonderful teachers and professors who have shaped my life at some point or another; Dr. Rakesh K. Pandey, Prof. Dr. Sheenu Thomas, Prof. Dr. Deepthy Menon and Prof. Dr. Raj K. Thareja deserve special mention.

I thank all my friends in India and Switzerland for being there for me through good and bad times. I thank Mr. Adil Masood for being a good friend and for all these hours of discussions we had about anything and everything. Dr. Ranjini Raghunandan is thanked for being a great person that she has been for close to a decade, I have known her. Many thanks to Ms. Natalja Strelnikova for her support and encouragement. If not for her, writing this thesis would have taken a lot more time than it did.

Finally, I would like to thank my parents for being my ultimate source of affection and inspiration. A special thanks goes to my sister, Shanuli, for her support and understanding.

# Contents

<b>Acknowledgement</b>	<b>ix</b>
<b>1 Introduction</b>	<b>1</b>
Bibliography . . . . .	6
<b>2 Background</b>	<b>17</b>
2.1 Electronic Spectroscopy . . . . .	17
2.1.1 Molecular Orbitals . . . . .	18
2.1.2 Vibrational Structure . . . . .	19
2.1.2.1 Herzberg-Teller Effect . . . . .	21
2.1.2.2 Jahn-Teller Effect . . . . .	22
2.1.2.3 Renner-Teller Effect . . . . .	23
2.1.3 Rotational Structure . . . . .	24
2.1.4 Fine Structure . . . . .	24
2.2 Multiphoton Spectroscopy . . . . .	24
2.2.1 Resonant Absorption . . . . .	25
2.2.2 Resonance Enhanced Multiphoton Ionization . . . . .	26
2.2.2.1 One-Color Two-Photon Scheme . . . . .	27
2.2.2.2 Two-Color Two-Photon Scheme . . . . .	27
2.2.2.3 Multiphoton Schemes . . . . .	27
2.3 Supersonic Free Jet Expansion . . . . .	28
2.4 Time-of-Flight Mass Spectrometry . . . . .	28
Bibliography . . . . .	31



<b>3</b>	<b>Experimental</b>	<b>33</b>
3.1	Molecular Sources . . . . .	34
3.1.1	Ablation Source . . . . .	34
3.1.2	Discharge Source . . . . .	35
3.2	Vacuum System . . . . .	37
3.3	Light Sources . . . . .	37
3.4	Time-of-Flight Mass Spectrometer . . . . .	39
3.5	Ion Detection . . . . .	39
3.6	Electrical Arrangement . . . . .	40
3.7	Data Handling . . . . .	42
	Bibliography . . . . .	43
<b>4</b>	<b>Silver monosulfide</b>	<b>45</b>
4.1	Experimental . . . . .	45
4.2	Calculations . . . . .	46
4.3	Results . . . . .	46
4.3.1	Electronic transitions in the near-infrared . . . . .	47
4.3.2	Electronic transitions in the ultraviolet . . . . .	52
4.4	Discussion . . . . .	57
4.5	Conclusion . . . . .	60
	Bibliography . . . . .	61
<b>5</b>	<b>Titanium dioxide</b>	<b>63</b>
5.1	Experimental . . . . .	65
5.2	Results and discussion . . . . .	66
5.2.1	Electronic transitions in the visible . . . . .	66
5.2.2	Electronic transitions in the ultraviolet . . . . .	71
5.3	Conclusion . . . . .	72
	Bibliography . . . . .	73
<b>6</b>	<b>Zirconium dioxide</b>	<b>77</b>
6.1	Experimental . . . . .	78

---

6.2	Results and discussion . . . . .	78
6.2.1	Electronic transitions in the visible . . . . .	78
6.2.2	Electronic transitions in the ultraviolet . . . . .	82
6.3	Conclusion . . . . .	85
	Bibliography . . . . .	87
<b>7</b>	<b>Silicon Trimer</b>	<b>89</b>
7.1	Experimental . . . . .	90
7.2	Results and discussion . . . . .	91
7.2.1	The triplet $D_{3h}$ system . . . . .	91
7.2.2	The singlet $D_{3h}/C_{2v}$ system . . . . .	93
7.3	Conclusion . . . . .	95
	Bibliography . . . . .	96
<b>8</b>	<b>Carbon chains, <math>C_n</math> (<math>n = 6 - 9</math>)</b>	<b>101</b>
8.1	Experimental . . . . .	102
8.2	Results and discussion . . . . .	103
8.2.1	$(2)^3\Sigma_u^- - X^3\Sigma_g^-$ electronic transition of $C_6$ and $C_8$ . . . . .	103
8.2.2	$^1\Sigma_u^+ - X^1\Sigma_g^+$ electronic transition of $C_7$ and $C_9$ . . . . .	106
8.3	Conclusion . . . . .	107
	Bibliography . . . . .	108
<b>9</b>	<b>Conclusion</b>	<b>113</b>
	Bibliography . . . . .	116
	<b>Curriculum Vitae</b>	<b>119</b>



# List of Figures

1.1	Regions of the electromagnetic spectrum. . . . .	1
2.1	Schematic of energy levels for a diatomic molecule. . . . .	18
2.2	Schematic of Jahn-Teller distortion along a doubly degenerate vibration coordinate. . . . .	22
2.3	Schematic of Renner-Teller distortion along a doubly degenerate vibration coordinate. . . . .	23
2.4	Level schemes for <b>(A)</b> resonant and <b>(B)</b> non-resonant two photon transitions. . . . .	26
3.1	The experimental setup. . . . .	33
3.2	Ablation source. . . . .	34
3.3	Mass spectrum of titanium ablation in the presence of 5%O <sub>2</sub> /He at 7.9 eV ionization energy. . . . .	35
3.4	Discharge source. . . . .	36
3.5	Micro channel plate detector. . . . .	40
3.6	Electrical arrangement of the experiment. . . . .	41
4.1	<b>(A)</b> Mass-selected [1+1'] resonance enhanced multiphoton ionization spectrum of the $A^2\Sigma^+ - X^2\Pi_i$ electronic transition of $^{107}\text{Ag}^{32}\text{S}$ at $5\text{ cm}^{-1}$ resolution; <b>(B)</b> The $\Omega'' = 3/2$ component of the 0-0 and 1-0 transitions along with the sequence bands, recorded with $0.15\text{ cm}^{-1}$ laser bandwidth. . . . .	48

4.2	The $\Omega'' = 3/2$ component of the $A^2\Sigma^+ - X^2\Pi$ 0–0 transition of $^{107}\text{Ag}^{32}\text{S}$ . The lower trace shows the simulation at 80 K rotational temperature with Gaussian and Lorentzian line widths of $0.12\text{ cm}^{-1}$ and $0.06\text{ cm}^{-1}$ , respectively. . . . .	50
4.3	The $\Omega'' = 3/2$ component of the $A^2\Sigma^+ - X^2\Pi$ 1–0 transition of $^{107}\text{Ag}^{32}\text{S}$ . The lower trace shows the simulation with the same parameters as Figure 4.2. . . . .	52
4.4	Mass-selected $[1+1']$ resonance enhanced multi-photon ionization spectrum of $^{107}\text{Ag}^{32}\text{S}$ in the <b>(A)</b> 25 000 - 27 000 $\text{cm}^{-1}$ region, recorded with $8\text{ cm}^{-1}$ laser bandwidth; <b>(B)</b> 25 515 - 26 215 $\text{cm}^{-1}$ region, recorded with $0.15\text{ cm}^{-1}$ laser bandwidth. . . . .	54
4.5	Mass-selected $[1+1']$ resonance enhanced multi-photon ionization spectrum of $^{107}\text{Ag}^{32}\text{S}$ in the 28 500 - 31 500 $\text{cm}^{-1}$ region. . . . .	55
4.6	Mass-selected $[1+1']$ resonance enhanced multi-photon ionization spectrum of $^{107}\text{Ag}^{32}\text{S}$ in the 34 500 - 37 500 $\text{cm}^{-1}$ region. . . . .	56
4.7	Mass-selected $[1+1']$ resonance enhanced multi-photon ionization spectrum of $^{107}\text{Ag}^{32}\text{S}$ in the 38 000 - 40 500 $\text{cm}^{-1}$ region. . . . .	58
4.8	Mass-selected $[1+1']$ resonance enhanced multi-photon ionization spectrum of $^{107}\text{Ag}^{32}\text{S}$ in the 40 500 - 47 500 $\text{cm}^{-1}$ region. . . . .	59
5.1	Mass-selected $[1+1']$ resonance enhanced multi-photon ionization spectra of the $A^1B_2 - X^1A_1$ electronic transition of <b>(A)</b> $^{48}\text{Ti}^{16}\text{O}_2$ ; <b>(B)</b> $^{48}\text{Ti}^{18}\text{O}_2$ . . . . .	66
5.2	Assignment for the $A^1B_2(\nu_1, \nu_2, \nu_3) - X^1A_1(0, 0, 0)$ electronic transition of $^{48}\text{Ti}^{16}\text{O}_2$ . . . . .	69
5.3	Mass-selected $[1+1']$ resonance enhanced multi-photon ionization spectrum of the $C^1B_2(\nu_1, \nu_2, \nu_3) - X^1A_1(0, 0, 0)$ electronic transition of $^{48}\text{Ti}^{16}\text{O}_2$ . . . . .	70
6.1	Mass-selected $[1+1']$ resonance enhanced multi-photon ionization spectrum of the $A^1B_2 - X^1A_1$ electronic transition of $^{90}\text{Zr}^{16}\text{O}_2$ . . . . .	80

6.2	The rotational contours for the $A^1B_2(0,0,0) - X^1A_1(0,0,0)$ transition of <b>(A)</b> $^{90}\text{Zr}^{16}\text{O}_2$ ; <b>(B)</b> $^{91}\text{Zr}^{16}\text{O}_2$ ; <b>(C)</b> $^{92}\text{Zr}^{16}\text{O}_2$ ; <b>(D)</b> $^{94}\text{Zr}^{16}\text{O}_2$ .	81
6.3	The rotational contours for the $A^1B_2(0,0,3) - X^1A_1(0,0,0)$ transition of <b>(A)</b> $^{90}\text{Zr}^{16}\text{O}_2$ ; <b>(B)</b> $^{91}\text{Zr}^{16}\text{O}_2$ ; <b>(C)</b> $^{92}\text{Zr}^{16}\text{O}_2$ ; <b>(D)</b> $^{94}\text{Zr}^{16}\text{O}_2$ .	82
6.4	Mass-selected $[1+1']$ resonance enhanced multi-photon ionization spectrum of $^{90}\text{Zr}^{16}\text{O}_2$ in the 23 000 $\text{cm}^{-1}$ to 35 000 $\text{cm}^{-1}$ region. . .	83
6.5	Assignment for the $B^1A_1(\nu_1, \nu_2, \nu_3) - X^1A_1(0, 0, 0)$ electronic transition of $^{90}\text{Zr}^{16}\text{O}_2$ . . . . .	85
6.6	Assignment for the $G^1B_2(\nu_1, \nu_2, \nu_3) - X^1A_1(0, 0, 0)$ electronic transition of $^{90}\text{Zr}^{16}\text{O}_2$ . . . . .	86
7.1	Mass-selected $[1+1']$ resonance enhanced multi-photon ionization spectrum of $\text{Si}_3$ in the 17 000 - 21 500 $\text{cm}^{-1}$ region. . . . .	92
7.2	The $^1B_1 - ^1A_1$ and $^1A_2 - ^1A_1$ transition of $\text{Si}_3$ in $C_{2v}$ geometry, observed in <b>(A)</b> neon matrix [18]; <b>(B)</b> gas phase. The triplet transitions in gas phase spectrum are marked with an asterisk (*). . .	94
8.1	Time-of-flight mass spectrum of laser ablated graphite, recorded using a 10.5 eV ionization source. . . . .	102
8.2	$(2)^3\Sigma_u^- - X^3\Sigma_g^-$ electronic spectrum of linear $\text{C}_6$ in the gas phase measured by $[1+1]$ resonance enhanced multiphoton ionization method using 30 ps laser. . . . .	103
8.3	$(2)^3\Sigma_u^- - X^3\Sigma_g^-$ electronic spectrum of linear $\text{C}_8$ in the gas phase measured by $[1+1]$ resonance enhanced multiphoton ionization method using a 30 ps laser. . . . .	104
8.4	$^1\Sigma_u^+ - X^1\Sigma_g^+$ electronic spectrum of linear $\text{C}_7$ measured by $[1+1]$ resonance enhanced multiphoton ionization method using a 30 ps laser. . . . .	105
8.5	$^1\Sigma_u^+ - X^1\Sigma_g^+$ electronic spectrum of linear $\text{C}_9$ measured by $[1+1]$ resonance enhanced multiphoton ionization method using a 30 ps laser. . . . .	106



# List of Tables

4.1	Calculated spectroscopic constants for low-lying electronic states of AgS at the MCSCF-SBKJC level of theory. . . . .	46
4.2	Band maxima and isotopic shifts (in $\text{cm}^{-1}$ ) for the $A^2\Sigma^+ - X^2\Pi$ electronic transition of $^{107}\text{Ag}^{32}\text{S}$ , $^{109}\text{Ag}^{32}\text{S}$ and $^{109}\text{Ag}^{34}\text{S}$ . . . . .	49
4.3	Vibrational constants (in $\text{cm}^{-1}$ ) for the $X^2\Pi$ and $A^2\Sigma^+$ states of AgS. . . . .	49
4.4	Molecular constants (in $\text{cm}^{-1}$ ) for the $X^2\Pi$ and $A^2\Sigma^+$ states of AgS. . . . .	53
4.5	Band maxima (in $\text{cm}^{-1}$ ) for the observed ultraviolet transition of $^{107}\text{Ag}^{32}\text{S}$ . . . . .	57
5.1	Band maxima and isotopic shifts (in $\text{cm}^{-1}$ ) for the $A^1B_2(\nu_1, \nu_2, \nu_3) - X^1A_1(0,0,0)$ electronic transition of $^{48}\text{Ti}^{16}\text{O}_2$ and $^{48}\text{Ti}^{18}\text{O}_2$ . . . . .	68
5.2	Vibrational parameters (in $\text{cm}^{-1}$ ) for the $A^1B_2$ state of $^{48}\text{Ti}^{16}\text{O}_2$ . . . . .	69
5.3	Band maxima (in $\text{cm}^{-1}$ ) for the $C^1B_2(\nu_1, \nu_2, \nu_3) - X^1A_1(0,0,0)$ electronic transition of $^{48}\text{Ti}^{16}\text{O}_2$ . . . . .	71
6.1	Band maxima (in $\text{cm}^{-1}$ ) for the $A^1B_2(\nu_1, \nu_2, \nu_3) - X^1A_1(0,0,0)$ electronic transition of $^{90}\text{Zr}^{16}\text{O}_2$ . . . . .	79
6.2	Vibrational parameters (in $\text{cm}^{-1}$ ) for the $A^1B_2$ state of $^{90}\text{Zr}^{16}\text{O}_2$ . . . . .	80
6.3	Band maxima (in $\text{cm}^{-1}$ ) for the $B^1A_1(\nu_1, \nu_2, \nu_3) - X^1A_1(0,0,0)$ electronic transition of $^{90}\text{Zr}^{16}\text{O}_2$ . . . . .	84
6.4	Band maxima (in $\text{cm}^{-1}$ ) for the $G^1B_2(\nu_1, \nu_2, \nu_3) - X^1A_1(0,0,0)$ electronic transition of $^{90}\text{Zr}^{16}\text{O}_2$ . . . . .	85



7.1	Band maxima (in $\text{cm}^{-1}$ ) for the ${}^3A_1'' - {}^3A_2'$ electronic transition of ${}^{28}\text{Si}_3$ . . . . .	93
7.2	Band maxima (in $\text{cm}^{-1}$ ) for transitions of $\text{Si}_3$ observed in the singlet manifold. . . . .	95

# 1 Introduction

Spectroscopy has made an outstanding contribution to the present state of our understanding about the structure of atoms and molecules. In the case of molecules, details about the geometry, conformation and even accurate values of bond lengths and bond angles can be obtained from their spectra. This information can be derived from the absorption or emission spectra, which are generated on interaction of electromagnetic radiation with matter. Based on the frequency of the electromagnetic radiation used, different kinds of information can be obtained as a result of such interactions, as can be seen in Figure 1.1. Molecules may undergo rotational, vibrational, electronic or ionization processes, in order of increasing energy. They may also scatter light in a Raman process.

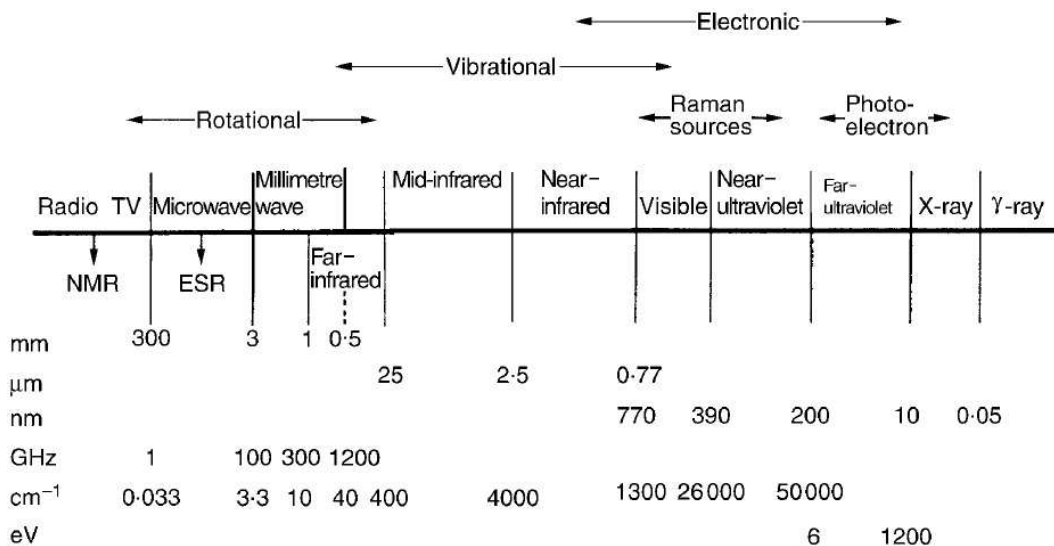


Figure 1.1: Regions of the electromagnetic spectrum.

Most of our knowledge about the universe comes from analysis of electromagnetic radiation coming from the space. Spectroscopy is the means used to determine the chemical composition and physical conditions in distant stars and interstellar clouds. It also enables us to measure the rate of expansion of the universe, the mass of a galaxy, the masses of two stars in orbit about each other, the dark matter content of galaxies, discover a black hole or an exoplanet around other stars, all using the Doppler shift.

The roots of modern spectroscopy go back to 1666, when Issac Newton first demonstrated that sunlight passing through a prism could be dispersed into a continuous series of colours, similar to the rainbow [1]. However, the first major breakthrough came 150 years later, when Joseph von Fraunhofer observed a large number of fine dark lines in the solar spectrum [2]. This phenomenon was not understood until the work of Gustav Kirchhoff and Robert Bunsen [3] in the 1850s. Armed with the theory of absorption and emission and knowledge that each atom and molecule produced a unique and characteristic spectrum, they proposed that these lines were due to the selective absorption of a continuous spectrum produced by the hot interior of the sun by cooler gases at the surface; hence laying the foundations of modern spectroscopy.

The quantum leap however came with the development of lasers. With the kind of impact lasers have made in spectroscopy, it would not be wrong to call them as "The Light of Knowledge". Many experiments which could not be carried out before, because of lack of intensity or insufficient resolution, are now readily done with lasers. Laser lines span the whole spectral range from the vacuum-ultraviolet to the far-infrared region. Of particular interest are the continuously tunable lasers, which in combination with frequency mixing techniques provide a light source at any desired wavelength above 100 nm. The development of tunable lasers in UV/Vis region has provided the means to study the electronic processes taking place in atoms and molecules. Another big leap in spectroscopy came from the advancements made in supersonic free jet expansion technology. Together with a molecular source like electric discharge [4] or laser ablation source [5], it provides an effective way to produce isolated transient molecules at very low

---

temperatures. The resulting spectra are less congested due to low population of excited rovibronic levels and reduced Doppler broadening at lower temperatures, and hence easier to interpret. Multiphoton ionization method coupled with a time-of-flight mass spectrometer can be utilised for sensitive detection of molecules of desired mass. Combined together with lasers and a suitable molecular source, it provides a powerful technique to study the electronic transitions in the desired molecule. Chapter 2 gives a theoretical background about the processes discussed here, whereas Chapter 3 focuses on the details of the experimental set-up.

Transition-metal sulfides play an important role in various biological and industrial applications [6–9] and have also been of astronomical interest since the discovery of TiS [10], YS [11], and ZrS [12] in S-type Mira variable stars. There have been relatively few studies on their electronic transitions when compared to the isoelectronic monoxides [13, 14]. Moreover, these investigations have been mostly directed towards the  $3d$  transition metal monosulfides [15–23]. In the case of  $4d$  transition metals, electronic transitions have been studied only for the monosulfides of yttrium [24–26], zirconium [27–30], niobium [31, 32] and rhodium [33]. The first gas phase detection of silver monosulfide, along with the analysis of the observed electronic transitions is presented in Chapter 4.

Titanium dioxide is of importance in various industrial and technological applications. It is the most widely used white pigment because of its brightness, high refractive index, UV absorbing capabilities and resistance to discolouration, and has applications in paints, coatings, plastics, papers, inks, foods, medicine, sunscreen etc. [34]. As a thin film, its refractive index and colour make it an excellent reflective optical coating for dielectric mirrors [35].  $\text{TiO}_2$  is a photocatalyst under UV radiation and its catalytic activity can be extended to the visible by doping with other metals [36]. Thin films of  $\text{TiO}_2$  are a major component of dye-sensitized solar cells [37]. It is also used as a large bandgap material in the semiconductor industry. Titanium containing molecules are of interest to astrochemists as it is one of the more abundant transition metals in space [38].  $\text{TiO}$  [39] and  $\text{TiH}$  [40] have been detected in atmospheres of cool M-type stars;  $\text{TiO}$  being the main opacity source in the atmospheres of these stars in the visible and near

infrared [41].  $\text{TiO}_2$  is believed to play an important role in dust formation processes in circumstellar shells of oxygen-rich stars [42]. Recently, there has been a detection of  $\text{TiO}_2$  in the oxygen-rich circumstellar shell around the late M-type supergiant star VY Canis Majoris via rotational transitions [43]. There are many unidentified emission features towards VY Canis Majoris in the optical region [44] and  $\text{TiO}_2$  is considered as a potential carrier for some of these [45]. Given this diverse interest, electronic spectra of  $\text{TiO}_2$  have been recorded and analysed, the details of which are provided in Chapter 5.

Going down the group, just below titanium, there is zirconium.  $\text{ZrO}_2$  has attracted attention in recent years due to its interesting properties and is being used for many engineering and industrial applications. Because of its high thermal stability, it is widely used in the production of ceramics [46]. Its high ionic conductivity (and a low electronic conductivity) makes it one of the most useful electroceramics [46]. Its high mechanical stability and resistance to abrasion makes it an ideal candidate for use as protective coating on particles of titanium dioxide pigments [46]. Due to its high refractive index, as a refractory material, it has many applications similar to titanium dioxide. It is also a high-k dielectric material [47] with potential applications as an insulator in transistors.  $\text{ZrO}_2$  is also a molecule of astrophysical interest as the monoxide,  $\text{ZrO}$  is an important component in atmospheres of certain late type stars [48,49].  $\text{ZrO}$  has considerable significance in distinguishing M and S-type stars [50], as it is one of the main absorption features in the spectra of S-type stars. In stars with a very high mass loss rate,  $\text{ZrO}_2$  clusters may form in large enough quantities to play a role as seed particle in dust formation processes [51]. Chapter 6 gives details about the electronic spectra of  $\text{ZrO}_2$ .

Research on pure silicon species,  $\text{Si}_n$  has been driven by technological applications in the semiconductor industry [52] and astrochemical interest as a result of identification of many silicon containing molecules in stellar and interstellar atmospheres [53]. Another motivation has been to understand the difference in the geometries of silicon and carbon clusters, despite both having similar electronic structures. Small silicon clusters have non-linear three-dimensional geome-

---

try [54, 55], in contrast to carbon species which are either in linear or monocyclic ring form [56]. The detection of isovalent SiC<sub>2</sub> [57–59] and C<sub>3</sub> [60, 61] in space has resulted in great spectroscopic interest in Si<sub>3</sub>. The electronic spectra of Si<sub>3</sub> in the visible part of electromagnetic spectrum is presented in Chapter 7. The spectral analysis shows that the molecule exists in two distinct geometries: D<sub>3h</sub> and C<sub>2v</sub>.

Over the last decades, the study of carbon species has attracted interest due to their relevance in fields like combustion, plasma, thin film chemistry and astrophysical environments [56, 62]. Linear chains, monocyclic and polycyclic rings and fullerene structures have been proposed for various carbon species [56]. Theoretical calculations predict the cumulenic chains to be the most stable isomer for odd numbered members of the series, C<sub>*n*</sub> (*n* = 4 – 9), while the linear structure is nearly iso-energetic with the monocyclic ring for the even ones [63]. The cyclic form is favoured for *n* ≥ 10 [64]; however, previous studies show that the linear isomer could be produced under certain experimental conditions [65, 66]. The ground electronic states of several C<sub>*n*</sub> species are known from electronic spin resonance (ESR) studies in solid matrices [67] and high resolution infrared (IR) absorption studies in the gas phase [65, 66, 68–79]. The electronic spectra of molecules *n* > 3 have been studied using matrix isolation spectroscopy for the odd numbered linear chains up to *n* = 21 [80, 81], their even counterparts up to *n* = 14 [82–84] and the even numbered monocyclic rings containing *n* = 6 – 14 carbon atoms [84–86]. Gas phase identification of excited electronic transitions has been possible for linear chains C<sub>4–6,8,9</sub> [87–89], monocyclic rings C<sub>14,18,22</sub> [90, 91] and the fullerenes C<sub>60</sub> and C<sub>70</sub> [92]. In this context, Chapter 8 presents the gas phase electronic spectra of the (2)<sup>3</sup>Σ<sub>*u*</sub><sup>–</sup> – X<sup>3</sup>Σ<sub>*g*</sub><sup>–</sup> transition of C<sub>6</sub> and C<sub>8</sub>, and the <sup>1</sup>Σ<sub>*u*</sub><sup>+</sup> – X<sup>1</sup>Σ<sub>*g*</sub><sup>+</sup> transition of C<sub>7</sub> and C<sub>9</sub>.

Lastly, Chapter 9 concludes and provides an outlook of this work.



# Bibliography

- [1] I. Newton. New theory about light and colors. *Philosophical Transactions of the Royal Society of London*, 6:3075–3087, 1671.
- [2] J. Fraunhofer. Bestimmung des Brechungs - und des Farben-Zerstreuungs - Vermögens verschiedener Glasarten, in Bezug auf die Vervollkommnung achromatischer Fernröhre. *Annalen der Physik*, 56:264–313, 1817.
- [3] G. Kirchhoff. Ueber die Fraunhofer'schen Linien. *Monatsbericht der Königlichen Preussische Akademie der Wissenschaften*, pages 662–665, 1859.
- [4] V. Gupta, F. J. Mazzotti, C. A. Rice, R. Nagarajan, and J. P. Maier. The  $A^2\Sigma^+ - X^2\Pi_i$  electronic transition of AgS. *Journal of Molecular Spectroscopy*, 2013.
- [5] X. Chen, V. Gupta, C. A. Rice, and J. P. Maier. Gas phase electronic spectroscopy of carbon chains,  $C_n$  ( $n = 6 - 9$ ). *Physical Chemistry Chemical Physics*, 2013.
- [6] G. D. Cody. Transition metal sulfides and the origins of metabolism. *Annual Review of Earth and Planetary Sciences*, 32:569–599, 2004.
- [7] T. Weber, H. Prins, and R. A. Van Santen, editors. *Transitional Metal Sulphides: Chemistry and Catalysis*, Proceedings of the NATO Advanced Research Workshop on Challenges for Sulphides in Material Sciences and Catalysis, Varna, Bulgaria, 1997. Kluwer Academic Publishers, Dordrecht, Netherlands.



- [8] E. I. Stiefel and K. Matsumoto, editors. *Transition Metal Sulfur Chemistry*, ACS Symposium Series 653. American Chemical Society, Washington, U. S. A., 1996.
- [9] D. J. Vaughan and J. R. Craig. *Mineral Chemistry of Metal Sulfides*. Cambridge University Press, Cambridge, U. K., 1978.
- [10] J. Jonsson, O. Launila, and B. Lindgren. Titanium sulphide in the spectra of stellar atmospheres. *Monthly Notices of the Royal Astronomical Society*, 258:49–51, 1992.
- [11] D. L. Lambert and R. E. S. Clegg. The Keenan and Wing bands in S stars. *Monthly Notices of the Royal Astronomical Society*, 191:367–389, 1980.
- [12] K. H. Hinkle, D. L. Lambert, and R. F. Wing. Zirconium sulphide in S stars. *Monthly Notices of the Royal Astronomical Society*, 238:1365–1379, 1989.
- [13] J. F. Harrison. Electronic structure of diatomic molecules composed of a first-row transition metal and main-group element (H-F). *Chemical Reviews*, 100:679–716, 2000.
- [14] A. J. Merer. Spectroscopy of the diatomic 3d transition metal oxides. *Annual Review of Physical Chemistry*, 40:407–438, 1989.
- [15] B. Fenot, J. L. Femenias, and R. Stringat. Rotational study and hyperfine effects of the (0,0) band of the  $B^2\Sigma - X^2\Sigma$  system of ScS. *Journal of Molecular Spectroscopy*, 78:40–50, 1979.
- [16] R. M. Clements and R. F. Barrow. Rotational analysis of bands of an infra-red system of gaseous TiS. *Transactions of the Faraday Society*, 65:1163–1167, 1969.
- [17] Q. Ran, W. S. Tam, A. S. C. Cheung, and A. J. Merer. Laser spectroscopy of VS: hyperfine and rotational structure of the  $C^4\Sigma^- - X^4\Sigma^-$  transition. *Journal of Molecular Spectroscopy*, 220:87–106, 2003.

- 
- [18] Q. Shi, Q. Ran, W. S. Tam, J. W. H. Leung, and A. S. C. Cheung. Laser-induced fluorescence spectroscopy of CrS. *Chemical Physics Letters*, 339:154–160, 2001.
- [19] M. Douay, B. Pinchemel, and C. Dufour. Laser-induced fluorescence of MnS: rotational analysis of the  $A^6\Sigma^+ - X^6\Sigma^+$  transition. *Canadian Journal of Physics*, 63:1380–1388, 1985.
- [20] S. Zhang, J. Zhen, Q. Zhang, and Y. Chen. Laser-induced fluorescence spectroscopy of FeS in the visible region. *Journal of Molecular Spectroscopy*, 255:101–105, 2009.
- [21] S. Yu, I. E. Gordon, P. M. Sheridan, and P. F. Bernath. Infrared emission spectroscopy of the  $A^4\Phi_i - X^4\Delta_i$  and  $B^4\Pi_i - X^4\Delta_i$  transitions of CoS. *Journal of Molecular Spectroscopy*, 236:255–259, 2006.
- [22] X. Zheng, T. Wang, J. Guo, C. Chen, and Y. Chen. Laser-induced fluorescence spectroscopy of NiS. *Chemical Physics Letters*, 394:137–140, 2004.
- [23] L. C. O’Brien, M. Dulick, and S. P. Davis. The near-infrared  $Y^2\Sigma^+ - X^2\Pi$  transition of CuS. *Journal of Molecular Spectroscopy*, 195:328–331, 1999.
- [24] R. Stringat, B. Fenot, and J. L. Féménias. Vibrational analysis of the  $A^2\Pi - X^2\Sigma$  and  $B^2\Sigma - X^2\Sigma$  transitions of YS and rotational analysis of the B – X (0, 0) band. *Canadian Journal of Physics*, 57:300–305, 1979.
- [25] A. M. James, R. Fournier, B. Simard, and M. D. Campbell. Electronic spectroscopy of yttrium monosulfide: molecular beam studies and density functional calculations. *Canadian Journal of Chemistry*, 71:1598–1614, 1993.
- [26] P. Kowalczyk, A. M. James, and B. Simard. High-resolution study of the near-infrared  $A^2\Pi_{1/2} - X^2\Sigma^+$  transition of YS. *Journal of Molecular Spectroscopy*, 189:196–201, 1998.

- [27] B. Simard, S. A. Mitchell, and P. A. Hackett. Spectroscopy and photophysics of refractory molecules at low temperature. II. The green systems of ZrS. *Journal of Chemical Physics*, 89:1899–1904, 1988.
- [28] J. Jonsson. The  $b^3\Phi - a^3\Delta$  and  $d^3\Delta - a^3\Delta$  systems of ZrS. *Journal of Molecular Spectroscopy*, 169:18–29, 1995.
- [29] J. Jonsson and B. Lindgren. Infrared spectroscopy: the  $b^3\Pi - a^3\Delta$  system of ZrS. *Journal of Molecular Spectroscopy*, 169:30–37, 1995.
- [30] J. Jonsson, S. Wallin, and B. Lindgren. On the singlet spectrum of ZrS. *Journal of Molecular Spectroscopy*, 192:198–214, 1998.
- [31] B. Simard, C. Masoni, and P. A. Hackett. First laboratory observation of niobium monosulphide in the gas phase. *Journal of Chemical Physics*, 92:7003–7011, 1990.
- [32] O. Launila. Fourier transform spectroscopy of NbS. *Journal of Molecular Spectroscopy*, 229:31–38, 2005.
- [33] R. Li, W. J. Balfour, W. S. Hopkins, and A. G. Adam. A visible spectrum of jet-cooled rhodium monosulfide. *Journal of Molecular Spectroscopy*, 234:211–215, 2005.
- [34] J. Winkler. *Titanium dioxide*. Vincentz Network, Hannover, Germany, 2003.
- [35] W. M. Haynes. *CRC Handbook of chemistry and physics*. CRC Press, Boca Raton, U. S. A., 93rd edition, 2012.
- [36] M. E. Kurtoglu, T. Longenbach, and Y. Gogotsi. Preventing sodium poisoning of photocatalytic TiO<sub>2</sub> films on glass by metal doping. *International Journal of Applied Glass Science*, 2:108–116, 2011.
- [37] T. Miyasaka. Toward printable sensitized mesoscopic solar cells: light-harvesting management with thin TiO<sub>2</sub> films. *Journal of Physical Chemistry Letters*, 2:262–269, 2011.

- 
- [38] A. G. W. Cameron. Abundances of the elements in the solar system. *Space Science Reviews*, 15:121–146, 1973.
- [39] R. E. S. Clegg, D. L. Lambert, and R. A. Bell. Isotopes of titanium in cool stars. *Astrophysical Journal*, 234:188–199, 1979.
- [40] R. Yerle. Tih in M-type stars and sunspots. *Astronomy and Astrophysics*, 73:346–351, 1979.
- [41] W. W. Morgan, P. C. Keenan, and E. Kellman. *An atlas of stellar spectra with an outline of spectral classification*. University of Chicago Press, Chicago, U. S. A., 1943.
- [42] H.-P. Gail and E. Sedlmayr. Mineral formation in stellar winds: I. Condensation sequence of silicate and iron grains in stationary oxygen rich outflows. *Astronomy and Astrophysics*, 347:594–616, 1999.
- [43] T. Kamiński, C. A. Gottlieb, K. M. Menten, N. A. Patel, K. H. Young, S. Brünken, H. S. P. Müller, M. C. McCarthy, and L. Decin J. M. Winters. Pure rotational spectra of TiO and TiO<sub>2</sub> in VY Canis Majoris. *Astronomy and Astrophysics*, In print, 2013.
- [44] G. Wallerstein and G. Gonzalez. The spectrum of VY Canis Majoris in 2000 February. *Publications of the Astronomical Society of the Pacific*, 113:954–956, 2001.
- [45] S. Brünken, H. S. P. Müller, K. M. Menten, M. C. McCarthy, and P. Thaddeus. The rotational spectrum of TiO<sub>2</sub>. *Astrophysical Journal*, 676:1367–1371, 2008.
- [46] R. H. Nielsen and G. Wilfing. Zirconium and zirconium compounds. In *Ullmann's Encyclopedia of Industrial Chemistry*, volume 39, pages 753–778. Wiley-VCH, Weinheim, Germany, 2010.
- [47] G. Reyna-García, M. García-Hipólito, J. Guzmán-Mendoza, M. Aguilar-Frutis, and C. Falcony. Electrical, optical and structural characterization of

- high-k dielectric ZrO<sub>2</sub> thin films deposited by the pyrosol technique. *Journal of Materials Science: Materials in Electronics*, 15:439–446, 2004.
- [48] D. N. Davis. The spectrum of  $\beta$  pegasi. *Astrophysical Journal*, 106:28–75, 1947.
- [49] G. H. Herbig. Identification of a molecular band at  $\lambda$ 3682 in the spectra of late-type stars. *Astrophysical Journal*, 109:109–115, 1949.
- [50] W. W. Morgan and P. C. Keenan. Spectral classification. *Annual Review of Astronomy and Astrophysics*, 11:29–50, 1973.
- [51] A. S. Ferrarotti and H. P. Gail. Mineral formation in stellar winds: III. dust formation in s stars. *Astronomy and Astrophysics*, 382:256–281, 2002.
- [52] S. Yamazaki. Semiconductor device having crystalline silicon clusters. U. S. Patent No. US6252249B1, 2001.
- [53] ed. D. K. Bohme, E. Herbst, N. Kaifu, and S Saito. *Chemistry and Spectroscopy of Interstellar Molecules*, chapter A. E. Glassgold and G. A. Mamon: Circumstellar Chemistry, pages 261–266. University of Tokyo Press, Tokyo, Japan, 1992.
- [54] S. Li, R. J. Van Zee, W. Weltner Jr., and K. Raghavachari. Si<sub>3</sub> - Si<sub>7</sub>. Experimental and theoretical infrared spectra. *Chemical Physics Letters*, 243:275–280, 1995.
- [55] C. Xu, T. R. Taylor, G. R. Burton, and D. M. Neumark. Vibrationally resolved photoelectron spectroscopy of silicon cluster anions Si<sub>n</sub><sup>-</sup> ( $n = 3 - 7$ ). *Journal of Chemical Physics*, 108:1395–1406, 1998.
- [56] A. Van Orden and R. J. Saykally. Small carbon clusters: spectroscopy, structure, and energetics. *Chemical Reviews*, 98:2313–2357, 1998.
- [57] P. W. Merrill. Note on the spectrum of UV Aurigæ. *Publications of the Astronomical Society of the Pacific*, 38:175–176, 1926.

- 
- [58] R. F. Sanford. Two bands in spectra of class N. *Publications of the Astronomical Society of the Pacific*, 38:177–179, 1926.
- [59] B. Kleman. Laboratory excitation of the blue-green bands observed in the spectra of N-type stars. *Astrophysical Journal*, 123:162–165, 1956.
- [60] K. W. Hinkle, J. J. Keady, and P. F. Bernath. Detection of  $C_3$  in the circumstellar shell of IRC+10216. *Science*, 241:1319–1322, 1988.
- [61] J. P. Maier, N. M. Lakin, G. A. H. Walker, and D. A. Bohlender. Detection of  $C_3$  in diffuse interstellar clouds. *Astrophysical Journal*, 553:267–273, 2001.
- [62] W. Weltner Jr. and R. J. Van Zee. Carbon molecules, ions, and clusters. *Chemical Reviews*, 89:1713–1747, 1989.
- [63] J. M. L. Martin and P. R. Taylor. Structure and vibrations of small carbon clusters from coupled-cluster calculations. *Journal of Physical Chemistry*, 100:6047–6056, 1996.
- [64] J. Hutter, H. P. Lüthi, and F. Diederich. Structures and vibrational frequencies of the carbon molecules  $C_2 - C_{18}$  calculated by density functional theory. *Journal of the American Chemical Society*, 116:750–756, 1994.
- [65] T. F. Giesen, U. Berndt, K. M. T. Yamada, G. Fuchs, R. Schieder, G. Winnewisser, R. A. Provencal, F. N. Keutsch, A. Van Orden, and R. J. Saykally. Detection of the linear carbon cluster  $C_{10}$ : rotationally resolved diode-laser spectroscopy. *European Journal of Chemical Physics and Physical Chemistry*, 2:242–247, 2001.
- [66] T. F. Giesen, A. Van Orden, H. J. Hwang, R. S. Fellers, R. A. Provencal, and R. J. Saykally. Infrared laser spectroscopy of the linear  $C_{13}$  carbon cluster. *Science*, 265:756–759, 1994.
- [67] R. J. Van Zee, R. F. Ferrante, K. J. Zeringue, and W. Weltner Jr. Electron spin resonance of the  $C_6$ ,  $C_8$ , and  $C_{10}$  molecules. *Journal of Chemical Physics*, 88:3465–3474, 1988.

- [68] K. Matsumura, H. Kanamori, K. Kawaguchi, and E. Hirota. Infrared diode laser kinetic spectroscopy of the  $\nu_3$  band of  $C_3$ . *Journal of Chemical Physics*, 89:3491–3494, 1988.
- [69] C. A. Schmuttenmaer, R. C. Cohen, N. Pugliano, J. R. Heath, A. L. Cooksy, K. L. Busarow, and R. J. Saykally. Tunable far-IR laser spectroscopy of jet-cooled carbon clusters: the  $\nu_2$  bending vibration of  $C_3$ . *Science*, 249:897–900, 1990.
- [70] J. R. Heath and R. J. Saykally. The structure of the  $C_4$  cluster radical. *Journal of Chemical Physics*, 94:3271–3273, 1991.
- [71] N. Moazzen-Ahmadi, J. J. Thong, and A. R. McKellar. Infrared diode laser spectroscopy of the  $\nu_3$  fundamental and  $\nu_2 + \nu_5 - \nu_5$  sequence bands of the  $C_4$  radical in a hollow cathode discharge. *Journal of Chemical Physics*, 100:4033–4038, 1994.
- [72] N. Moazzen-Ahmadi, A. R. W. McKellar, and T. Amano. Laboratory observation of the rotation-vibration spectrum of gas-phase  $C_5$ . *Chemical Physics Letters*, 157:1–4, 1989.
- [73] J. R. Heath, A. L. Cooksy, M. H. W. Gruebele, C. A. Schmuttenmaer, and R. J. Saykally. Diode-laser absorption spectroscopy of supersonic carbon cluster beams: the  $\nu_3$  spectrum of  $C_5$ . *Science*, 244:564–566, 1989.
- [74] H. J. Hwang, A. Van Orden, K. Tanaka, E. W. Kuo, T. R. Heath, and R. J. Saykally. Infrared laser spectroscopy of jet-cooled carbon clusters: structure of triplet  $C_6$ . *Molecular Physics*, 79:769–776, 1993.
- [75] J. R. Heath, R. A. Sheeks, A. L. Cooksy, and R. J. Saykally. The  $C_7$  cluster: structure and infrared frequencies. *Science*, 249:895–897, 1990.
- [76] J. R. Heath, A. Van Orden, E. Kuo, and R. J. Saykally. The  $\nu_5$  band of  $C_7$ . *Chemical Physics Letters*, 182:17–20, 1991.

- 
- [77] P. Neubauer-Guenther, T. F. Giesen, U. Berndt, G. Fuchs, and G. Winnewisser. The Cologne Carbon Cluster Experiment: ro-vibrational spectroscopy on  $C_8$  and other small carbon clusters. *Spectrochimica Acta Part A: Molecular and Biomolecular Spectroscopy*, 59:431–441, 2003.
- [78] J. R. Heath and R. J. Saykally. The  $C_9$  cluster: structure and infrared frequencies. *Journal of Chemical Physics*, 93:8392–8394, 1990.
- [79] A. Van Orden, H. J. Hwang, E. W. Kuo, and R. J. Saykally. Infrared laser spectroscopy of jet-cooled carbon clusters: the bending dynamics of linear  $C_9$ . *Journal of Chemical Physics*, 98:6678–6683, 1993.
- [80] D. Forney, P. Freivogel, M. Grutter, and J. P. Maier. Electronic absorption spectra of linear carbon chains in neon matrices. IV.  $C_{2n+1}$   $n = 2-7$ . *Journal of Chemical Physics*, 104:4954–4960, 1996.
- [81] M. Wyss, M. Grutter, and J. P. Maier. Electronic spectra of long odd-number carbon chains  $C_{17}-C_{21}$  and  $C_{13}^- - C_{21}^-$ . *Chemical Physics Letters*, 304:35–38, 1999.
- [82] P. Freivogel, M. Grutter, D. Forney, and J. P. Maier. The  ${}^3\Sigma_u^- \leftarrow X^3\Sigma_g^-$  electronic absorption spectrum of linear  $C_4$  in a neon matrix. *Chemical Physics Letters*, 249:191–194, 1996.
- [83] P. Freivogel, J. Fulara, M. Jakobi, D. Forney, and J. P. Maier. Electronic absorption spectra of linear carbon chains in neon matrices. II.  $C_{2n}^-$ ,  $C_{2n}$ , and  $C_{2n}H$ . *Journal of Chemical Physics*, 103:54–59, 1995.
- [84] M. Grutter, M. Wyss, E. Riaplov, J. P. Maier, S. D. Peyerimhoff, and M. Hanrath. Electronic absorption spectra of linear  $C_6$ ,  $C_8$  and cyclic  $C_{10}$ ,  $C_{12}$  in neon matrices. *Journal of Chemical Physics*, 111:7397–7401, 1999.
- [85] S. L. Wang, C. M. L. Rittby, and W. R. M. Graham. Detection of cyclic carbon clusters. I. Isotopic study of the  $\nu_4(e')$  mode of cyclic  $C_6$  in solid Ar. *Journal of Chemical Physics*, 107:6032–6037, 1997.



- [86] J. D. Presilla-Marquez, J. Harper, J. A. Sheehy, P. G. Carric, and C. W. Larson. Vibrational spectra of cyclic  $C_8$  in solid argon. *Chemical Physics Letters*, 300:719–726, 1999.
- [87] H. Linnartz, O. Vaizert, T. Motylewski, and J. P. Maier. The  ${}^3\Sigma_u^- \leftarrow X^3\Sigma_g^-$  electronic spectrum of linear  $C_4$  in the gas phase. *Journal of Chemical Physics*, 112:9777–9779, 2000.
- [88] T. Motylewski, O. Vaizert, T. F. Giesen, H. Linnartz, and J. P. Maier. The  ${}^1\Pi_u \leftarrow X^1\Sigma_g^+$  electronic spectrum of  $C_5$  in the gas phase. *Journal of Chemical Physics*, 111:6161–6163, 1999.
- [89] A. E. Boguslavskiy and J. P. Maier. Gas phase electronic spectra of the carbon chains  $C_5$ ,  $C_6$ ,  $C_8$ , and  $C_9$ . *Journal of Chemical Physics*, 125:94308–1–7, 2006.
- [90] A. E. Boguslavskiy and J. P. Maier. Gas-phase electronic spectrum of the  $C_{14}$  ring. *Physical Chemistry Chemical Physics*, 9:127–130, 2007.
- [91] A. E. Boguslavskiy, H. Ding, and J. P. Maier. Gas-phase electronic spectra of  $C_{18}$  and  $C_{22}$  rings. *Journal of Chemical Physics*, 123:34305–1–7, 2005.
- [92] R. E. Haufler, Y. Chai, L. P. F. Chibante, M. R. Fraelich, R. B. Weisman, R. F. Curl, and R. E. Smalley. Cold molecular beam electronic spectrum of  $C_{60}$  and  $C_{70}$ . *Journal of Chemical Physics*, 95:2197–2199, 1991.

# 2 Background

## 2.1 Electronic Spectroscopy

The Born-Oppenheimer approximation [1], i.e. the separation of electronic and nuclear motion in a molecule, forms the basis of molecular spectroscopy. The nonrelativistic Hamiltonian operator is given by

$$\hat{H} = \frac{-\hbar^2}{2} \sum_{\alpha} \frac{\nabla_{\alpha}^2}{M_{\alpha}} - \frac{\hbar^2}{2m_e} \sum_i \nabla_i^2 + \sum_{\alpha} \sum_{\beta > \alpha} \frac{Z_{\alpha} Z_{\beta} e^2}{4\pi\epsilon_0 r_{\alpha\beta}} - \sum_{\alpha} \sum_i \frac{Z_{\alpha} e^2}{4\pi\epsilon_0 r_{i\alpha}} + \sum_i \sum_{j > i} \frac{e^2}{4\pi\epsilon_0 r_{ij}},$$
$$\hat{H} = \hat{T}_N + \hat{T}_e + \hat{V}_{NN} + \hat{V}_{eN} + \hat{V}_{ee},$$

where  $\alpha, \beta$  denote the nuclei in a molecule and  $i, j$  the electrons.  $\hat{T}_N, \hat{T}_e, \hat{V}_{NN}, \hat{V}_{eN}, \hat{V}_{ee}$  indicate the nuclear and kinetic energy, nuclear-nuclear repulsion, the electron-nuclear attraction and the electron-electron repulsion, respectively. There is no direct solution for the Schrödinger equation  $\hat{H}\psi = E\psi$ , with this Hamiltonian operator. However, it can be solved by applying the Born-Oppenheimer approximation, and separating electronic and nuclear motion. The electronic structure is solved by fixing the position of nuclei and solving the pure electronic equation

$$\hat{H}_{el}\psi_{el} = E_{el}\psi_{el},$$

in which

$$\hat{H}_{el} = \hat{T}_e + \hat{V}_{eN} + \hat{V}_{ee}.$$

Figure 2.1 shows schematic of energy levels for a diatomic molecule.

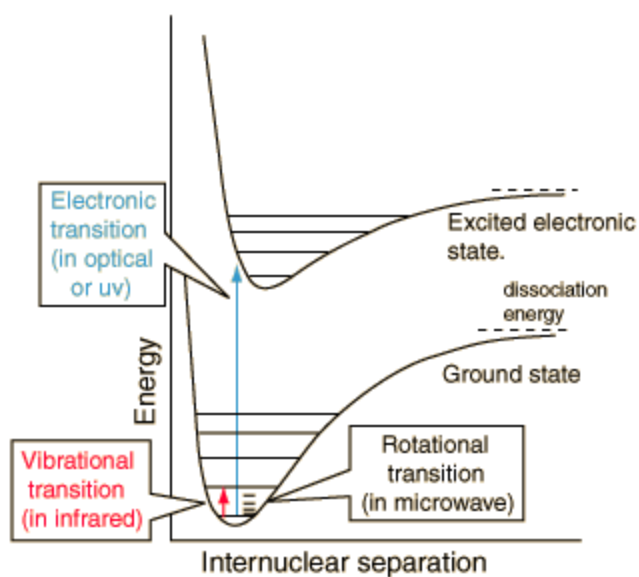


Figure 2.1: Schematic of energy levels for a diatomic molecule.

### 2.1.1 Molecular Orbitals

The electronic Schrödinger equation can be solved approximately by constructing a set of molecular orbitals (MOs) in which each MO is a linear combination of atomic orbitals (LCAOs) [2]

$$\phi_{MO} = \sum c_i \phi_i.$$

The total wavefunction is a Slater determinant of MOs [3],

$$| \psi_{el} = \phi_{MO}(1)\bar{\phi}_{MO}(2)\dots |.$$

Information about the electronic structure can therefore be derived from consideration of the shapes of the MOs constructed as LCAOs.

The selection rules for electronic transitions are derived through the use of the transition moment integral

$$\int \psi_{el,f}^* \hat{\mu} \psi_{el,i} d\tau.$$

Here  $\psi_{el,f}$  and  $\psi_{el,i}$  are eigenfunctions in the upper and lower states, and  $\hat{\mu}$  is the dipole moment of the system of nuclei and electrons for a definite electronic configuration. If the value of this integral is zero the transition is forbidden. The integral itself need not be calculated to determine a selection rule. It is sufficient to determine the symmetry of transition moment function,  $\psi_{el,f}^* \hat{\mu} \psi_{el,i}$ . If the integral contains the totally symmetric irreducible representation of the point group, the transition is allowed; otherwise, it is forbidden.

### 2.1.2 Vibrational Structure

Within the Born-Oppenheimer approximation, the separation of vibrational and electronic motion leads to the concept of associating electronic states with potential energy surfaces [2]. For a diatomic molecule, the potential energy function  $V(r)$  is a function of a single variable, the internuclear distance,  $r$ . For a polyatomic molecule  $V(Q_i)$  is a function of  $3N - 6$  ( $3N - 5$  in case of linear molecules) internal coordinates, which can be expressed in terms of normal modes. This gives rise to a multidimensional potential energy surface for each polyatomic electronic state, compared to a simple one dimensional case for a diatomic molecule.

The solution of the Schrödinger equation for nuclear motion on each potential energy surface of a polyatomic molecule provides the corresponding vibrational frequencies and anharmonicities for each electronic state, given by [4]

$$G(v_i) = \sum_r \omega_r \left(v_r + \frac{d_r}{2}\right) + \sum_{r,s>r} x_{rs} \left(v_r + \frac{d_r}{2}\right) \left(v_s + \frac{d_s}{2}\right) + \sum_{t,t'>t} g_{tt'} l_t l_{t'}.$$

In this equation, the  $\omega_r$  are the harmonic vibrational frequencies, each with a corresponding degeneracy term  $d_r$ , the  $x_{rs}$  and  $g_{tt'}$  are the anharmonic corrections, where  $t$  refers to degenerate modes with vibrational angular momentum  $l_t$ . For a diatomic molecule, this equation reduces to

$$G(v) = \omega_e \left(v + \frac{1}{2}\right) - \omega_e x_e \left(v + \frac{1}{2}\right)^2.$$

A vibronic transition frequency is given by the difference between two vibronic term values, i.e.,

$$\tilde{\nu} = \Delta T_e + G'(v'_1, v'_2, \dots) - G''(v''_1, v''_2, \dots),$$

in which  $\Delta T_e$  is the minimum potential energy difference between the two states.

The vibrational selection rules for an allowed electronic transition are determined from the Franck-Condon principle [5, 6]. The intensity of the vibronic transition is proportional to the square of the transition moment integral,

$$M_{e'v'e''v''} = \int \psi_{e'v'}^* \hat{\mu} \psi_{e''v''} d\tau_{ev}.$$

The Born-Oppenheimer approximation separates electronic and nuclear motion,  $\psi_{e'v'e''v''} = \psi_{e'e''} \psi_{v'v''}$ . So, transition moment integral becomes

$$M_{e'v'e''v''} = \int \psi_{e'}^* \hat{\mu} \psi_{e''} d\tau_{el} \int \psi_{v'}^* \psi_{v''} d\tau_v = M_{e'e''} \int \psi_{v'_1}^* \psi_{v''_1} dQ_1 \int \psi_{v'_2}^* \psi_{v''_2} dQ_2 \dots$$

Within the realm of the Born-Oppenheimer approximation and normal mode approximations [2], the transition moment integral is comprised of an electronic transition dipole moment

$$M_{e'e''} = R_e = \langle \psi_{e'} | \hat{\mu} | \psi_{e''} \rangle$$

and a product of  $3N - 6$  ( $3N - 5$ ) vibrational overlap integrals, and can be written as

$$M_{e'v'e''v''} = \langle \psi_{e'} | \hat{\mu} | \psi_{e''} \rangle \langle v'_1 | v''_1 \rangle \langle v'_2 | v''_2 \rangle \dots$$

For a totally symmetric vibration, the selection rule for  $v$  is

$$\Delta v_i = 0, \pm 1, \pm 2, \dots,$$

and intensity is determined by the Franck-Condon factor

$$q_{v'_i-v''_i} = \left| \int \psi_{v'_i}^* \psi_{v''_i} dQ_i \right|^2.$$

For non-totally symmetric vibrations, the Franck-Condon factor vanishes for  $v_i$  values such that

$$\Delta v_i = \pm 1, \pm 3, \pm 5, \dots$$

because the product  $\Gamma^{\psi_{v'}} \otimes \Gamma^{\psi_{v''}}$  does not contain the totally symmetric irreducible representation. For an allowed transition, the nonsymmetric vibrational modes obey the selection rule

$$\Delta v_i = \pm 2, \pm 4, \pm 6, \dots$$

within the harmonic approximation.

### 2.1.2.1 Herzberg-Teller Effect

Although forbidden, often nonsymmetric vibrational transitions occur in an electronic transition with the selection rule  $\Delta v_i = \pm 1, \pm 3, \pm 5, \dots$ . These forbidden electronic transitions become allowed by vibronic coupling, as first explained by Herzberg and Teller [2, 4, 7]. This requires that the transition moment integral

$$\int \psi_{vibronic'}^* \hat{\mu} \psi_{vibronic''} d\tau$$

be considered for the total vibronic symmetry ( $\Gamma^{vibronic} = \Gamma^{el} \otimes \Gamma^{vib}$ ).

The intensity of the vibronic transition depends on the degree of mixing of the vibrational and electronic wavefunctions and can be derived using perturbation theory. The Schrödinger equation of the fixed equilibrium configuration for a set of zeroth-order electronic and harmonic wavefunctions without the effects of vibronic coupling is given by

$$\hat{H}_e^0 \psi_e^0 = E_e \psi_e^0.$$

Vibronic coupling is derived by expanding the electronic Hamiltonian operator in a Taylor series

$$\hat{H}_e = \hat{H}_e^0 + \sum_i \left( \frac{\partial \hat{H}_e}{\partial Q_i} \right)_{Q_i=0} Q_i + \dots$$

Truncating the expansion to the first term gives the perturbation operator as

$$\hat{H}' = \sum_i \left( \frac{\partial \hat{H}_e}{\partial Q_i} \right)_{Q_i=0} Q_i .$$

The degree of mixing is determined as the ratio of the magnitude of the vibronic coupling matrix element  $\langle \psi_k^0 | \hat{H}' | \psi_f^0 \rangle$  and the separation  $(E_f^0 - E_k^0)$  between the interacting electronic states  $\psi_f$  and  $\psi_k$ .

### 2.1.2.2 Jahn-Teller Effect

The Jahn-Teller effect [2,4,7,8] also violates the selection rule  $\Delta v_i = \pm 2, \pm 4, \pm 6, \dots$ , for non-symmetric vibrations in an electronic transition. According to Jahn-Teller theorem [8], any non-linear molecular system in a degenerate electronic state will be unstable and will undergo distortion to form a system of lower symmetry and lower energy thereby removing the degeneracy. This is a consequence of a breakdown in the Born-Oppenheimer approximation. Using the same approach as was used for Herzberg-Teller effect, a perturbation operator  $\hat{H}'$  can be considered responsible for the mixing of vibrational and electronic wavefunctions. If  $\psi_a$  and  $\psi_b$  are linearly independent orbitally degenerate wavefunctions, then  $\hat{H}'$  will lift their degeneracy if there is a non zero matrix element between them, i.e.,

$$\int \psi_a^* \hat{H}' \psi_b d\tau_e = \sum_i \int \psi_a^* \left( \frac{\partial \hat{H}_e}{\partial Q_i} \right)_{Q_i=0} Q_i \psi_b d\tau_e \neq 0.$$

This will be nonzero only if  $\Gamma^{Q_i} \otimes (\Gamma^{\psi_a} \otimes \Gamma^{\psi_b})_{sym}$  contains the totally symmetric irreducible representation. In the case of all degenerate states, a non totally symmetric vibrational distortion ( $Q_i$ ) is present [8], lowering the symmetry of the molecule. This is shown schematically in Figure 2.2.

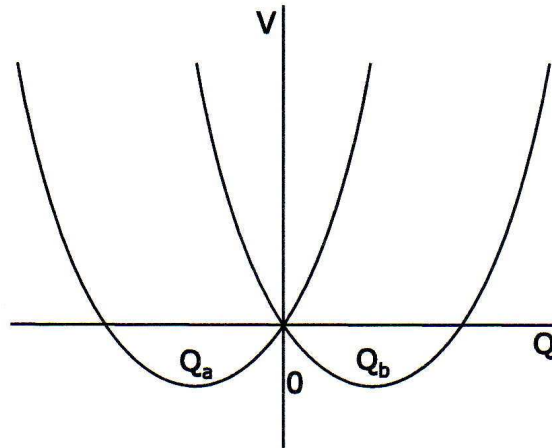


Figure 2.2: Schematic of Jahn-Teller distortion along a doubly degenerate vibration coordinate.

For molecular systems with half-closed-shell electronic configurations, which produce totally symmetric charge distribution and are not subject to the Jahn-Teller effect, distortions may occur due to the strong pseudo Jahn-Teller mixing of two excited states, which is a second order effect.

### 2.1.2.3 Renner-Teller Effect

Another breakdown in the Born-Oppenheimer approximation is the Renner-Teller effect [2,4,7], which occurs in linear molecules as a result of an interaction between vibrational and electronic angular momenta for states in which  $\Lambda \neq 0$ . The levels associated with bending modes are shifted in energy, due to this interaction. The Renner-Teller effect occurs because the double orbital degeneracy is lifted when a linear molecule bends during vibrational motion (Figure 2.3). As a linear molecule bends, the two potential curves  $V^+$  and  $V^-$  becomes distinct.

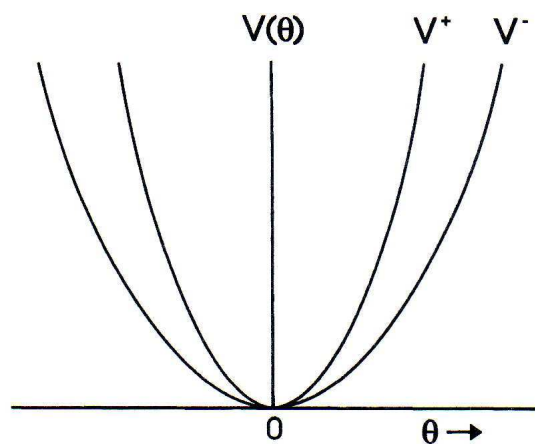


Figure 2.3: Schematic of Renner-Teller distortion along a doubly degenerate vibration coordinate.



### 2.1.3 Rotational Structure

For electronic or vibronic transitions there is a set of accompanying  $J$  states between manifolds of rotational levels associated with upper and lower electronic or vibronic states. A particular rovibronic transition occurs at a line position with

$$\tilde{\nu} = \Delta T_e + G'(v') + F(J') - G''(v'') - F(J''),$$

where  $G(v)$  and  $F(J)$  are vibrational and rotational energy level expressions, and  $T_e$  is the equilibrium transition energy between the states. The rotational structure depends on the vibronic symmetry of the ground and excited states, and the relative change in geometry between them [4, 9].

### 2.1.4 Fine Structure

The nonrelativistic Schrödinger equation is not complete [10] and additional relativistic terms need to be added to the Hamiltonian. The largest additional term is needed to account for the presence of electron spin,  $\hat{H}_{es}$ , and is called fine structure. This term includes spin-orbit, spin-rotation and spin-spin coupling, namely,

$$\hat{H}_{es} = \hat{H}_{so} + \hat{H}_{sr} + \hat{H}_{ss}.$$

The effects of  $\hat{H}_{es}$  are present in non-singlet multiplicity cases.

## 2.2 Multiphoton Spectroscopy

In a multiphoton process, a molecule can undergo a transition  $E_i \rightarrow E_f$  by absorbing two or more photons. The first theoretical treatment of such a process was reported in 1931 by Göppert-Mayer [11], but the experimental realization [12] had to wait for the development of intense light sources provided by lasers.

The transition probability for a multiphoton process can be formulated using time dependent perturbation theory. Consider the simple case of a two-photon process, where a molecule undergoes a transition from the initial level  $\langle i |$  to the final level  $\langle f |$  via an intermediate level  $\langle k |$ . The transition probability for the

two-photon process,  $W^{(2)}$ , taking into account only the lowest order term of the radiation-molecule interaction, is given

$$W^{(2)} \propto I^2 \left| \sum_k \frac{\langle f | \hat{\mu} | k \rangle \langle k | \hat{\mu} | i \rangle}{\Delta E_{ki} - \hbar\omega_r} \right|^2,$$

where  $I$  is the intensity of laser,  $\Delta E_{ki}$  is the energy difference between intermediate and initial states,  $\hat{\mu}$  is the dipole moment and  $\omega_r$  is the laser frequency. This equation shows that the two photon transition probability is proportional to the square of laser intensity. Moreover,  $n$ -photon transition probability is proportional to  $I^n$ , which is the formal intensity law for multiphoton transition.

The  $I^n$  dependence does not hold true under all conditions. It is valid for cases of low-intensity laser experiments, long lived intermediate states for short pulse times, and before the steady state condition is satisfied. The use of high-intensity lasers may result in saturation of population between the intermediate and ground states and make it easy to reach a steady-state condition. A pure quadratic intensity dependence that obeys the formal intensity laws is observed for laser intensities below  $10^7 \text{ W cm}^{-2}$  [13]. Above this threshold value, the dependence changes from quadratic to roughly linear.

### 2.2.1 Resonant Absorption

For a two photon process, when the laser frequency is tuned to the energy difference between the intermediate and lower state, there is a drastic increase in the two-photon signal. This process is called a resonant two-photon transition. This process can be explained mathematically; when

$$\omega_r = \frac{\Delta E_{ki}}{\hbar}$$

the denominator of the above equation becomes zero and the transition probability goes to infinity. However, the energy levels of the intermediate state are not infinitely narrow but have a width, hence the transition probability is never infinity in the real case. Figure 2.4 presents the level schemes for resonant and non-resonant two photon transitions.

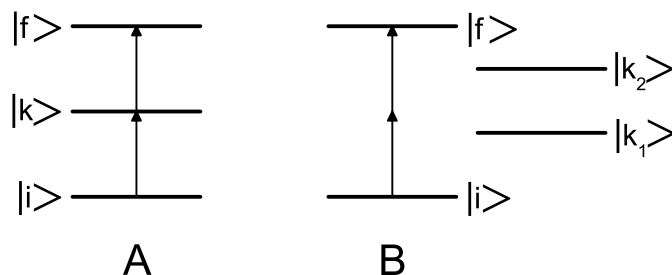


Figure 2.4: Level schemes for (A) resonant and (B) non-resonant two photon transitions.

The vibronic structure appearing in the resonant multiphoton transition is generally different from that in a non-resonant one: in the former the vibronic structure reflects the potential differences between the initial, resonant and final states, while in the latter the vibronic structure is mainly determined by the overlap integral between the initial and final states, due to large energy mismatch to the intermediate state.

### 2.2.2 Resonance Enhanced Multiphoton Ionization

In a multiphoton process, the photons can either be absorbed simultaneously or sequentially. Simultaneous absorption of more than one photon is rarely observed in nature. However, a sufficiently intense laser can cause molecules to simultaneously absorb enough photons to ionize. Under typical conditions, the ionization rates decrease rapidly with the number of photons required.

The ionization rate for any molecule can be greatly enhanced when ionized sequentially and the absorption steps (resonances) are provided by stable states that can accumulate a population. This process is called resonance enhanced multiphoton ionization (REMPI). Spectra can be obtained by monitoring the photoelectrons or laser generated cations. These spectra reflect the properties of the initial and resonant intermediate excited states. The final absorption step which

produces the ion does not influence the spectrum strongly, due to ejection of an electron being a much faster process. Several schemes for can be adopted based on the number and colour of photons used.

### 2.2.2.1 One-Color Two-Photon Scheme

In one-color two-photon [1+1] scheme, the laser is scanned through the electronic transitions of the molecule of interest, so that resonant photons excite the molecule to the intermediate state. The molecule then absorbs a second photon for ionization. In this scheme the energy of a photon must be  $\geq 1/2$  of the ionization potential (IP). This technique was used to record the UV spectra of carbon chains,  $C_{6,7,8,9}$  during the course of this work.

### 2.2.2.2 Two-Color Two-Photon Scheme

In a two-color two-photon [1+1'] scheme, the first laser is scanned through the electronic transitions and a second colour of a fixed frequency is used to ionize the molecules from the resonant excited intermediate state. The sum of the two photon energies from both lasers should be more than the IP of species of interest. The energy of the ionization photon varies depending on the transition frequency and IP of the molecule under investigation. During the course of this study, 3.5 eV, 4.7 eV, 6.4 eV, 7.9 eV and 10.5 eV photons were used for ionization. This scheme was employed to record UV/Vis spectra of several molecules presented herein.

### 2.2.2.3 Multiphoton Schemes

Higher order process like [2+1] or [2+1'] may be used in cases where one photon is not enough to bring the molecule to the excited state. However, such schemes are rarely employed due to drawbacks like smaller absorption cross-section, different selection rules for multi-photon excitation and requirement of more powerful lasers.

## 2.3 Supersonic Free Jet Expansion

When a gas is expanded adiabatically through a small nozzle from a high pressure region to a low pressure region, the conversion of internal energy of the gas into kinetic energy leads to decrease in translational, vibrational and rotational temperatures [14]. This decrease in temperature reduces the Doppler broadening significantly. The partial cooling of rotational and vibrational degrees of freedom simplifies the otherwise congested molecular spectrum, providing an easier analysis.

The gas emerges through a small nozzle of diameter  $D$  from a high pressure source ( $P_0, T_0$ ) to a low pressure ( $P$ ) region at a sonic speed (Mach number,  $M = 1$ ). Beyond the nozzle exit, the flow becomes supersonic ( $M > 1$ ), and the temperature and density of a gas decrease with increasing distance from the nozzle. At some point shock waves appear, reducing the  $M$  to subsonic values. This causes the pressure to increase in the region, until the Mach disk appears normal to the flow at a distance  $x_m$  from the nozzle given by

$$x_m = 0.67D\sqrt{\frac{P_0}{P}}.$$

## 2.4 Time-of-Flight Mass Spectrometry

Time-of-flight (TOF) mass spectrometry is a method of mass spectrometry in which an ion's mass-to-charge ( $m/Z$ ) ratio is determined via a time measurement. A TOF mass spectrometer uses the differences in transit time through a drift region to separate ions of different masses. It operates in a pulsed mode so ions must be produced or extracted in pulses.

The potential energy  $PE$ , of a charged particle in an electric field is related to the charge of the particle and to the strength of the electric field:

$$PE = ZV,$$

where  $Z$  is the charge of the particle, and  $V$  is the electric potential difference. When the ion is accelerated into TOF tube by the voltage  $V$ , its potential energy is converted to kinetic energy. The kinetic energy  $KE$  of any mass  $m$  is:

$$KE = \frac{1}{2}mv^2.$$

Since, the potential energy is converted to kinetic energy,

$$qV = \frac{1}{2}mv^2.$$

The velocity of the charged particle after acceleration will not change since it moves in a field-free TOF tube. The transit time  $t$  through the drift tube of length  $D$  is

$$t = \frac{D}{v} = \frac{D}{\sqrt{2V}} \sqrt{\frac{m}{Z}}.$$

Thus the mass-to-charge ratios can be determined from this equation if the exact drift length and acceleration potential are known. However, the direct relation is rarely used. In most cases, calibration of the TOF spectrometer is performed through empirical determination of the TOF of a pair of known masses. This allows constants  $a$  and  $b$  in the equation

$$t_i = a\sqrt{\left(\frac{m}{Z}\right)_i} + b$$

to be determined and, afterwards, any experimental TOFs,  $t$ , to be converted to a  $m/Z$  value to identify the unknown ions.

The resolution of the mass spectrometer is defined broadly as the ability to distinguish two ions of adjacent masses. If all ions were formed in a plane parallel to the electrodes and with zero initial velocity the flight time would be same for all ions which have the same  $m/Z$ , and the resolution would be limited by the detecting equipment. In practice, however, the resolving power of a TOF spectrometer depends on its ability to reduce the time spread caused by the initial space and kinetic energy distribution. Ions of the same mass formed at the same time with the same initial kinetic energy, but at different locations in the extraction field will receive different kinetic energies from the electric field. This initial spacial

distribution will therefore result in different arrival times for otherwise identical ions. A solution for this is to employ a dual-stage ionization region of three electrodes [15].

# Bibliography

- [1] M. Born and R. Oppenheimer. Zur Quantentheorie der Molekeln. *Annalen der Physik*, 389:457–484, 1927.
- [2] P. F. Bernath. *Spectra of atoms and molecules*. Oxford University Press, New York, U. S. A., 2nd edition, 2005.
- [3] J. C. Slater. The theory of complex spectra. *Physical Review*, 34:1293–1322, 1929.
- [4] G. Herzberg. *Electronic Spectra and Eletronic Structure of Polyatomic Molecules*. Van Nostrand Reinhold, New York, U. S. A., 1966.
- [5] J. Franck. Elementary processes of photochemical reactions. *Transactions of the Faraday Society*, 21:536–542, 1926.
- [6] E. Condon. A theory of intensity distribution in band systems. *Physical Review*, 28:1182–1201, 1926.
- [7] G. Fischer. *Vibronic Coupling*. Academic Press, London, U. K., 1984.
- [8] H. Jahn and E. Teller. Stability of polyatomic molecules in degenerate electronic states. I. Orbital degeneracy. *Proceedings of the Royal Society of London. Series A, Mathematical and Physical Sciences*, 161:220–235, 1937.
- [9] G. Herzberg. *Spectra of Diatomic Molecules*. Van Nostrand Reinhold, New York, U. S. A., 1950.
- [10] P. R. Bunker and P. Jensen. *Molecular Symmetry and Spectroscopy*. NRC Research Press, Ottawa, Canada, 2nd edition, 1998.



- [11] M. Göppert-Mayer. Über elementarakte mit zwei quantensprüngen. *Annalen der Physik*, 401:273–294, 1931.
- [12] W. Kaiser and C. G. Garret. Two-photon excitation in  $\text{CaF}_2: \text{E}_u^{2+}$ . *Physical Review Letters*, 7:229–231, 1961.
- [13] U. Boesl, H. J. Neuseer, and E. W. Schlag. Multi-photon ionization in the mass spectrometry of polyatomic molecules: Cross sections. *Chemical Physics*, 55:193–204, 1981.
- [14] D. H. Levy. Laser spectroscopy of cold gas-phase molecules. *Annual Review of Physical Chemistry*, 31:197–225, 1980.
- [15] W. C. Wiley and I. H. McLaren. Time-of-flight mass spectrometer with improved resolution. *Review of Scientific Instruments*, 26:1150–1157, 1955.

### 3 Experimental

The experimental setup used to study the electronic spectra of transient molecules is depicted in Figure 3.1. It consists of a molecular source, the ionization region, time-of-flight mass spectrometer (TOF-MS) and the detection system.

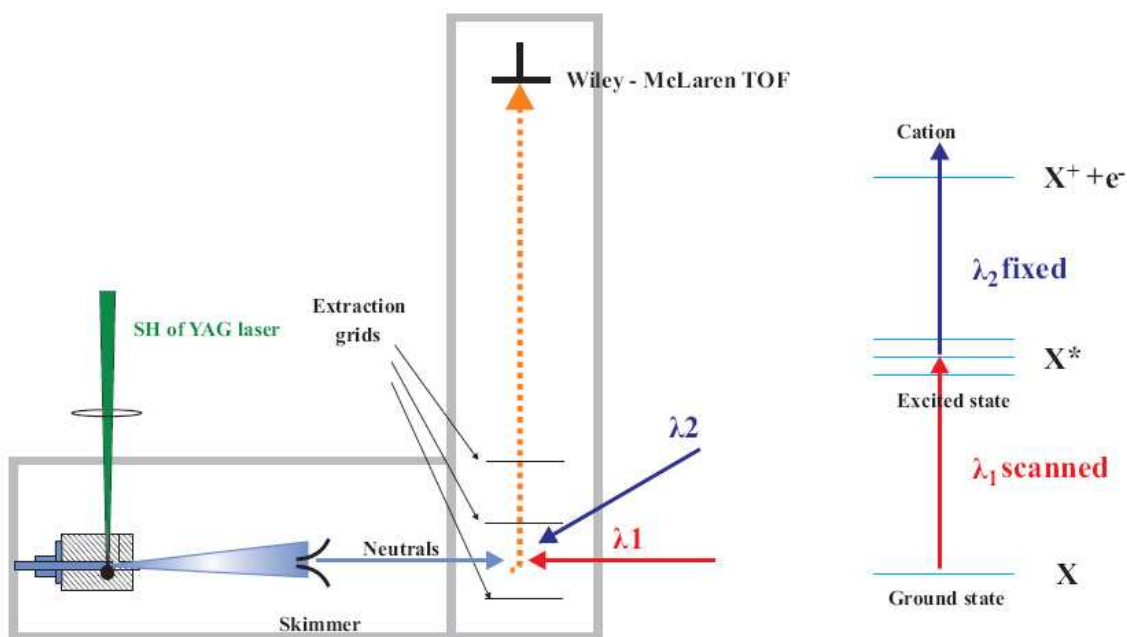


Figure 3.1: The experimental setup.

Transient molecules are produced either in an ablation or a discharge source under supersonic expansion conditions and a collimated molecular beam is produced by a skimmer  $\sim 50$  mm downstream. Ions are removed before the molecular beam enters the ionization region of a TOF-MS, by applying 300 V electric potential on a skimmer. Neutral molecules are then sequentially ionized using resonance

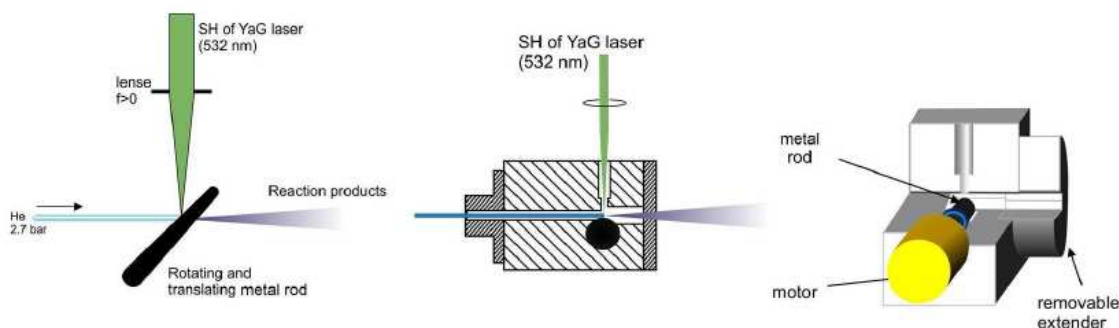


Figure 3.2: Ablation source.

enhanced multiphoton ionization (REMPI) technique; the resulting ions are extracted in a two stage acceleration set-up and detected by a micro-channel plate (MCP) ion detector. This technique allows the recording of absorption spectra of many species with different  $m/Z$  at the same time. Its greatest advantage lies in its mass selectivity, which allows one to make an unambiguous assignment of absorption features to a particular species; biggest disadvantage being its applicability only in the case of neutral molecules.

## 3.1 Molecular Sources

Two molecular sources were used for the experiments discussed in this work: discharge source and laser ablation source.

### 3.1.1 Ablation Source

The ablation source (Figure 3.2) relies on the conventional laser vaporization of a solid elemental/alloy rod [1–4]. The rod is rotated and translated so that a fresh surface is continuously exposed to the laser (50 mJ/1064 nm or 25 mJ/532 nm, 5 ns pulse of Nd:YAG, focused into 0.3 mm spot) which is fired to coincide with a pure helium or a gas mixture flowed over the target area. Vaporized material is passed through a 5 mm long and 3 mm diameter tube with a buffer gas under

6-10 bar backing pressure and expanded into a vacuum chamber. The gas mixture consisted of 0.5–5% precursor ( $\text{O}_2$ ,  $\text{CH}_4$ ,  $\text{C}_2\text{H}_2$ ,  $\text{C}_4\text{H}_2$ ,  $\text{C}_3\text{H}_4$  etc.) with helium as the buffer gas. The mass distribution of the products of ablated titanium in the presence of 5%  $\text{O}_2/\text{He}$  is shown in Figure 3.3.

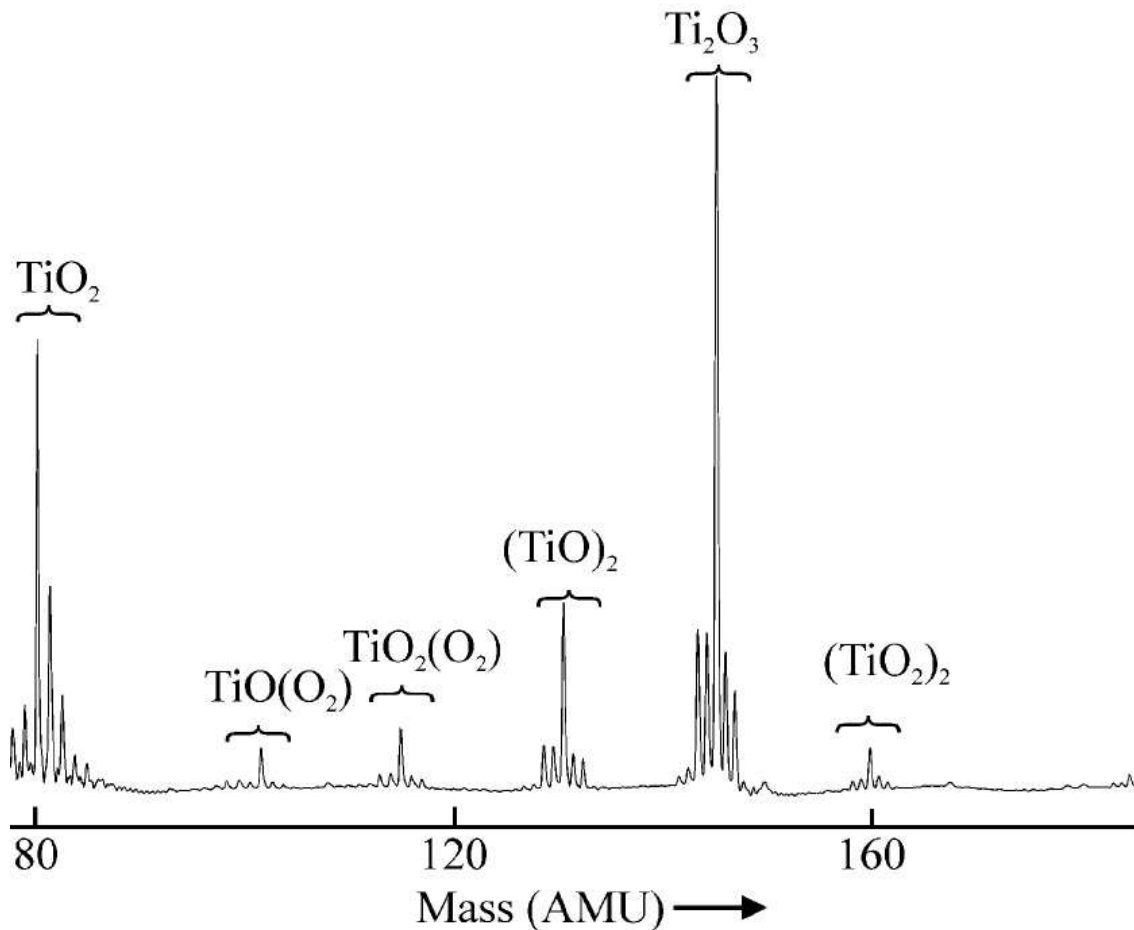


Figure 3.3: Mass spectrum of titanium ablation in the presence of 5%  $\text{O}_2/\text{He}$  at 7.9 eV ionization energy.

### 3.1.2 Discharge Source

The pinhole discharge source (Figure 3.4) is based on the design of Ohshima and Endo [5]. A mixture of 0.5–5% precursor ( $\text{CS}_2$ ,  $\text{CH}_4$ ,  $\text{C}_2\text{H}_2$ ,  $\text{C}_4\text{H}_2$ ,  $\text{C}_3\text{H}_4$  etc.)

with helium as the buffer gas is expanded under 6–10 bar backing pressure into vacuum through the ceramic body. A gas pulse generated by an electromagnetic valve (General Valve 106,  $\varnothing$  0.7) is computer controlled. The amount of gas released is varied by manipulating the width of the opening time. Adjusting this in accord with the pressure in the source chamber allows one to keep the latter constant and thus ensuring stable operating conditions. A 100–200  $\mu$ s long high voltage pulse ( $-700$ – $900$  V) from a homebuilt power supply is applied between the stainless steel or silver electrodes placed on either side of the 2–10 mm thick insulating spacer. The channel has a diameter 1 mm, except for the insulator section where it is enlarged to 2 mm in order to create a localized plasma region. Source stability is better when the outer electrode is grounded while the inner one is pulsed negatively. The whole nozzle system is mounted on an XYZ translation stage, allowing variation around a solid angle sampled by the skimmer. This gives control over the concentrations of species and their rotational temperature during the experiment.

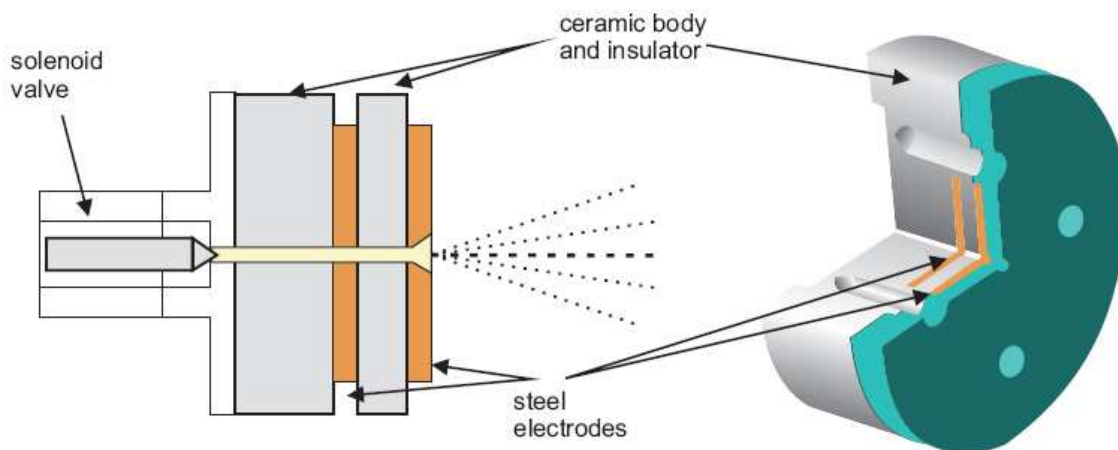


Figure 3.4: Discharge source.

## 3.2 Vacuum System

The experimental apparatus consists of two chambers, a source chamber and a TOF mass spectrometry chamber, separated by a 2 mm diameter skimmer and subjected to differential pumping. The source chamber consists of a large stainless-steel cross-piece (25 cm in diameter and about 15 dm<sup>3</sup> capacity) evacuated by a large turbo-molecular pump (Oerlikon Turbovac T1600, 1550 ls<sup>-1</sup>) being backed by a turbo-pumping station (Pfeifer HiCube 80 Eco, 67 ls<sup>-1</sup>). The pressure obtained in the chamber without operating the molecular source was at the level of  $\sim 10^{-6}$  mbar, and typically  $1-2 \times 10^{-5}$  mbar when operating the source at 20 Hz with a backing pressure of 8 bar. The second chamber hosted the TOF mass spectrometer and ion detector, and required vacuum on the order  $\sim 10^{-7}$  mbar. This requirement is achieved through the use of two turbo-molecular pumps: a 210 ls<sup>-1</sup> Pfeifer TMU261 pump (backed by a 10 m<sup>3</sup>h<sup>-1</sup> mechanical pump, Pfeifer DUO10) is located near the region where the lasers interact with the molecules (extraction plates of TOF) and a 260 ls<sup>-1</sup> Pfeifer HiPace 300 pump (backed by another 10 m<sup>3</sup>h<sup>-1</sup> mechanical pump, Pfeifer DUO10) secures the MCP detector. A set of gauges are employed to indicate vacuum levels in the machine. Low vacuum,  $1000 - 10^{-3}$  mbar, is monitored by Pirani-type gauges (Balzers TPR) whereas high vacuum in the range  $10^{-3} - 10^{-8}$  mbar is diagnosed by Penning ionization gauges (Balzers IKR251). The pressure readings of the gauge in the source chamber are sent via RS232 port to a computer for feedback control of the valve driver program [6] to keep the pressure constant during the experiment.

## 3.3 Light Sources

In the nanosecond time regime, various lasers were used to get the tunable photons required for excitation of molecule on resonance. For low resolution measurements, output in the 210 – 2300 nm range can be obtained from an optical parametric oscillator laser (Ekspla NT342,  $\sim 5$  cm<sup>-1</sup> bandwidth, 10 ns), which is pumped by third harmonic of an in-built Nd<sup>3+</sup>:YAG rod. The high resolution measure-

ments were done using either a single grating dye laser (Lambda Physik Scanmate  $\sim 0.15 \text{ cm}^{-1}$  bandwidth, 370 – 960 nm) or a dual grating dye laser (Continuum Jaguar  $\sim 0.06 \text{ cm}^{-1}$  bandwidth, 400 – 700 nm); both pumped by second/third harmonic of an  $\text{Nd}^{3+}$ :YAG laser (Continuum Powerlite, 10 ns). A tunable UV radiation from 210 – 350 nm can be produced by frequency doubling the output of a dye laser using a BBO crystal. For the ionization step, excimer laser filled with ArF (Lambda Physik RD-EXC-5, 6.4 eV, 2 ns) or  $\text{F}_2$  (Lambda Physik RD-EXC-20, 7.9 eV, 2 ns) was used based on the energy considerations for the molecule under study. All the experiments with ns lasers were done at 20 Hz repetition rate.

In the picosecond regime, photons for both excitation and ionization steps are provided by an  $\text{Nd}^{3+}$ :YAG pumped optical parametric oscillator laser system (Ek-spla 2143 Series/PG421, 10 Hz,  $2 \text{ cm}^{-1}$  bandwidth) with 30 ps pulses. This system has a tunable output in the 210 – 2300 nm range and a fixed wavelength output at either 355 nm or 266 nm, either of which can be used for the ionization step.

For one of the experiments, tunable radiation was produced by Raman shifting the output of a Ti:Sapphire based pulsed amplification system [7] ( $\sim 0.001 \text{ cm}^{-1}$  bandwidth) on the first Anti-stoke's line of  $\text{H}_2$ . The Raman cell consist of a 1.2 m long tube filled with 40 bar of  $\text{H}_2$  and anti-reflection coated glass windows on both ends. The output from the laser is focused inside the cell using a 50 cm focal length lens. On the output end, a band pass filter is used to cut the unscattered and higher order radiation.

A high energy ionization source, with 10.5 eV (118.2 nm) output corresponding to ninth harmonic wavelength of a  $\text{Nd}^{3+}$ :YAG laser, was also developed as part of the study. Herein up to the third harmonic, conversion is carried out in nonlinear crystals (doubling and subsequent mixing) which is followed by tripling in a xenon gas cell. The reason for the popularity of this arrangement comes from the fortunate coincidence of generated wavelength with the region of negative dispersion of xenon caused by the vicinity of the 5p-5d transition of Xe at 119.2 nm. Therefore, achieving the phase-matching condition is possible; these can be tuned by varying the Xe gas pressure [8]. The lack of conversion efficiency due to non-optimal res-

onance match can be compensated by a high intensity of incident radiation. The 10.5 eV radiation was produced by focusing the 355 nm radiation from either a ns (40 – 50 mJ) or ps (2 – 3 mJ) laser onto the centre of an isolated 50-cm long stainless steel gas cell. A quartz Brewster angle window was at the entrance of the gas cell, and  $\sim 23$  cm focal length (at 118.2 nm) MgF<sub>2</sub> lens was located at the exit (vacuum chamber side). This lens also provides the high vacuum seal between the gas cell and the ionization chamber of the vacuum system. Pure xenon, or a mixture of xenon and argon was used to get the desired output at 118.2 nm.

### 3.4 Time-of-Flight Mass Spectrometer

A Wiley-McLaren type TOF mass spectrometer (MS) [9] with double stage acceleration scheme was used during the present studies. The mass resolution of the TOFF-MS is  $\sim 900$ , sufficient to separate ions which differ by one mass unit. A fixed DC voltage of  $-2$  kV is applied on the extraction grids via a potential divider arrangement. By varying the ratio of voltage on the plates, the space focus position can be matched with the detector without changing the times of flight, and, hence, mass calibration. The potential divider arrangement for the current set-up is shown on the top right of Figure 3.6.

### 3.5 Ion Detection

The ion detector used in the experiment is a micro channel plate (MCP) detector, consisting of an array of glass capillaries (10–25  $\mu\text{m}$  inner diameter) that are coated on the inside with an electron-emissive material. The capillaries are biased at a high voltage and like the channeltron, an ion that strikes the inside wall of one of the capillaries creates an avalanche of secondary electrons. This cascading effect creates a gain of  $10^3$  to  $10^4$  and produces a current pulse at the output. Two plates are stacked and connected in series, in a V-shaped configuration, so that the overall gain is  $10^6 - 10^7$ . The MCP detectors provide high temporal resolution, direct conversion, high physical charge amplification, low noise, and pulse-counting



capabilities. The fast response time (in 100 ps range) and flat geometry (effective area diameter of 25 mm) are particularly important for TOF-MS applications.

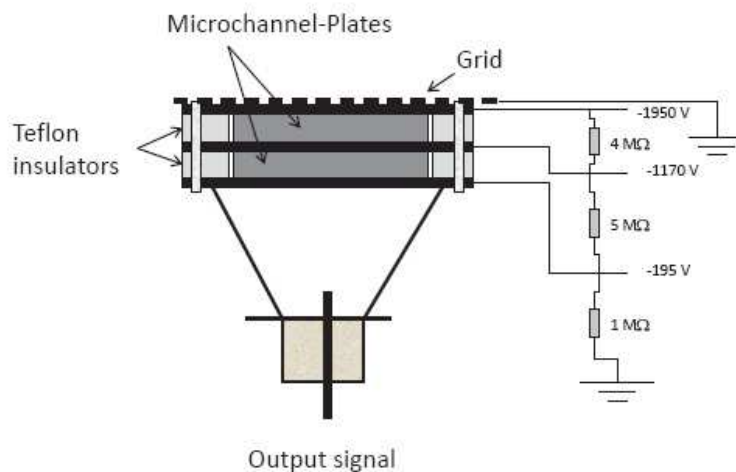


Figure 3.5: Micro channel plate detector.

The detector is operated for positive ion detection (Figure 3.5). Following impact by the positive ion the first plate produces an electron output which is subsequently amplified to more electrons to provide a gain on the ion signal. The detector gain is governed by the potential applied to the plates (0–1 kV per plate). The gain selected is determined by the intensity of the ion signal observed on the oscilloscope and signal saturation is avoided by lowering the detector voltage when necessary. The output of the detector is an electron current that is amplified by a fast, low-noise pre-amplifier and transmitted through a BNC cable to the oscilloscope (LeCroy LT342, 500MHz, 2 channels) where the accumulation and digitalization of the data takes place.

### 3.6 Electrical Arrangement

Figure 3.6 shows the electrical arrangement for the whole setup when the discharge source is in operation. In the case of ablation source, the discharge pulse is replaced

by two trigger pulses to the flash-lamp and Q-switch of the ablation  $\text{Nd}^{3+}:\text{YAG}$  laser.

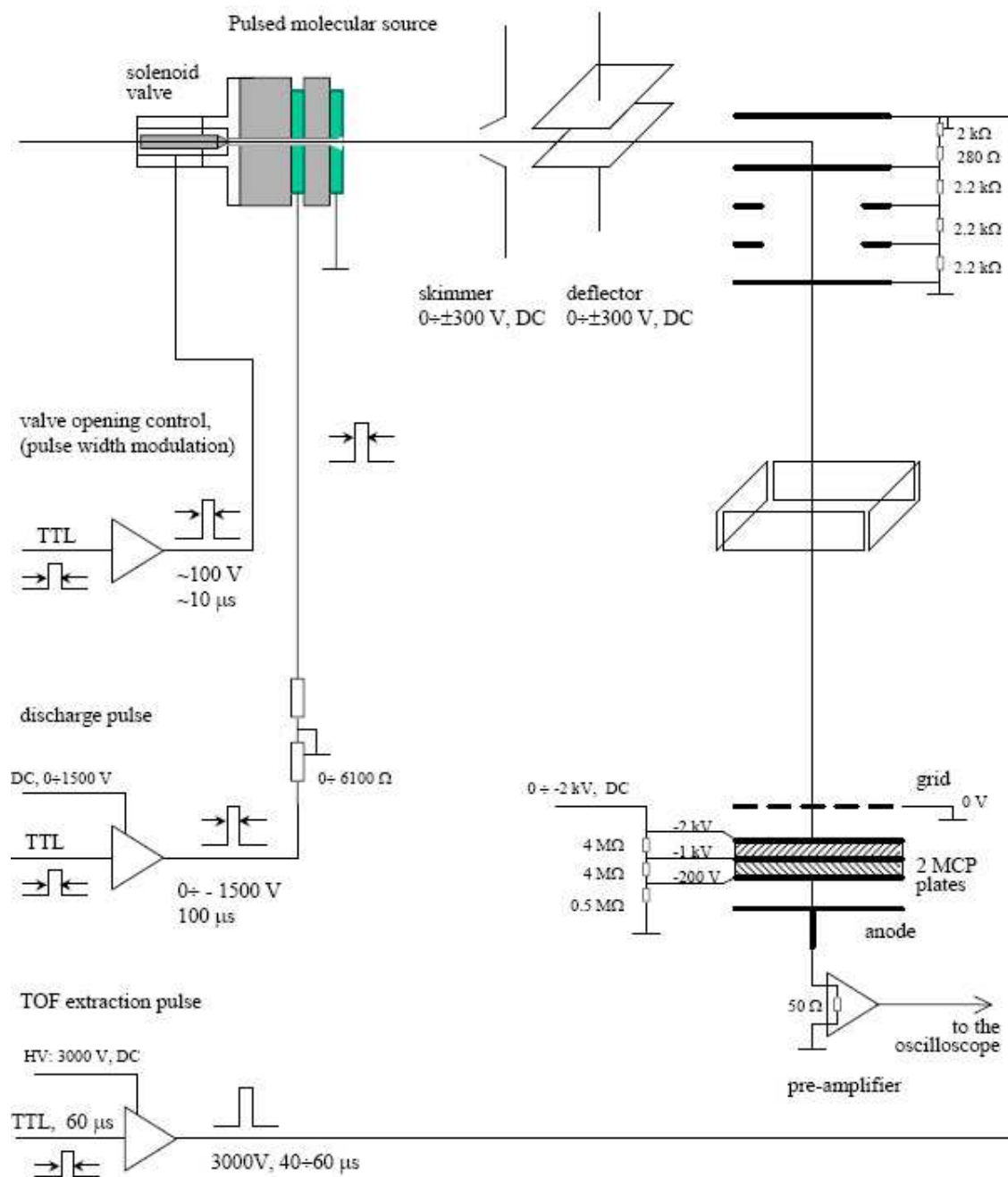


Figure 3.6: Electrical arrangement of the experiment.

## 3.7 Data Handling

Typically 30 laser shots were averaged by the oscilloscope before being transmitted via a GPIB interface to a Linux based computer. The whole data acquisition process is controlled by a program written in LabView. The program can work in two main modes: mass spectrometer and REMPI spectrometer. The first mode allows the user to monitor the evolution of the mass spectrum in near real-time. The computer interrogates the oscilloscope in cycle, requesting it to digitize and average a set number of laser shots, each of which is followed by a complete TOF cycle. The resulting waveform can replace the previous one on the screen of the computer or can be added to it when further signal accumulation is required. The mass calibration is defined by the operator through an empirical assignment of two time delays to the two masses. The calibration entered can be used immediately to convert the mass spectrum's abscissa axis to mass-to-charge ( $m/Z$ ) units. Assessment of correctness of calibration is usually done on basis of integer values for of all, observable mass-peaks. The peak of interest are marked and then mass gates applied either manually or automatically, based on the  $M_0 + iM_1 + jM_2$  template.

In the 'REMPI spectrometer' mode the program records the dependence of the mass-spectrum on the laser wavelength. The computer drives the scanning laser to the next wavelength, programs the oscilloscope on certain given number of accumulation cycles, and downloads the acquired waveform. The integrated intensities of the gated peaks are calculated and stored. The cycle is looped and the laser is tuned to the next wavelength. The mass-peak area is proportional to the ion current of the ions with a specific mass, and, in turn, to the ionization efficiency of the corresponding neutral species. The variation of the peak area versus laser wavelength provides the REMPI spectrum of the molecule.

# Bibliography

- [1] T. G. Dietz, M. A. Duncan, D. E. Powers, and R. E. Smalley. Laser production of supersonic metal cluster beams. *Journal of Chemical Physics*, 74:6511–6512, 1981.
- [2] D. E. Powers, S. G. Hansen, M. E. Geusic, A. C. Puiu, J. B. Hopkins, T. G. Dietz, M. A. Duncan, P. R. R. Langridgesmith, and R. E. Smalley. Supersonic metal cluster beams: laser photo-ionization studies of  $\text{Cu}_2$ . *Journal of Physical Chemistry*, 86:2556–2560, 1982.
- [3] P. Milani and W. A. Deheer. Improved pulsed laser vaporization source for production of intense beams of neutral and ionized clusters. *Review of Scientific Instruments*, 61:1835–1838, 1990.
- [4] E. F. Rexer, M. P. Joshi, R. L. DeLeon, P. N. Prasad, and J. F. Garvey. A reactive laser ablation source for the production of thin films. *Review of Scientific Instruments*, 69:3028–3030, 1998.
- [5] Y. Ohshima and Y. Endo. Structure of  $\text{C}_3\text{S}$  studied by pulsed-discharge-nozzle Fourier-transform microwave spectroscopy. *Journal of Molecular Spectroscopy*, 153:627–634, 1992.
- [6] T. Motylewski. *Cavity Ringdown Spectroscopy of Transient Species*. PhD thesis, University of Basel, Basel, Switzerland, 2001.
- [7] R. Chauhan. *Development and Application of Laser Methods for Electronic Spectroscopy of Radicals*. PhD thesis, University of Basel, Basel, Switzerland, 2010.

- [8] A. H. Kung, J. F. Young, and S. E. Harris. Generation of 1182 radiation in phase-matched mixtures of inert-gases. *Applied Physics Letters*, 22:301–302, 1973.
- [9] W. C. Wiley and I. H. McLaren. Time-of-flight mass spectrometer with improved resolution. *Review of Scientific Instruments*, 26:1150–1157, 1955.

# 4 Silver monosulfide

The spectroscopic information about AgS is limited as there are no reported experimental studies and just a few theoretical calculations. Ab initio calculations and isovalent arguments suggest that AgS has a similar order of electronic states as AgO [1]. The ground state has been calculated to be  $^2\Pi$  with an electronic configuration  $1\sigma^2 1\delta^4 1\pi^4 2\sigma^2 2\pi^3$  [1, 2]. Furthermore, the calculations at CASSCF level predict the first excited state,  $^2\Sigma^+$  to lie  $\sim 10\,500\text{ cm}^{-1}$  above the ground state [1]. A density functional approach at the MCPF-ANO level of theory gave a bond length of 237 pm and a vibrational frequency of  $319\text{ cm}^{-1}$  for the  $X^2\Pi$  state. The calculated values for the  $A^2\Sigma^+$  state were 230 pm and  $294\text{ cm}^{-1}$  [1].

## 4.1 Experimental

The details of the experimental setup are given in Chapter 3. Briefly, helium seeded with 0.5%  $\text{CS}_2$ , at a backing pressure of 10 bar, was expanded through a DC discharge source, consisting of two silver electrodes with a one mm hole separated by a 2 mm insulator. A  $10\ \mu\text{s}$  (700 V, 100 mA) pulse was applied between the electrodes producing Ag atoms that react with  $\text{CS}_2$  to form AgS. The neutral molecules were irradiated with a tunable laser followed by 7.87 eV photons from an  $\text{F}_2$  (for near-IR transitions) or 6.42 eV photons from an ArF (for UV transitions) excimer laser to ionize the excited molecules. An optical parametric oscillator laser with a resolution of  $\sim 5\text{ cm}^{-1}$  was used to record the low resolution vibronic spectrum and a  $\sim 0.15\text{ cm}^{-1}$  bandwidth dye laser, to measure the rotationally resolved spectra. The calculated ionization potential of AgS is 8.46 eV [2].

## 4.2 Calculations

Ab initio calculations were performed with the GAMESS package [3,4], to obtain the transition energies, symmetry, bond lengths, vibrational frequencies and spin-orbit coupling constants for different electronic states. The MCSCF method was used, chosen with an active space of 10 molecular orbitals in which 11 electrons were distributed. The ECP basis set was selected as SBKJC with 3p, 3d and 1f. The results are in Table 4.1; the states with no bond length listed, have a repulsive potential. Because the variation of energy with bond length is relatively small, these might have a minimum with more sophisticated methods, as already mentioned in Ref. 1. The negative sign of the spin-orbit coupling constant indicates that the term is inverted.

Table 4.1: Calculated spectroscopic constants for low-lying electronic states of AgS at the MCSCF-SBKJC level of theory.

State	$r_e/\text{pm}$	$\omega_e/\text{cm}^{-1}$	$A_{\text{so}}/\text{cm}^{-1}$	$T_e/\text{cm}^{-1}$
$X^2\Pi$	244 (237)	295 (319)	-370	-
$A^2\Sigma^+$	245 (230)	263 (294)	-	8 998 (10 457)
$B^2\Sigma^-$	-	-	-	11 852 (16 601)
$(1)^2\Delta$	-	-	-2	20 411 (25 520)
$(2)^2\Pi$	-	-	-78	23 484 (23 527)
$(3)^2\Pi$	359		-173	30 946 (29 633)

Values in parentheses are the calculated values in Ref. 1.

## 4.3 Results

There are two stable naturally occurring isotopes of silver:  $^{107}\text{Ag}$  (51.84%) and  $^{109}\text{Ag}$  (48.16%) and four of sulfur:  $^{32}\text{S}$  (95.02%),  $^{33}\text{S}$  (0.75%),  $^{34}\text{S}$  (4.21%) and  $^{36}\text{S}$  (0.02%). The [1+1'] resonance enhanced multiphoton ionization (REMPI) mass spectrum shows two strong peaks of almost equal intensity at  $m/Z$  139 and 141 and a weak feature at  $m/Z$  143 which are assigned to  $^{107}\text{Ag}^{32}\text{S}$ ,  $^{109}\text{Ag}^{32}\text{S}$  and

$^{109}\text{Ag}^{34}\text{S}$ , respectively. By setting the mass gates on these peaks, it was possible to record the spectra of all three isotopomers simultaneously.

### 4.3.1 Electronic transitions in the near-infrared

The low resolution, mass-selected  $[1+1']$  REMPI spectrum of  $^{107}\text{Ag}^{32}\text{S}$ , in the  $9\,500\text{ cm}^{-1}$  to  $11\,500\text{ cm}^{-1}$  range is presented in Figure 4.1(A). Five bands of varying intensity are observed; a strong one at  $\sim 10\,520\text{ cm}^{-1}$ , two with medium intensity on either side of it at  $\sim 10\,043\text{ cm}^{-1}$  and  $\sim 10\,835\text{ cm}^{-1}$ , and two weak ones at  $\sim 10\,196\text{ cm}^{-1}$  and  $\sim 10\,353\text{ cm}^{-1}$ . The transitions at  $10\,520\text{ cm}^{-1}$  and  $10\,835\text{ cm}^{-1}$  were recorded at  $0.15\text{ cm}^{-1}$  resolution, as shown in Figure 4.1(B). Here, the sequence bands can also be observed to the red. The features at  $10\,043\text{ cm}^{-1}$ ,  $10\,196\text{ cm}^{-1}$  and  $10\,353\text{ cm}^{-1}$  could not be recorded at higher resolution due to the limitations of the dye laser in the near-infrared.

MCPF-ANO calculations [1] predict the AgS ground state to have  $^2\Pi$  symmetry, while  $A^2\Sigma^+$  state is estimated to lie at  $\sim 10\,900\text{ cm}^{-1}$ , quite close to the observed band system. Furthermore, the observed bands are blue-shaded, consistent with the small decrease in Ag–S internuclear separation that has been calculated. The assignment of the band system to the calculated  $A^2\Sigma^+ - X^2\Pi_i$  transition is supported by the analysis below.

**Vibronic Analysis:** Using combination differences, the bands at  $10\,196\text{ cm}^{-1}$ ,  $10\,520\text{ cm}^{-1}$  and  $10\,835\text{ cm}^{-1}$ , along with the corresponding sequence bands to the red, can be ascribed to the same vibronic system with 0–0 at  $10\,520\text{ cm}^{-1}$ , 1–0 at  $10\,835\text{ cm}^{-1}$  and 0–1 at  $10\,196\text{ cm}^{-1}$ . The other two observed features at  $10\,043\text{ cm}^{-1}$  and  $10\,353\text{ cm}^{-1}$  are separated by  $\sim 480\text{ cm}^{-1}$  from the peaks at  $10\,520\text{ cm}^{-1}$  and  $10\,835\text{ cm}^{-1}$ . This is due to the spin-orbit splitting of  $477(8)\text{ cm}^{-1}$  in the  $X^2\Pi$  ground state, which is inverted according to the calculations and in comparison with isovalent AgO [5] and CuS [6].

The bands at  $10\,520\text{ cm}^{-1}$  and  $10\,043\text{ cm}^{-1}$  are assigned to the  $\Omega'' = 3/2$  and  $\Omega'' = 1/2$  spin-orbit components of the  $A^2\Sigma^+ - X^2\Pi$  0–0 transition, respectively. The peaks at  $10\,835\text{ cm}^{-1}$  and  $10\,353\text{ cm}^{-1}$  originate from the 1–0 vibronic tran-



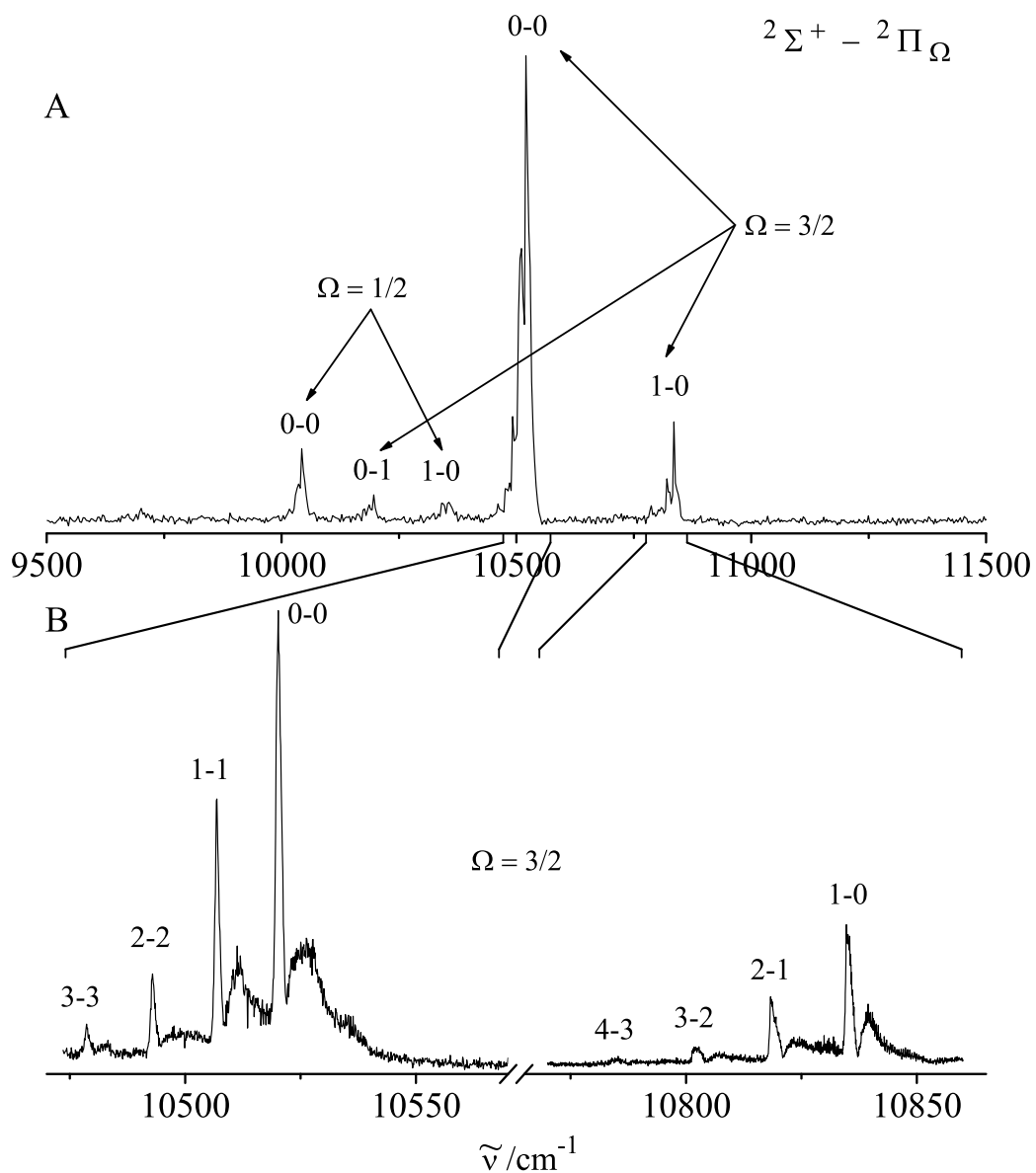


Figure 4.1: (A) Mass-selected [1+1'] resonance enhanced multiphoton ionization spectrum of the  $A^2\Sigma^+ - X^2\Pi_i$  electronic transition of  $^{107}\text{Ag}^{32}\text{S}$  at 5  $\text{cm}^{-1}$  resolution; (B) The  $\Omega'' = 3/2$  component of the 0-0 and 1-0 transitions along with the sequence bands, recorded with 0.15  $\text{cm}^{-1}$  laser bandwidth.

Table 4.2: Band maxima and isotopic shifts (in  $\text{cm}^{-1}$ ) for the  $A^2\Sigma^+ - X^2\Pi$  electronic transition of  $^{107}\text{Ag}^{32}\text{S}$ ,  $^{109}\text{Ag}^{32}\text{S}$  and  $^{109}\text{Ag}^{34}\text{S}$ .

$^{107}\text{Ag}^{32}\text{S}$			$^{109}\text{Ag}^{32}\text{S}$			$^{109}\text{Ag}^{34}\text{S}$		
Band <sup>a</sup>	Offset <sup>b</sup>		Band <sup>a</sup>	Isotopic shift <sup>c</sup>		Band <sup>a</sup>	Isotopic shift <sup>d</sup>	
				Obs.	Calc.		Obs.	Calc.
$A^2\Sigma^+ - X^2\Pi_{3/2}$								
0-1	10 196(8)	-324	10 196(8)					
3-3	10 478.52	-41.65	10 478.63	0.11	0.10			
2-2	10 492.84	-27.33	10 492.90	0.06	0.07	10 493.56	0.72	0.81
1-1	10 506.71	-13.46	10 506.76	0.05	0.04	10 507.32	0.61	0.49
0-0	10 520.17	0	10 520.17	0.00	0.01	10 520.33	0.16	0.16
4-3	10 785.27	265.10	10 784.63	-0.64	-0.58			
3-2	10 802.72	282.55	10 801.90	-0.82	-0.60			
2-1	10 818.29	298.12	10 817.71	-0.58	-0.63	10 811.44	-6.85	-7.47
1-0	10 834.74	314.57	10 834.03	-0.71	-0.66	10 827.15	-7.59	-7.80
$A^2\Sigma^+ - X^2\Pi_{1/2}$								
0-0	10 043(8)	-477	10 043(8)					
1-0	10 353(8)	-167	10 353(8)					

<sup>a</sup> Error in measurement is  $0.05 \text{ cm}^{-1}$  unless stated otherwise.

<sup>b</sup> Shift from the  $10\,520.17 \text{ cm}^{-1}$  band.

<sup>c</sup>  $\tilde{\nu}^{109}\text{Ag}^{32}\text{S} - \tilde{\nu}^{107}\text{Ag}^{32}\text{S}$ .

<sup>d</sup>  $\tilde{\nu}^{109}\text{Ag}^{34}\text{S} - \tilde{\nu}^{107}\text{Ag}^{32}\text{S}$ .

Table 4.3: Vibrational constants (in  $\text{cm}^{-1}$ ) for the  $X^2\Pi$  and  $A^2\Sigma^+$  states of  $\text{AgS}$ .

	$^{107}\text{Ag}^{32}\text{S}$	$^{109}\text{Ag}^{32}\text{S}$	$^{109}\text{Ag}^{34}\text{S}$
$X^2\Pi$			
$\omega_e''$	331.6(2)	331.0(2)	323.1(3)
$\omega_e x_e''$	1.3(1)	1.3(1)	1.0(3)
$A^2\Sigma^+$			
$T_e$	10 528.3(2)	10 528.3(2)	10 528.2(3)
$\omega_e'$	318.4(1)	317.6(1)	310.1(3)
$\omega_e x_e'$	1.4(1)	1.4(1)	1.2(3)

sition and that at  $10\,196 \text{ cm}^{-1}$  corresponds to the  $\Omega'' = 3/2$  component of the 0-1 band. The presence of a short vibrational progression with the appearance of just

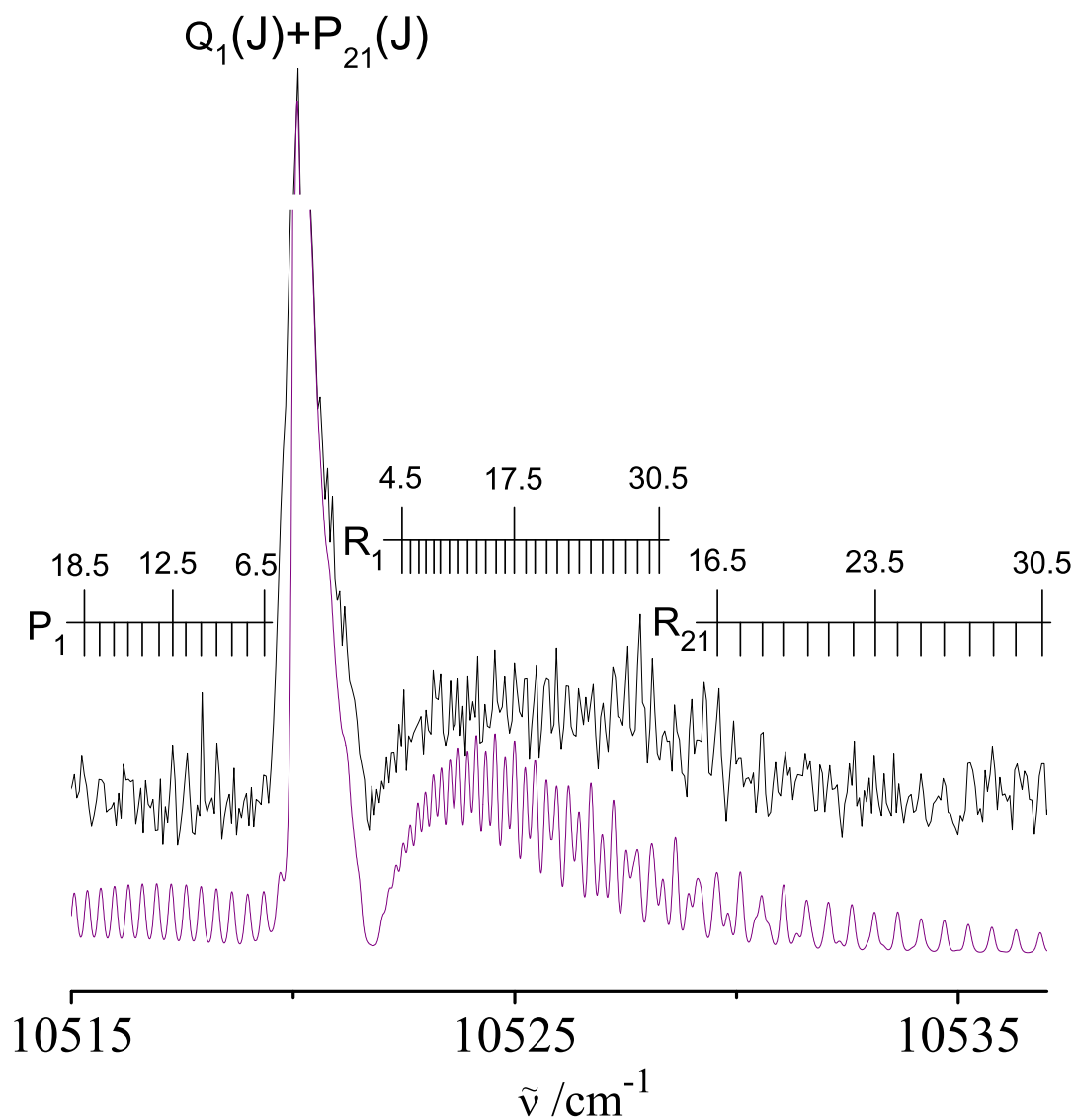


Figure 4.2: The  $\Omega'' = 3/2$  component of the  $A^2\Sigma^+ - X^2\Pi$  0–0 transition of  $^{107}\text{Ag}^{32}\text{S}$ . The lower trace shows the simulation at 80 K rotational temperature with Gaussian and Lorentzian line widths of  $0.12\text{ cm}^{-1}$  and  $0.06\text{ cm}^{-1}$ , respectively.

$v = 0$  and  $v = 1$  levels in the excited state results from good Frank-Condon overlap between the  $X^2\Pi$  and  $A^2\Sigma^+$  states. The transition frequencies of the band maxima for the recorded vibronic bands of  $^{107}\text{Ag}^{32}\text{S}$ ,  $^{109}\text{Ag}^{32}\text{S}$  and  $^{109}\text{Ag}^{34}\text{S}$ , along

with the respective assignments are given in Table 4.2. The isotope shifts are also compared to the calculated values.

The  $\Omega'' = 3/2$  component of the vibronic transition is fitted to obtain the harmonic vibrational frequency,  $\omega_e'' = 331.6(2) \text{ cm}^{-1}$  and the anharmonic term,  $\omega_e x_e'' = 1.3(1) \text{ cm}^{-1}$  for the ground state, as well as the band origin,  $T_e = 10528.3(2) \text{ cm}^{-1}$ ,  $\omega_e' = 318.4(1) \text{ cm}^{-1}$ ,  $\omega_e x_e' = 1.4(1) \text{ cm}^{-1}$  for the excited state of  $^{107}\text{Ag}^{32}\text{S}$ . The vibrational constants obtained for  $^{107}\text{Ag}^{32}\text{S}$ ,  $^{109}\text{Ag}^{32}\text{S}$  and  $^{109}\text{Ag}^{34}\text{S}$  are listed in Table 4.3.

**Rotational Analysis:** Figures 4.2 and 4.3 show the rotationally resolved spectra of the  $A^2\Sigma^+ - X^2\Pi_{3/2}$  component of 0–0 and 1–0 bands, for  $^{107}\text{Ag}^{32}\text{S}$ . The rotational profile fits were carried out with the PGOPHER software [7]. The fit of the 1–0 band was performed while varying the spectroscopic constants for both the lower and upper states. This gives the rotational constant,  $B'' = 0.13126(16) \text{ cm}^{-1}$  and the centrifugal distortion constant,  $D'' = 5.5(17) \times 10^{-7} \text{ cm}^{-1}$  for the ground state and  $B' = 0.13295(14) \text{ cm}^{-1}$  and  $D' = 5.4(13) \times 10^{-7} \text{ cm}^{-1}$  for the excited state. For the case of the 0–0 band, the lower state molecular constants were fixed to the values obtained from the fit of the 1–0 transition while the upper state constants were varied, to obtain  $B' = 0.13370(4) \text{ cm}^{-1}$  and  $D' = 3.9(3) \times 10^{-7} \text{ cm}^{-1}$ . The small change in the rotational constant between the  $X^2\Pi$  and  $A^2\Sigma^+$  states is in-line with the dominant Frank-Condon factor for the 0–0 transition. Simulations were carried out at a rotational temperature of 80 K, and used  $0.12 \text{ cm}^{-1}$  Gaussian and  $0.06 \text{ cm}^{-1}$  Lorentzian line widths, which fitted best the profiles of the peaks. The high  $J$  lines for the  $P$ -branch overlap with those of  $R$  of the respective hot bands and were left out of the fits. Intensity variations in the rotational profile are caused by fluctuations in the DC discharge. The rotational spectroscopic constants obtained for  $^{107}\text{Ag}^{32}\text{S}$  and  $^{109}\text{Ag}^{32}\text{S}$ , are listed in Table 4.4.

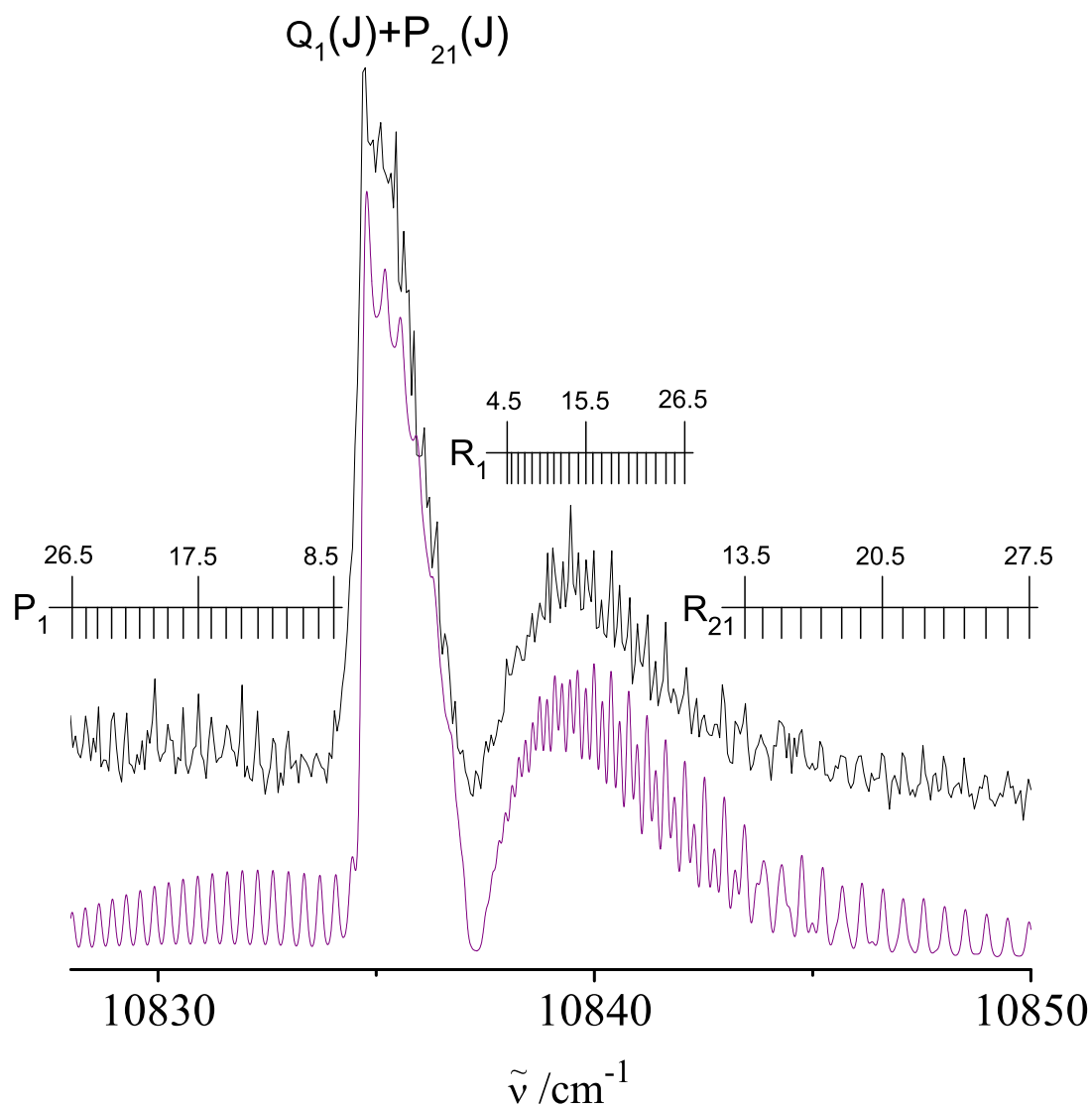


Figure 4.3: The  $\Omega'' = 3/2$  component of the  $A^2\Sigma^+ - X^2\Pi$  1–0 transition of  $^{107}\text{Ag}^{32}\text{S}$ . The lower trace shows the simulation with the same parameters as Figure 4.2.

### 4.3.2 Electronic transitions in the ultraviolet

[1+1'] REMPI spectrum of AgS was recorded in the UV from  $24000 \text{ cm}^{-1}$  to  $47500 \text{ cm}^{-1}$  at  $8 \text{ cm}^{-1}$  laser bandwidth. Several electronic systems were observed in this region, as can be seen in Figures 4.4, 4.5, 4.6, 4.7 and 4.8. Vibronic pro-

Table 4.4: Molecular constants (in  $\text{cm}^{-1}$ ) for the  $X^2\Pi$  and  $A^2\Sigma^+$  states of AgS.

$X^2\Pi$		$A^2\Sigma^+$	
v=0		v=0	v=1
$^{107}\text{Ag}^{32}\text{S}$			
$T_0$		10 521.662(7)	10 837.124(8)
$A_{so}$	- 477(8)	-	-
$B$	0.131 26(16)	0.133 70(4)	0.132 95(14)
$D$	$5.5(17) \times 10^{-7}$	$3.9(3) \times 10^{-7}$	$5.4(13) \times 10^{-7}$
$^{107}\text{Ag}^{34}\text{S}$			
$T_0$		10 521.656(7)	10 836.482(9)
$A_{so}$	- 477(8)	-	-
$B$	0.130 90(18)	0.133 42(3)	0.132 44(16)
$D$	$7.0(15) \times 10^{-7}$	$6.3(3) \times 10^{-7}$	$5.4(14) \times 10^{-7}$

gressions have been identified for several electronic transitions up to  $40\,500\text{ cm}^{-1}$ . The assignment of the lower energy terminus as a  $X^2\Pi$  state for all transitions is indisputable because of the cold sample conditions and absence of any low lying electronic states. The excited electronic state of these transitions can only be determined from rotational analysis of the high resolution spectra or accurate high level calculations, both of which are currently unavailable.

Figure 4.4 (A) presents the electronic spectrum of  $^{107}\text{Ag}^{32}\text{S}$  in the  $25\,000\text{ cm}^{-1}$  to  $27\,000\text{ cm}^{-1}$  region. Vibronic analysis of the observed bands shows two distinct progressions with frequencies  $\sim 195\text{ cm}^{-1}$  and  $\sim 140\text{ cm}^{-1}$ . The origin of the electronic system with  $\omega' \approx 195\text{ cm}^{-1}$  is identified at  $25\,753\text{ cm}^{-1}$ . The location of the band origin of the other system is ambiguous due to overlapping features from the first system; however, has been tentatively assigned to the band at  $25\,667\text{ cm}^{-1}$ .

High resolution measurements were also performed in the  $25\,515\text{ cm}^{-1}$  to  $26\,215\text{ cm}^{-1}$  region, using a  $0.15\text{ cm}^{-1}$  bandwidth laser. The obtained spectrum (Figure 4.4 (B)) is complicated due to presence of two overlapping electronic systems. Efforts are underway to assign the rotational lines in this spectrum and obtain the molecular symmetry and constants for both the excited states.

Figure 4.5 presents the electronic spectrum of  $^{107}\text{Ag}^{32}\text{S}$  in the  $28\,500\text{ cm}^{-1}$  to  $31\,500\text{ cm}^{-1}$  region. For the system between  $29\,000\text{ cm}^{-1}$  to  $30\,000\text{ cm}^{-1}$ , three dis-

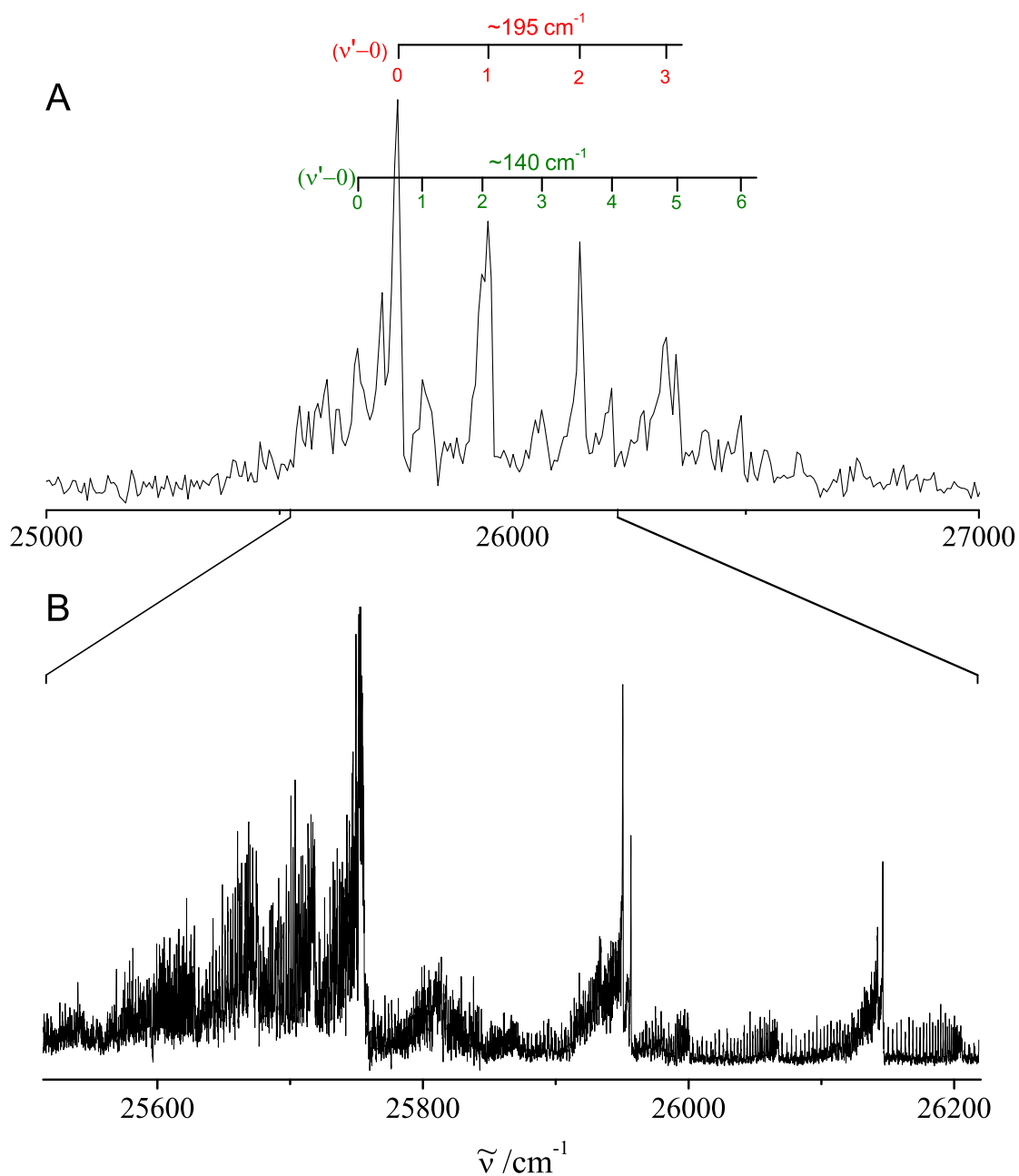


Figure 4.4: Mass-selected [1+1'] resonance enhanced multi-photon ionization spectrum of  $^{107}\text{Ag}^{32}\text{S}$  in the (A) 25 000 - 27 000  $\text{cm}^{-1}$  region, recorded with 8  $\text{cm}^{-1}$  laser bandwidth; (B) 25 515 - 26 215  $\text{cm}^{-1}$  region, recorded with 0.15  $\text{cm}^{-1}$  laser bandwidth.

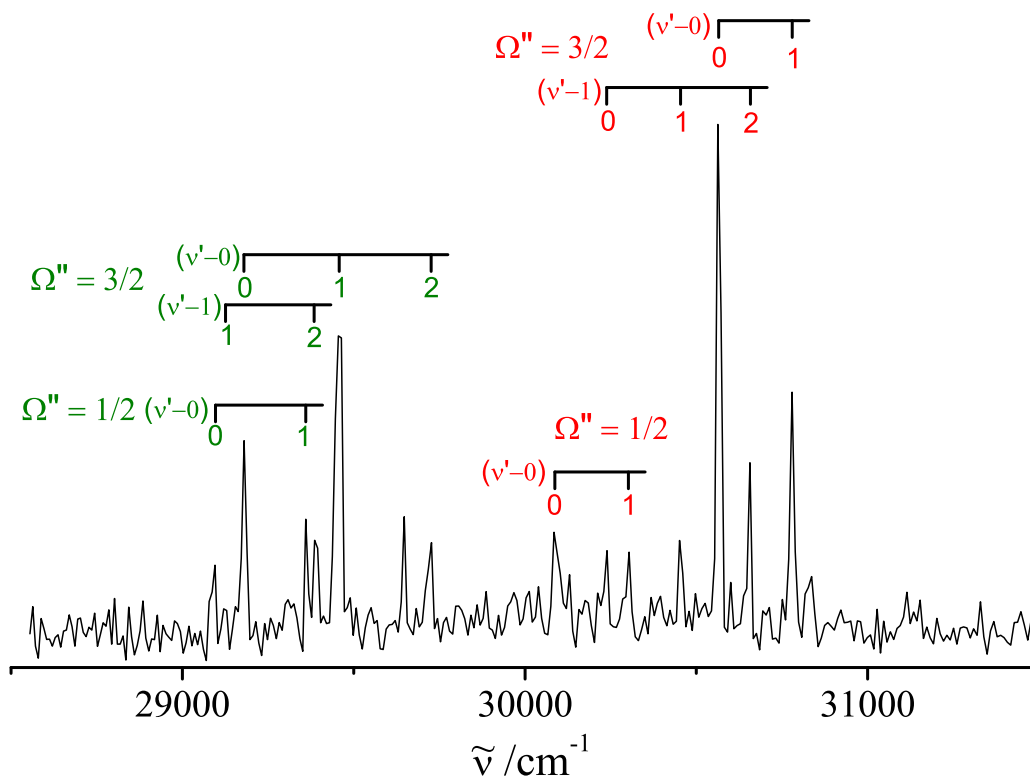


Figure 4.5: Mass-selected  $[1+1']$  resonance enhanced multi-photon ionization spectrum of  $^{107}\text{Ag}^{32}\text{S}$  in the  $28\,500 - 31\,500\text{ cm}^{-1}$  region.

tinct progressions with a frequency  $\sim 270\text{ cm}^{-1}$  are identified. These progressions originate from  $29\,095\text{ cm}^{-1}$ ,  $29\,120\text{ cm}^{-1}$  and  $29\,180\text{ cm}^{-1}$ . Based on combination differences and intensity of bands,  $29\,180\text{ cm}^{-1}$  and  $29\,120\text{ cm}^{-1}$  are identified as  $\Omega'' = 3/2$  component of the  $0-0$  and  $1-1$  transitions, respectively. The peak at  $29\,095\text{ cm}^{-1}$  is assigned to the  $\Omega'' = 1/2$  component of the  $0-0$  transition, indicating a spin-orbit coupling term,  $A_{so}' \approx -392\text{ cm}^{-1}$  for the excited state. Similar analysis of the bands from  $30\,000\text{ cm}^{-1}$  to  $31\,000\text{ cm}^{-1}$  leads to assignment of the peaks at  $30\,563\text{ cm}^{-1}$  and  $30\,086\text{ cm}^{-1}$  as  $\Omega'' = 3/2$  and  $\Omega'' = 1/2$  components of the  $0-0$  transition, respectively. A difference of  $-477\text{ cm}^{-1}$  between the spin-orbit components, as observed for the  $A^2\Sigma^+ - X^2\Pi$  transition, indicates a  $\Sigma$  excited



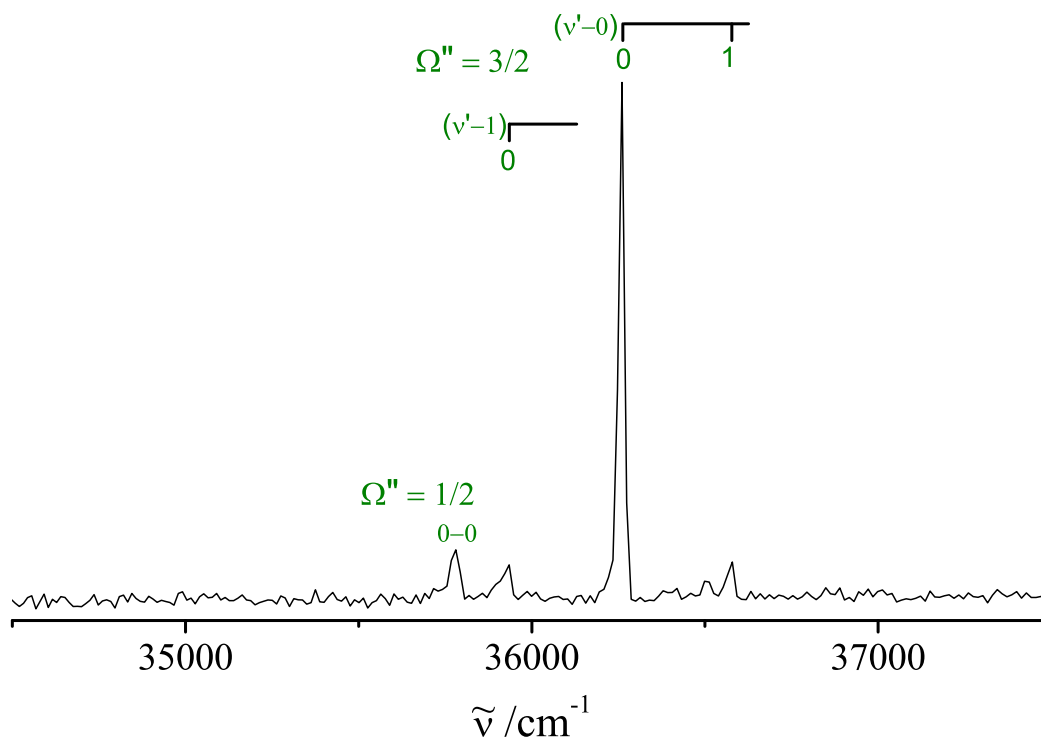


Figure 4.6: Mass-selected [1+1'] resonance enhanced multi-photon ionization spectrum of  $^{107}\text{Ag}^{32}\text{S}$  in the 34500 - 37500  $\text{cm}^{-1}$  region.

state for this particular transition. The stretching frequency for the excited state is determined to be  $\omega' \approx 215 \text{ cm}^{-1}$ .

The bands observed further to the UV in the 32000 – 40000  $\text{cm}^{-1}$  region were analysed like-wise and the identified vibronic progressions are marked in Figures 4.6 and 4.7. The transition wavenumbers of all the observed UV transitions up to 40500  $\text{cm}^{-1}$  are given in Table 4.5. Beyond 40500  $\text{cm}^{-1}$  the vibronic spectrum becomes extremely complicated due to high density of electronic states, as shown in Figure 4.8.

Table 4.5: Band maxima (in  $\text{cm}^{-1}$ ) for the observed ultraviolet transition of  $^{107}\text{Ag}^{32}\text{S}$ .

Assignment $\nu' - \nu''$	Observed wavenumber	Offset	Assignment $\nu' - \nu''$	Observed wavenumber	Offset
0-0 ( $\Omega'' = 3/2$ )	25 667	0	0-0 ( $\Omega'' = 1/2$ )	30 085	-478
1-0 ( $\Omega'' = 3/2$ )	25 806	139	1-0 ( $\Omega'' = 3/2$ )	30 239	-324
2-0 ( $\Omega'' = 3/2$ )	25 934	267	1-0 ( $\Omega'' = 1/2$ )	30 303	-260
3-0 ( $\Omega'' = 3/2$ )	26 062	395	1-1 ( $\Omega'' = 3/2$ )	30 451	-112
4-0 ( $\Omega'' = 3/2$ )	26 212	545	0-0 ( $\Omega'' = 3/2$ )	30 563	0
5-0 ( $\Omega'' = 3/2$ )	26 350	683	2-1 ( $\Omega'' = 3/2$ )	30 657	94
6-0 ( $\Omega'' = 3/2$ )	26 490	823	1-0 ( $\Omega'' = 3/2$ )	30 779	216
0-0 ( $\Omega'' = 3/2$ )	25 753	0	0-0 ( $\Omega'' = 1/2$ )	35 780	-481
1-0 ( $\Omega'' = 3/2$ )	25 947	194	0-1 ( $\Omega'' = 3/2$ )	35 935	-326
2-0 ( $\Omega'' = 3/2$ )	26 144	391	0-0 ( $\Omega'' = 3/2$ )	36 261	0
3-0 ( $\Omega'' = 3/2$ )	26 330	571	1-0 ( $\Omega'' = 3/2$ )	36 579	318
0-0 ( $\Omega'' = 1/2$ )	29 095	-85	0-0 ( $\Omega'' = 3/2$ )	38 569	0
1-1 ( $\Omega'' = 3/2$ )	29 121	-59	1-1 ( $\Omega'' = 3/2$ )	38 628	59
0-0 ( $\Omega'' = 3/2$ )	29 180	0	1-0 ( $\Omega'' = 3/2$ )	38 944	375
1-0 ( $\Omega'' = 1/2$ )	29 360	180	2-1 ( $\Omega'' = 3/2$ )	39 005	436
2-1 ( $\Omega'' = 3/2$ )	29 386	206	2-0 ( $\Omega'' = 3/2$ )	39 342	773
1-0 ( $\Omega'' = 3/2$ )	29 445	265	3-0 ( $\Omega'' = 3/2$ )	39 702	1 133
2-0 ( $\Omega'' = 3/2$ )	29 727	547	0-0 ( $\Omega'' = 1/2$ )	39 435	-473
			0-0 ( $\Omega'' = 3/2$ )	39 908	0
			1-0 ( $\Omega'' = 3/2$ )	40 278	370

## 4.4 Discussion

The ground  $X^2\Pi_i$  electronic state of AgS is represented by the configuration  $1\sigma^2 1\delta^4 1\pi^4 2\sigma^2 2\pi^3$ . An electronic transition to  $A^2\Sigma^+$  state involves excitation of a  $2\sigma$  electron to the  $2\pi$  orbital resulting in an excited electronic configuration of  $1\sigma^2 1\delta^4 1\pi^4 2\sigma^1 2\pi^4$ .

Calculations predict similar electronic properties for AgS and AgO; the major difference being a lesser ionic character for AgS [1]. The spin-orbit coupling constant provides some proof for covalency. If only the ionic  $\text{Ag}^+\text{S}^-$  configu-

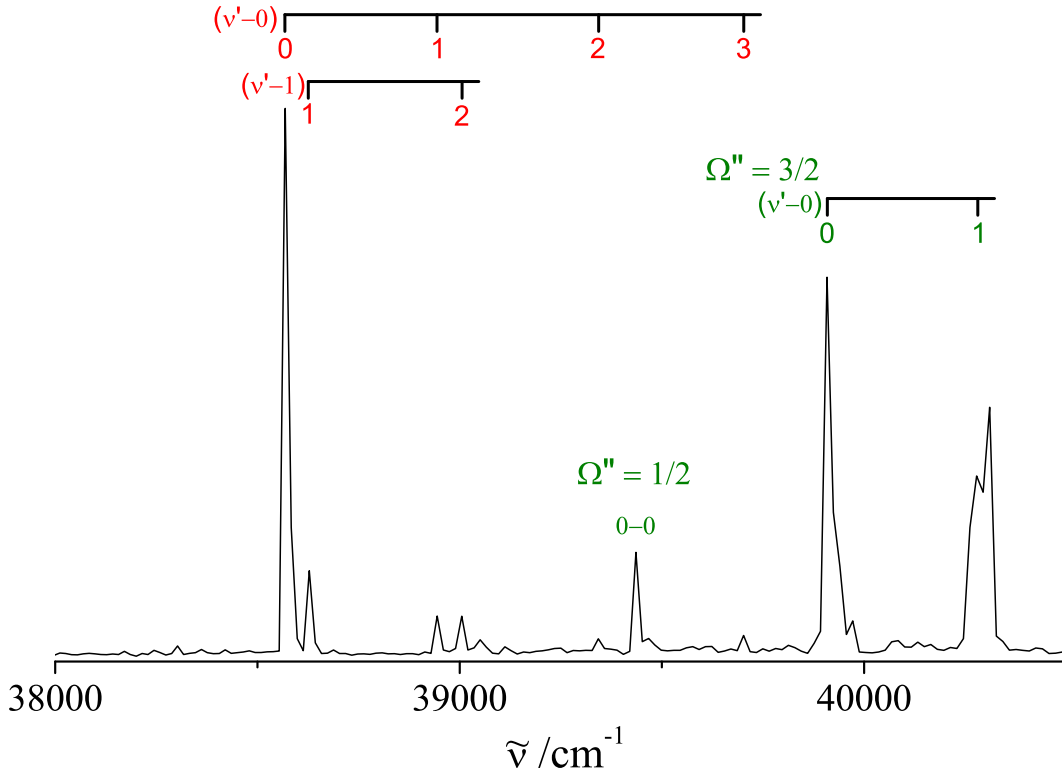
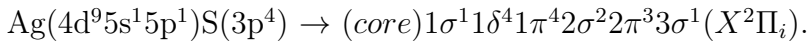
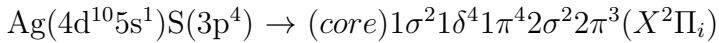
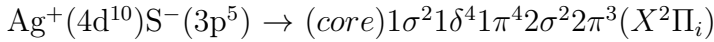


Figure 4.7: Mass-selected  $[1+1']$  resonance enhanced multi-photon ionization spectrum of  $^{107}\text{Ag}^{32}\text{S}$  in the 38 000 - 40 500  $\text{cm}^{-1}$  region.

ration was present, then the spin-orbit coupling constant would reflect that of  $\text{S}^-$ ,  $\zeta = 326 \text{ cm}^{-1}$  [8]. Instead the observed value for the  $X^2\Pi_i$  state of AgS is  $-477(8) \text{ cm}^{-1}$  and thus there is a contribution from other configurations.

The  $X^2\Pi_i$  spin-orbit coupling constant for AgS ( $-477 \text{ cm}^{-1}$ ) is quite similar to isovalent CuS ( $-433 \text{ cm}^{-1}$ ) [9]. Based on an analogous treatment, the  $X^2\Pi_i$  state of AgS is considered to be represented by a dominant ionic  $\text{Ag}^+\text{S}^-$  and two covalent configurations.



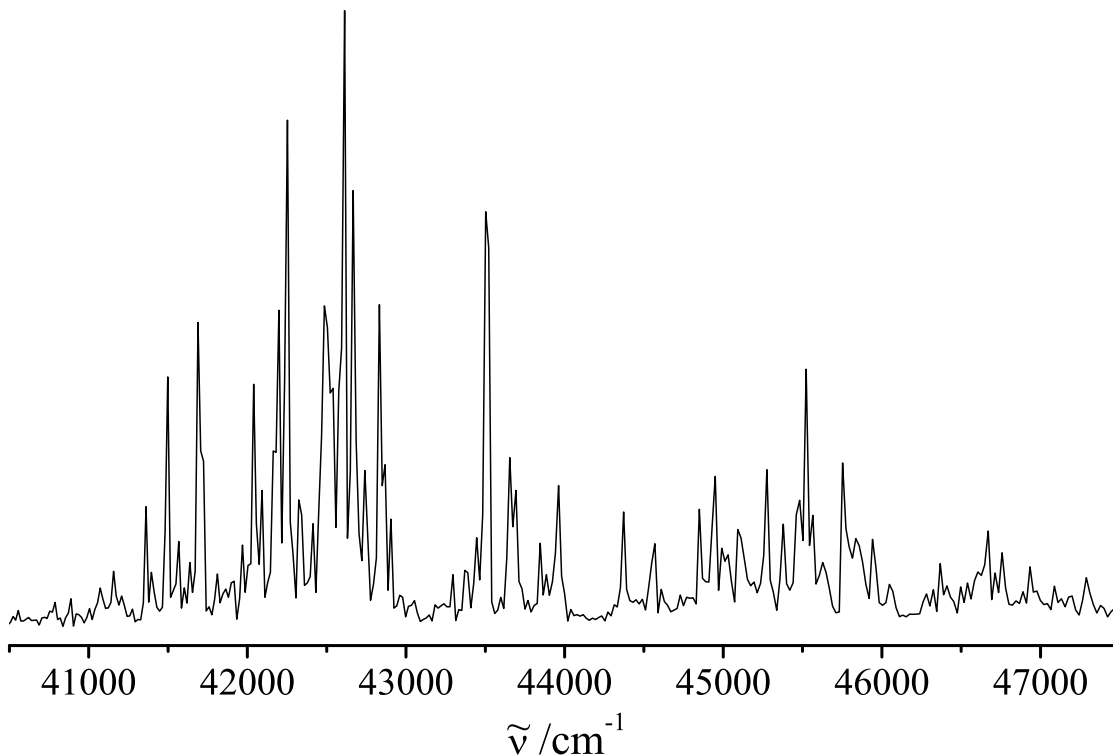
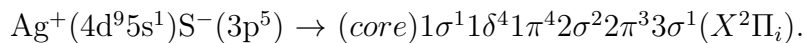


Figure 4.8: Mass-selected [1+1'] resonance enhanced multi-photon ionization spectrum of  $^{107}\text{Ag}^{32}\text{S}$  in the 40 500 - 47 500  $\text{cm}^{-1}$  region.

There is also a possible contribution from an ionic configuration resulting from coupling the open shell  $\text{Ag}^+ 4d^9 5s^1$  electrons with  $\text{S}^- 3p^5$  electrons, as in the case of  $\text{AgO}$  [10],



A study of magnetic hyperfine interactions in the  $X^2\Pi_i$  state would provide a further understanding about the contribution of various electronic configurations to bonding in  $\text{AgS}$ .

## 4.5 Conclusion

AgS has been spectroscopically characterized in the gas phase for the first time, with the band system in the 10 000 – 11 000  $\text{cm}^{-1}$  region assigned to the  $A^2\Sigma^+ - X^2\Pi_i$  electronic transition. The vibrational constants for both electronic states and the spin-orbit coupling parameter for the ground state were determined from the analysis of the spectrum. The two strongest features, assigned to the  $A^2\Sigma^+ - X^2\Pi_{3/2}$  component of the 0–0 and 1–0 transitions, were recorded at rotational resolution and the spectroscopic constants were determined for both electronic states. The spin-orbit coupling constant for the ground state suggests some covalent character for Ag–S bond.

Several electronic systems were also observed in the UV. Band origin and vibronic progressions were identified for seven of these in the 25 000 – 40 000  $\text{cm}^{-1}$  region. High resolution spectra were recorded for two of the electronic systems in 25 500 - 26 500  $\text{cm}^{-1}$  region; detailed analysis for which is currently in progress.

# Bibliography

- [1] C. W. Bauschlicher Jr., H. Partridge, and S. R. Langhoff. An ab initio study of the low-lying doublet states of AgO and AgS. *Chemical Physics*, 148:57–68, 1990.
- [2] X. Sun, J. Wang, and Z. Wu. Chemical bonding and electronic structure of 4d-metal monosulfides. *Journal of Cluster Science*, 20:525–534, 2009.
- [3] M. W. Schmidt, K. K. Baldrige, J. A. Boatz, S. T. Elbert, M. S. Gordon, J. H. Jensen, S. Koseki, N. Matsunaga, K. A. Nguyen, S. Su, T. L. Windus, M. Dupuis, and J. A. Montgomery. General atomic and molecular electronic structure system. *Computational Chemistry*, 14:1347–1363, 1993.
- [4] C. E. Dykstra, G. Frenking, K. S. Kim, and G. E. Scuseria, editors. *Theory and Applications of Computational Chemistry: the first forty years*, chapter by M. S. Gordon and M. W. Schmidt, Advances in electronic structure theory: GAMESS a decade later, pages 1167–1189. Elsevier, Amsterdam, Netherlands, 2005.
- [5] L. C. O’Brien, S. J. Wall, and M. K. Sieber. Fourier transform spectroscopy of the  $A^2\Sigma^+ - X^2\Pi_i$  transition of AgO. *Journal of Molecular Spectroscopy*, 183:57–60, 1997.
- [6] L. C. O’Brien, M. Dulick, and S. P. Davis. The near-infrared  $Y^2\Sigma^+ - X^2\Pi$  transition of CuS. *Journal of Molecular Spectroscopy*, 195:328–331, 1999.
- [7] C. M. Western. PGOPHER, a program for simulating rotational structure. University of Bristol, <http://pgopher.chm.bris.ac.uk>.

- [8] H. Lefebvre-Brion and R. W. Field. *Perturbations in the Spectra of Diatomic Molecules*. Academic Press, Orlando, U. S. A., 1986.
- [9] J. M. Thompsen and L. M. Ziurys. Transition metal sulfide studies: the pure rotational spectrum of the CuS radical ( $X^2\Pi_i$ ). *Chemical Physics Letters*, 344:75–84, 2001.
- [10] T. Steimle, M. Tanimoto, K. Namiki, and S. Saito. The millimeter wave spectrum of silver monoxide, AgO. *Journal of Chemical Physics*, 108:7616–7622, 1998.

## 5 Titanium dioxide

Titanium dioxide can have one of the four isomeric forms; (a) O=Ti=O linear form, (b) inserted form with a large apex angle, (c) T-Shaped form with a small apex angle and an O–O distance close to that of O<sub>2</sub>, and (d) Ti-O-O superoxide form. The first experimental study to identify the structure of TiO<sub>2</sub> was undertaken more than 45 years ago [1]. This gas phase electrostatic deflection measurement on a molecular beam sample of TiO<sub>2</sub> demonstrated that the ground state has a permanent electric dipole, thus ruling out linear O=Ti=O structure. The infrared absorption and visible emission spectra of TiO<sub>2</sub> were first recorded in a neon matrix and C<sub>2v</sub> structure was suggested for both the ground and excited electronic states [2]. The  $\nu_1$  (a<sub>1</sub>) symmetric stretching and  $\nu_3$  (b<sub>2</sub>) asymmetric stretching frequencies for the <sup>48</sup>TiO<sub>2</sub> isotopologue were determined to be  $962.0 \pm 0.2 \text{ cm}^{-1}$  and  $934.8 \pm 0.2 \text{ cm}^{-1}$ , respectively. The isotopic dependence of  $\nu_3$  (b<sub>2</sub>) was used to extract an estimate for the bond angle,  $\theta$ , as  $110 \pm 15^\circ$ . Weak, visible emission having an origin at  $529.5 \pm 0.2 \text{ nm}$  and exhibiting a progression in the  $\nu_1$  (a<sub>1</sub>) symmetric stretch of the  $X^1A_1$  state was observed. The long vibrational progression was attributed to a significant change in geometry upon excitation. Subsequently, infrared absorption spectrum was recorded in an argon matrix and analysed to give  $\nu_1$  (a<sub>1</sub>) and  $\nu_3$  (b<sub>2</sub>) of  $946.9 \text{ cm}^{-1}$  and  $917.1 \text{ cm}^{-1}$ , respectively [3]. Again the isotopic dependence of  $\nu_3$  (b<sub>2</sub>) was used to estimate  $\theta$  as  $113 \pm 5^\circ$ . An investigation of TiO<sub>2</sub><sup>-</sup> by photoelectron spectroscopy (PES) [4] gave values for the  $a^3B_2$  and  $A^1B_2$  states of TiO<sub>2</sub> as  $15\,800 \pm 800 \text{ cm}^{-1}$  and  $19\,350 \pm 1\,600 \text{ cm}^{-1}$ , respectively. The symmetric stretching frequency,  $\nu_1$  (a<sub>1</sub>), of the  $X^1A_1$  state was determined to be  $940 \pm 40 \text{ cm}^{-1}$ , consistent with the matrix isolation value. When the PES spectrum was recorded at a higher resolution [5], the measured  $17\,740 \pm 800 \text{ cm}^{-1}$



difference between the adiabatic detachment energies was interpreted as the splitting between the  $X^1A_1$  and  $a^3B_2$  states. The PES spectrum was assigned assuming that the  $a^3B_2$  state is lower in energy than the isoconfigurational  $A^1B_2$  state. Recently, pure rotational transitions in the (0,0,0)  $X^1A_1$  vibronic state were recorded and the bond length,  $R_{Ti-O} = 165.1$  pm and bond angle,  $\theta = 111.6^\circ$ , determined [6].

There have been numerous theoretical studies on  $TiO_2$  [3, 7–17]. These studies suggest a complex optical spectrum of  $TiO_2$ . According to a recent study using various ab initio and density functional theory (DFT) methods [17], the lowest two singlet excited states are  $A^1B_2$  and  $B^1A_2$ . The vertical excitation energy for these states has been calculated to be 2.367 eV and 3.019 eV, respectively, by equation-of-motion coupled cluster (EOM-CCSD) method. The sequence of the higher excited states differs slightly by the levels of theory. The more reliable EOM-CCSD method predicts  $C^1B_2$  and  $D^1A_1$  states at 3.191 eV and 3.294 eV. The lowest  $a^3B_2$  triplet and  $A^1B_2$  singlet states are predicted to be nearly degenerate and assume a bent oxo-form like the  $X^1A_1$  state, but with a much smaller bond angle ( $95 - 100^\circ$ ) [14, 17]. The  $A^1B_2 - X^1A_1$  electronic transition is expected to have a long vibronic progressions and a very open branch structure. Strong vibronic coupling is also expected because the  $C_{2v}$  structured  $a^3B_2$  triplet and  $A^1B_2$  states are only  $\sim 0.3$  eV more stable than the linear form [14].

The electronic absorption spectrum of neon matrix isolated  $TiO_2$  was recorded in the matrix laboratory of our group [18]. Progressions in two band systems in the visible range were assigned. The origin of first, having a vibrational progression with spacing of  $840\text{ cm}^{-1}$ , was at  $15\,924\text{ cm}^{-1}$ . It was suggested that this system was due to an electronic transition for the linear isomer. The second one exhibited two vibrational progressions, with a spacing of  $850\text{ cm}^{-1}$ , and  $180\text{ cm}^{-1}$ . The origin of this band was difficult to assign because of overlapped  $TiO$  features, but was estimated to be  $19\,084\text{ cm}^{-1}$  and assigned as the  $A^1B_2 - X^1A_1$  transition of the bent oxo form. A third, weak band system with an origin at  $27\,174\text{ cm}^{-1}$  was assigned as the  $C^1B_1 - X^1A_1$  transition of the same isomer. This was followed by gas phase detection of the visible transition of  $TiO_2$  using mass selected resonant

enhanced multi-photon ionization (REMPI) and laser induced fluorescence (LIF) techniques [19]. A strong band at  $18\,655\text{ cm}^{-1}$  observed in the REMPI spectrum was recorded at high-resolution using LIF detection and the rotational structure analyzed. In addition, the optical Stark and dispersed LIF spectra of this band were also measured. It was tentatively assigned as the  $A^1B_2(0,0,0) - X^1A_1(0,0,0)$  transition. The assignment of the lower energy terminus as the  $X^1A_1(0,0,0)$  state is indisputable because of the cold sample conditions, the agreement of the determined spectroscopic parameters with those derived from the analysis of the pure-rotational spectrum and the observation of no features to the blue of the excitation wavelength in the dispersed LIF spectrum. The assignment of  $A^1B_2$  as the excited state is consistent with the most recent wavefunction based [14] and time dependent density functional theory (TD-DFT) based [20] predictions for the excitation energy of 2.33 eV and 2.22 eV, respectively. The assignment was also consistent with the photoelectron [4, 5] and neon matrix [18] spectra. However, it is difficult to explain the observed presence of bands to the red of  $18\,655\text{ cm}^{-1}$  in the REMPI spectrum with its assignment as the  $A^1B_2(0,0,0) - X^1A_1(0,0,0)$  transition. Furthermore, it is expected that the  $A^1B_2(0,0,0) - X^1A_1(0,0,0)$  vibronic transition would be a relatively weak spectral feature due to the observed change in geometry between the ground and excited states [19].

## 5.1 Experimental

The experimental set-up has been described in Chapter 3. To summarise, a molecular beam of  $\text{Ti}^{16}\text{O}_2$  was generated by laser ablation of a titanium rod in the presence of a supersonic expansion of a 95% He/5%  $\text{O}_2$  mixture. The mass selected [1+1'] REMPI spectra of  $\text{Ti}^{18}\text{O}_2$  was obtained using  $^{18}\text{O}_2$ . Low-resolution spectra were recorded using an OPO ( $\Delta\nu = 5\text{ cm}^{-1}$ ) or a pulsed dye laser ( $\Delta\nu = 0.15\text{ cm}^{-1}$ ) for excitation and an  $\text{F}_2$  excimer laser (7.87 eV) as the ionization source.

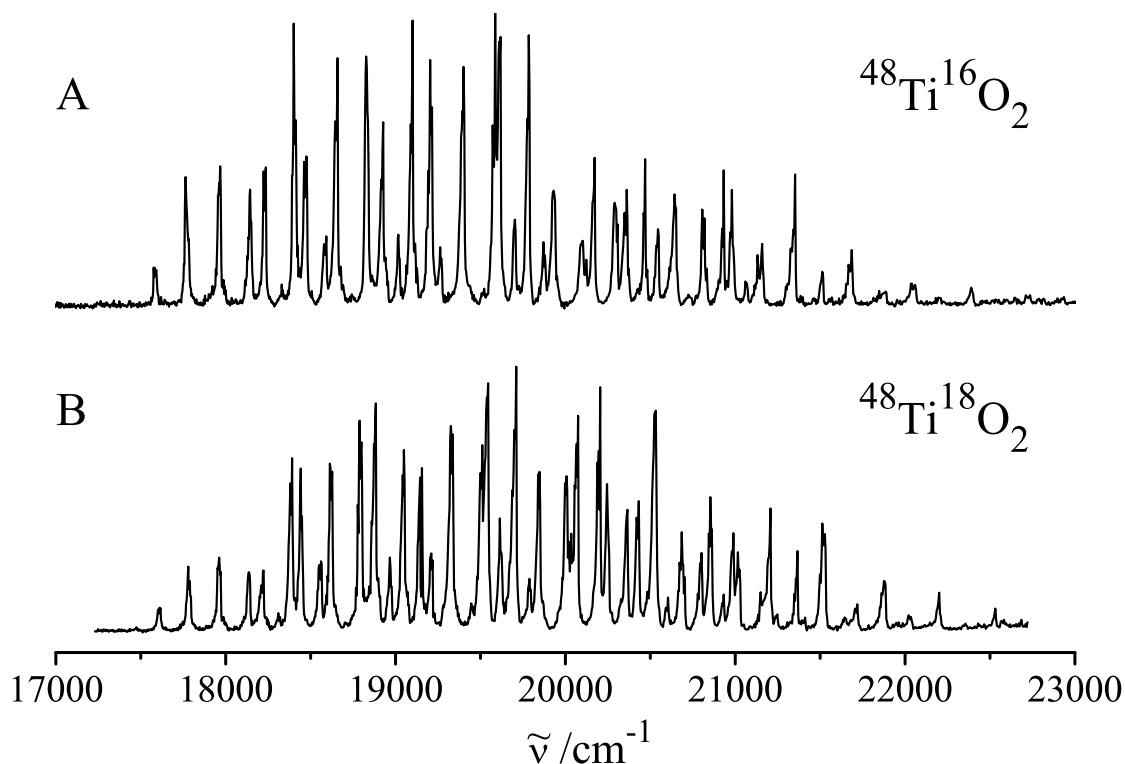


Figure 5.1: Mass-selected  $[1+1']$  resonance enhanced multi-photon ionization spectra of the  $A^1B_2 - X^1A_1$  electronic transition of (A)  $^{48}\text{Ti}^{16}\text{O}_2$ ; (B)  $^{48}\text{Ti}^{18}\text{O}_2$ .

## 5.2 Results and discussion

The mass spectrum of the collimated molecular beam is dominated by Ti and TiO as both have an ionization potential (IP) lower than 7.87 eV. Various other species such as  $(\text{TiO}_2)_2$ ,  $(\text{TiO})_2$ ,  $\text{TiO}(\text{O}_2)$ ,  $\text{TiO}_2(\text{O}_2)$  and  $\text{Ti}_2\text{O}_3$  also appear on the mass spectrum. The  $\text{TiO}_2$  mass signal appears only at resonance. The IP of  $\text{TiO}_2$  is  $9.5 \pm 0.5$  eV [21].

### 5.2.1 Electronic transitions in the visible

The mass-selected  $[1+1']$  REMPI spectra of  $^{48}\text{Ti}^{16}\text{O}_2$  and  $^{48}\text{Ti}^{18}\text{O}_2$  were recorded in the  $14000 \text{ cm}^{-1}$  to  $23000 \text{ cm}^{-1}$  region. There are no features to the red of

17 500  $\text{cm}^{-1}$ . The vibronic spectra between 17 000  $\text{cm}^{-1}$  and 23 000  $\text{cm}^{-1}$  are presented in Figure 5.1.

Isotopic shifts and inertial defects [22] have been used to analyse the spectrum in the 17 500  $\text{cm}^{-1}$  to 20 000  $\text{cm}^{-1}$  region and assign it to progressions in the  $A^1B_2(\nu_1, \nu_2, \nu_3) - X^1A_1(0,0,0)$  transition. The band origin for the  $A^1B_2 - X^1A_1$  transition of  $^{48}\text{Ti}^{16}\text{O}_2$  has been identified at 17 591  $\text{cm}^{-1}$ . The transition wavenumbers and assignments are given in Table 5.1 and the assigned spectrum of  $^{48}\text{Ti}^{16}\text{O}_2$  is shown in Figure 5.2. The vibronic features could not be assigned beyond 20 000  $\text{cm}^{-1}$  due to the complexity of the spectrum.

The observed transition wavenumbers were fit to the phenomenological expression:

$$G(v_1, v_2, v_3) = T_e + \sum_{i=1,3} \omega_i(v_i + \frac{1}{2})$$

using the assigned vibrational quantum numbers. The vibrational parameters for the  $A^1B_2$  state of  $^{48}\text{Ti}^{16}\text{O}_2$  are determined as  $T_{000} = 17\,593(5) \text{ cm}^{-1}$ ,  $\omega_1 = 876(3) \text{ cm}^{-1}$ ,  $\omega_2 = 184(1) \text{ cm}^{-1}$  and  $\omega_3 = 316(2) \text{ cm}^{-1}$ . The energy of the  $A^1B_2$  state is determined to be 18 020  $\text{cm}^{-1}$  by combining the zero point energies for the  $A^1B_2$  and  $X^1A_1$  states with  $T_{000}$ . The optimized vibrational parameters are presented in Table 5.2.

The observed shift in the mass-selected [1+1'] REMPI spectrum of  $^{48}\text{Ti}^{16}\text{O}_2$  relative to that of  $^{48}\text{Ti}^{18}\text{O}_2$  is compared with the predictions in Table 5.1. The agreement between the observed and predicted [22] shifts is good given the harmonic approximation, the fact that the symmetric stretch-bend force constant was constrained to zero and the relatively large measuring uncertainty ( $\sim 5 \text{ cm}^{-1}$ ). As expected, the deviation becomes more pronounced with increasing vibrational excitation, particularly excitation of the  $\nu_2$  bending mode. The barrier to linearity in the  $A^1B_2$  is predicted to be only 0.42 eV [14] suggesting the anharmonic contributions for  $\nu_2$  excitation will be significant, hence the poorer agreement.

The spectrum shows evidence of anharmonic behavior for  $\nu_3$ : the spacing between the  $A^1B_2(0,0,0)$  and  $A^1B_2(0,0,2)$  is 648  $\text{cm}^{-1}$ , whereas the spacing between  $A^1B_2(0,0,2)$  and  $A^1B_2(0,0,4)$  is 691  $\text{cm}^{-1}$ . Also, the determined

Table 5.1: Band maxima and isotopic shifts (in  $\text{cm}^{-1}$ ) for the  $A^1B_2(\nu_1, \nu_2, \nu_3) - X^1A_1(0,0,0)$  electronic transition of  $^{48}\text{Ti}^{16}\text{O}_2$  and  $^{48}\text{Ti}^{18}\text{O}_2$ .

Assignment $\nu_1, \nu_2, \nu_3$	Observed wavenumber		Offset <sup>a</sup>	Isotopic shift <sup>b</sup>	
	$^{48}\text{Ti}^{16}\text{O}_2$	$^{48}\text{Ti}^{18}\text{O}_2$		Observed	Calculated
0,0,0	17 591	17 610	0	19	17
0,1,0	17 776	17 779	185	3	9
0,2,0	17 964	17 961	373	-3	1
0,3,0	18 150	18 137	559	-13	-6
0,0,2	18 239	18 223	648	-16	-9
0,4,0	18 336	18 309	745	-27	-14
0,1,2	18 412	18 390	826	-27	-17
1,0,0	18 470	18 441	874	-24	-19
0,2,2	18 596	18 561	1 005	-35	-24
1,1,0	18 651	18 613	1 060	-38	-27
1,2,0	18 834	18 788	1 243	-46	-35
0,0,4	18 930	18 844	1 339	-46	-35
1,3,0	19 027	18 966	1 436	-61	-43
0,1,4	19 104	19 049	1 513	-55	-42
1,4,0	19 218	19 155	1 627	-63	-50
0,2,4	19 277	19 210	1 686	-67	-50
2,0,0	19 408	19 325	1 817	-83	-55
2,1,0	19 526		1 935		
1,6,0	19 590	19 510	1 999	-80	-61
0,0,6	19 617	19 544	2 026	-73	-60
2,2,0	19 706	19 613	2 115	-93	-71
0,1,6	19 792	19 710	2 201	-82	-68
2,3,0	19 883	19 788	2 292	-95	-79
	19 942	19 847	2 351	-95	
	20 107	20 006	2 516	-101	
3,0,0	20 176	20 074	2 585	-102	-91
0,0,8	20 307	20 204	2 716	-103	-86
3,1,0	20 369	20 245	2 778	-124	-99

<sup>a</sup> Shift from the 17 591  $\text{cm}^{-1}$  band.<sup>b</sup>  $\tilde{\nu}^{48}\text{Ti}^{18}\text{O}_2 - \tilde{\nu}^{48}\text{Ti}^{16}\text{O}_2$ .

$\omega_3(A^1B_2)$  value ( $= 316(2) \text{ cm}^{-1}$ ) is significantly smaller than MRCI predicted one

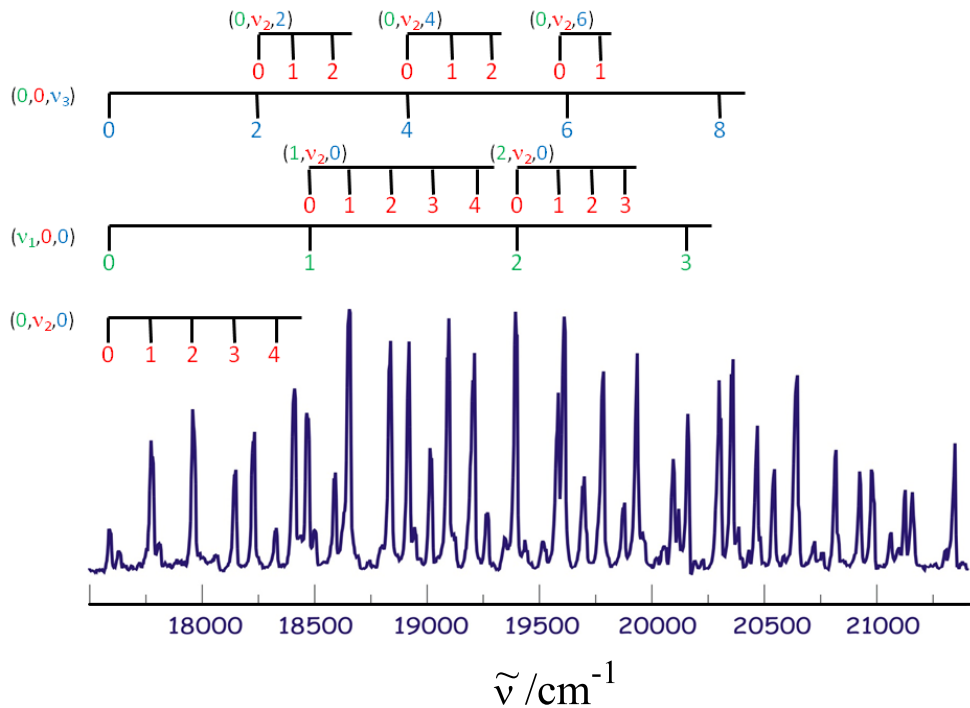


Figure 5.2: Assignment for the  $A^1B_2(v_1, v_2, v_3) - X^1A_1(0, 0, 0)$  electronic transition of  $^{48}\text{Ti}^{16}\text{O}_2$ .

Table 5.2: Vibrational parameters (in  $\text{cm}^{-1}$ ) for the  $A^1B_2$  state of  $^{48}\text{Ti}^{16}\text{O}_2$ .

Parameter	Value
$T_{000}$	17 593(5)
$\omega_1$	876(3)
$\omega_2$	184(1)
$\omega_3$	316(2)

(= 480  $\text{cm}^{-1}$ ) [14]. This suggests that the asymmetric  $\nu_3$  mode of the  $A^1B_2$  state interacts with other vibronic states, as discussed in Ref. 22.

Based on the [1+1'] REMPI spectrum of  $^{48}\text{Ti}^{16}\text{O}_2$ , high resolution LIF spectra ( $0.001 \text{ cm}^{-1}$ ) were recorded for the  $A^1B_2(1,1,0) - X^1A_1(0,0,0)$  ( $\nu = 18\,655 \text{ cm}^{-1}$ ),  $A^1B_2(0,0,2) - X^1A_1(0,0,0)$  ( $\nu = 18\,240 \text{ cm}^{-1}$ ),  $A^1B_2(0,1,2) - X^1A_1(0,0,0)$

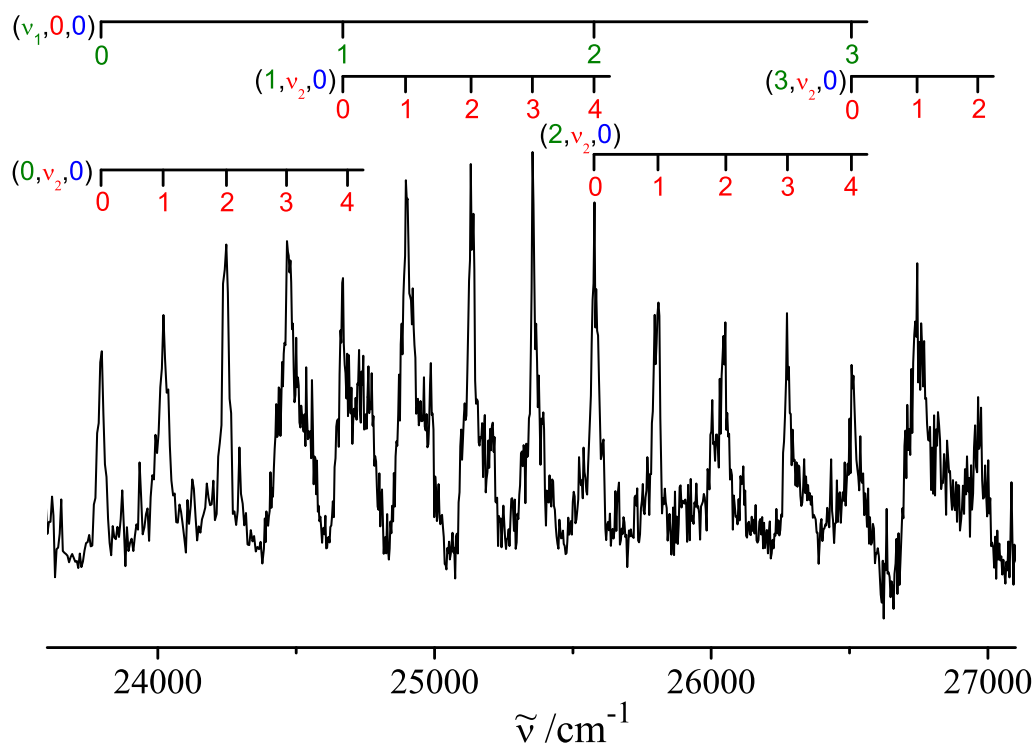


Figure 5.3: Mass-selected  $[1+1']$  resonance enhanced multi-photon ionization spectrum of the  $C^1B_2(\nu_1, \nu_2, \nu_3) - X^1A_1(0, 0, 0)$  electronic transition of  $^{48}\text{Ti}^{16}\text{O}_2$ .

( $\nu = 18412 \text{ cm}^{-1}$ ) and  $A^1B_2(1, 0, 0) - X^1A_1(0, 0, 0)$  ( $\nu = 18470 \text{ cm}^{-1}$ ) vibronic transitions [22]. The analysis of these bands shows a significant geometry change from the ground to the excited state, as predicted by calculations [14].

A comparison with the previous PES [4, 5] and the matrix isolation measurement [18] is also warranted. The band system with an origin at  $15924 \text{ cm}^{-1}$  observed in the absorption spectrum of a neon matrix isolated sample was not detected in the gas-phase sample studied here. This is consistent with the assumption [18] that the carrier of that band is the higher energy linear isomer and hence is not expected to be present in the laser ablation products. The observed  $A^1B_2(0, 0, 0) - X^1A_1(0, 0, 0)$  ( $\nu = 17591 \text{ cm}^{-1}$ ) band is shifted to the red by nearly  $1500 \text{ cm}^{-1}$  compared to the  $19084 \text{ cm}^{-1}$  origin assigned in the neon matrix isolation study [18]. This unrealistically large matrix-gas shift suggests that the first

Table 5.3: Band maxima (in  $\text{cm}^{-1}$ ) for the  $C^1B_2(\nu_1, \nu_2, \nu_3) - X^1A_1(0,0,0)$  electronic transition of  $^{48}\text{Ti}^{16}\text{O}_2$ .

Assignment $\nu_1, \nu_2, \nu_3$	Observed wavenumber	Offset <sup>a</sup>	Assignment $\nu_1, \nu_2, \nu_3$	Observed wavenumber	Offset <sup>a</sup>
0,0,0	23 797	0	1,3,0	25 354	1 557
0,1,0	24 020	223	1,4,0	25 578	1 781
0,2,0	24 247	450	2,0,0	25 578	1 781
0,3,0	24 466	669	2,1,0	25 809	2 012
	24 535	738		26 004	2 207
1,0,0	24 669	872	2,2,0	26 051	2 254
0,4,0	24 684	887	2,3,0	26 273	2 476
	24 760	963	2,4,0	26 507	2 710
1,1,0	24 896	1 099	3,0,0	26 507	2 710
	24 987	1 190	3,1,0	26 745	2 948
1,2,0	25 131	1 334	3,2,0	26 964	3 167
	25 210	1 413			

<sup>a</sup> Shift from the  $23\,797\text{ cm}^{-1}$  band.

features of the progression observed in the neon matrix spectrum were too weak to be observed. The separation of the first two peaks in the PES spectrum [4] is  $17\,740 \pm 800\text{ cm}^{-1}$ , in line with the  $A^1B_2(0,0,0) - X^1A_1(0,0,0)$  ( $\nu = 17\,591\text{ cm}^{-1}$ ) gas-phase value. The REMPI spectrum exhibits long progressions due to a significant change in geometry. In contrast, the two lowest spectral features in the PES spectrum are relatively narrow (FWHM  $\approx 0.4\text{ eV}$ ).

### 5.2.2 Electronic transitions in the ultraviolet

The mass-selected  $[1+1']$  REMPI spectrum of  $^{48}\text{Ti}^{16}\text{O}_2$ , recorded in the  $23\,500\text{ cm}^{-1}$  to  $27\,000\text{ cm}^{-1}$  region, is presented in Figure 5.3. The observed bands are tentatively assigned to  $C^1B_2 - X^1A_1$  transition based on EOM-CCSD calculations [17] and the origin identified at  $23\,797\text{ cm}^{-1}$ . A progression with a frequency of  $\sim 870\text{ cm}^{-1}$  is assigned to the  $\nu_1$  symmetric stretch mode and another one with a frequency of  $\sim 225\text{ cm}^{-1}$  is assigned to the  $\nu_2$  bend mode. There are some



unassigned features in the spectrum; the asymmetric stretch mode,  $\nu_3$ , might be responsible for these. Strong vibronic coupling is expected in the spectrum as EOM-CCSD calculations [17] predict  $D^1A_1$ ,  $E^1B_1$  and  $F^1B_1$  electronic states to lie within 0.5 eV of the  $C^1B_2$  state. The transition wavenumbers and assignments are given in Table 5.3.

### 5.3 Conclusion

Electronic spectra of  $\text{TiO}_2$  have been recorded in the visible and UV regions. The origin for the  $A^1B_2 - X^1A_1$  transition has been identified at  $17\,593\text{ cm}^{-1}$  whereas the band system with origin at  $23\,797\text{ cm}^{-1}$  has been tentatively assigned to the  $C^1B_2 - X^1A_1$  transition. The vibrational frequencies for the  $A^1B_2$  state of  $\text{Ti}^{16}\text{O}_2$  have been determined as  $\omega_1 = 876(3)\text{ cm}^{-1}$ ,  $\omega_2 = 184(1)\text{ cm}^{-1}$  and  $\omega_3 = 316(2)\text{ cm}^{-1}$ . Both electronic systems show a long progression, suggesting a significant change in geometry between the ground and excited states, which was confirmed in the case of  $A^1B_2 - X^1A_1$  transition by high-resolution LIF spectroscopy ( $0.001\text{ cm}^{-1}$ ) [22].

# Bibliography

- [1] M. Kaufman, J. Muentner, and W. Klemperer. Geometry of some refractory metal dioxides. *Journal of Chemical Physics*, 47:3365–3366, 1967.
- [2] N. S. McIntyre, K. R. Thompson, and W. Weltner Jr. Spectroscopy of titanium oxide and titanium dioxide molecules in inert matrices at 4°K. *Journal of Physical Chemistry*, 75:3243–3249, 1971.
- [3] G. V. Chertihin and L. Andrews. Reactions of laser ablated titanium, zirconium, and hafnium atoms with oxygen molecules in condensing argon. *Journal of Physical Chemistry*, 99:6356–6366, 1995.
- [4] H. Wu and L.-S. Wang. Electronic structure of titanium oxide clusters:  $\text{TiO}_y$  ( $y = 1 - 3$ ) and  $(\text{TiO}_2)_n$  ( $n = 1 - 4$ ). *Journal of Chemical Physics*, 107:8221–8228, 1997.
- [5] H.-J. Zhai and L.-S. Wang. Probing the electronic structure and band gap evolution of titanium oxide clusters  $(\text{TiO}_2)_n^-$  ( $n = 1 - 10$ ) using photoelectron spectroscopy. *Journal of the American Chemical Society*, 129:3022–3026, 2007.
- [6] S. Brünken, H. S. P. Müller, K. M. Menten, M. C. McCarthy, and P. Thaddeus. The rotational spectrum of  $\text{TiO}_2$ . *Astrophysical Journal*, 676:1367–1371, 2008.
- [7] M. V. Ramana and D. H. Phillips. A computational study of the  $\text{TiO}_2$  molecule. *Journal of Chemical Physics*, 88:2637–2640, 1988.

- [8] A. Hagfeldt, R. Bergstroem, H. O. G. Siegbahn, and S. Lunell. Structure and stability of small titanium/oxygen clusters studied by ab initio quantum chemical calculations. *Journal of Physical Chemistry*, 97:12725–12730, 1993.
- [9] M. B. Walsh, R. A. King, and H. F. Schaefer. The structures, electron affinities, and energetic stabilities of  $\text{TiO}_n$  and  $\text{TiO}_n^-$  ( $n = 1-13$ ). *Journal of Chemical Physics*, 110:5224–5230, 1999.
- [10] K. S. Jeong, C. Chang, E. Sedlmayr, and D. Sülzle. Electronic structure investigation of neutral titanium oxide molecules  $\text{Ti}_x\text{O}_y$ . *Journal of Physics B: Atomic, Molecular and Optical Physics*, 33:3417–3430, 2000.
- [11] T. Albaret, F. Finocchi, and C. Noguera. Density functional study of stoichiometric and O-rich titanium oxygen clusters. *Journal of Chemical Physics*, 113:2238–2249, 2000.
- [12] G. L. Gutsev, B. K. Rao, and P. Jena. Systematic study of oxo, peroxy, and superoxy isomers of 3d-metal dioxides and their anions. *Journal of Physical Chemistry A*, 104:11961–11971, 2000.
- [13] Z. W. Qu and G. J. Kroes. Theoretical study of the electronic structure and stability of titanium dioxide clusters  $(\text{TiO}_2)_n$  with  $n = 1 - 9$ . *Journal of Physical Chemistry B*, 110:8998–9007, 2006.
- [14] F. Grein. Density functional theory and multireference configuration interaction studies on low-lying excited states of  $\text{TiO}_2$ . *Journal of Chemical Physics*, 126:34313:1–8, 2007.
- [15] S. Li and D. A. Dixon. Molecular structures and energetics of the  $(\text{TiO}_2)_n$  ( $n = 1 - 4$ ) clusters and their anions. *Journal of Physical Chemistry A*, 112:6646–6666, 2008.
- [16] D. J. Taylor and M. J. Paterson. Calculations of the low-lying excited states of the  $\text{TiO}_2$  molecule. *Journal of Chemical Physics*, 133:204302:1–4, 2010.

- 
- [17] C. K. Lin, J. Li, Z. Tu, X. Li, M. Hayashi, and S. H. Lin. A theoretical search for stable bent and linear structures of low-lying electronic states of the titanium dioxide ( $\text{TiO}_2$ ) molecule. *RSC Advances*, 1:1228–1236, 2011.
- [18] I. Garkusha, A. Nagy, Z. Guennoun, and J. P. Maier. Electronic absorption spectrum of titanium dioxide in neon matrices. *Chemical Physics*, 353:115–118, 2008.
- [19] H. Wang, T. C. Steimle, C. Apetrei, and J. P. Maier. Characterization of the  $\tilde{X}^1A_1$  and  $\tilde{A}^1B_2$  electronic states of titanium dioxide,  $\text{TiO}_2$ . *Physical Chemistry Chemical Physics*, 11:2649–2656, 2009.
- [20] Y. Liu, Y. Yuan, Z. Wang, K. Deng, C. Xiao, and Q. Li. Assignment of photoelectron spectra of  $(\text{TiO}_2)_n$  with  $n = 1-3$ . *Journal of Chemical Physics*, 130:174308:1–6, 2009.
- [21] G. Balducci, G. Gigli, and M. Guido. Identification and stability determinations for the gaseous titanium oxide molecules  $\text{Ti}_2\text{O}_3$  and  $\text{Ti}_2\text{O}_4$ . *Journal of Chemical Physics*, 83:1913–1916, 1985.
- [22] X. Zhuang, A. Le, T. C. Steimle, R. Nagarajan, V. Gupta, and J. P. Maier. Visible spectrum of titanium dioxide. *Physical Chemistry Chemical Physics*, 12:15018–15028, 2010.



## 6 Zirconium dioxide

Studies on zirconium dioxide are fewer compared to isovalent titanium dioxide. Like  $\text{TiO}_2$ ,  $\text{ZrO}_2$  can have four isomeric forms and again the linear  $\text{O}=\text{Zr}=\text{O}$  structure has been ruled out by an earlier gas phase electrostatic deflection experiment on a molecular beam sample of  $\text{ZrO}_2$  [1], which demonstrated that the ground state has a permanent electric dipole. The infrared absorption spectra of  $\text{ZrO}_2$  was recorded in argon matrix [2], and inserted  $C_{2v}$  structure was suggested for the ground state. The  $\nu_1(a_1)$  symmetric stretch and the  $\nu_3(b_2)$  antisymmetric stretch frequencies were inferred as  $884.3\text{ cm}^{-1}$  and  $818.0\text{ cm}^{-1}$ , respectively. The isotopic dependence of  $\nu_3$  was used to extract an estimate for the bond angle,  $\theta$ , of  $113 \pm 5^\circ$ . The pure rotational transitions of  $\text{ZrO}_2$  were recorded and analysed [3] to obtain the bond length,  $R_{\text{Zr-O}}$  and bond angle,  $\theta$  as  $177.1\text{ pm}$ , and  $108.11^\circ$ , respectively. In the same study, inertial defect was used to determine the frequency of the bending mode,  $\nu_2(a_1)$  as  $290\text{ cm}^{-1}$ . An investigation of  $\text{ZrO}_2^-$  by photoelectron spectroscopy (PES) [4] gave the symmetric stretching frequency,  $\omega_1$  as  $887 \pm 40\text{ cm}^{-1}$  for the ground state. These PES results were supported by ab initio calculations using a coupled cluster method with single, double, and non-iterative triple excitations (CCSD(T)), which predicted the harmonic vibrational frequencies,  $\omega_1$ ,  $\omega_2$  and  $\omega_3$  for the  $X^1A_1$  ground state as  $887\text{ cm}^{-1}$ ,  $281\text{ cm}^{-1}$ , and  $835\text{ cm}^{-1}$ , respectively. In a separate study, high level ab initio calculations were done to model the  $355\text{ nm}$  photodetachment spectrum [5]. A study using the CCSD(T) theory predicted the stretching frequencies  $\omega_1$  and  $\omega_3$  as  $924\text{ cm}^{-1}$  and  $860\text{ cm}^{-1}$  [6]. The calculations at equation-of-motion coupled cluster (EOM-CCSD) level gave a separation of  $2.14\text{ eV}$  between the  $X^1A_1$  ground state and  $a^3B_2$  lowest energy triplet state [6]. In a recent study, using time-dependent den-

sity functional theory (TD-DFT) with B3LYP function, the vertical excitation energy for the lowest two singlet excited states  $A^1B_2$  and  $B^1A_1$  have been calculated as 2.1 eV and 2.9 eV, respectively [7, 8]. Using the same method, the harmonic vibrational frequencies,  $\omega_1$ ,  $\omega_2$  and  $\omega_3$  for the  $A^1B_2$  excited state have been predicted as  $855\text{ cm}^{-1}$ ,  $151\text{ cm}^{-1}$ , and  $420\text{ cm}^{-1}$ , respectively [7]. For the  $B^1A_1$  excited state, the symmetric stretching frequency,  $\omega_1$  has been calculated as  $831\text{ cm}^{-1}$  and the symmetric bending frequency,  $\omega_2$  as  $245\text{ cm}^{-1}$  [8].

## 6.1 Experimental

The experimental set-up and conditions were similar to that of  $\text{TiO}_2$ , the only difference being use of zirconium rod instead of titanium. The details are present in Chapters 3 and 5. The ionization potential of  $\text{ZrO}_2$  is  $9.4 \pm 0.2\text{ eV}$ .

## 6.2 Results and discussion

### 6.2.1 Electronic transitions in the visible

The mass-selected  $[1+1']$  resonance enhanced multiphoton ionization (REMPI) spectra of  $^{90}\text{Zr}^{16}\text{O}_2$  in the  $17\,000\text{ cm}^{-1}$  to  $21\,000\text{ cm}^{-1}$  region is presented in Figure 6.1. Based upon the analogy with  $\text{TiO}_2$  and ab initio prediction [7], the spectrum in Figure 6.1 is assigned to progressions in the  $A^1B_2(\nu_1, \nu_2, \nu_3) - X^1A_1(0,0,0)$  transition. There are no features to the red of the band at  $17\,041\text{ cm}^{-1}$ , so it was assigned as the origin of the to the  $A^1B_2 - X^1A_1$  electronic transition, assuming adiabatic expansion conditions where only the  $X^1A_1(0,0,0)$  level is populated. The transition wavenumbers and assignments are given in Table 6.1.

The observed transition wavenumbers were fit to the phenomenological expression:

$$G(v_1, v_2, v_3) = T_e + \sum_{i=1,3} \omega_i(v_i + \frac{1}{2}) + \sum_{i=1,3} \sum_{k=1,3} \chi_{ik}(v_i + \frac{1}{2})(v_k + \frac{1}{2})$$

Table 6.1: Band maxima (in  $\text{cm}^{-1}$ ) for the  $A^1B_2(\nu_1, \nu_2, \nu_3) - X^1A_1(0,0,0)$  electronic transition of  $^{90}\text{Zr}^{16}\text{O}_2$ .

Assignment $\nu_1, \nu_2, \nu_3$	Observed wavenumber	Offset <sup>a</sup>	Assignment $\nu_1, \nu_2, \nu_3$	Observed wavenumber	Offset <sup>a</sup>
0,0,0	17 041	0	2,2,0	19 020	1 979
0,1,0	17 194	153	0,1,4	19 148	2 107
0,2,0	17 351	310	2,3,0	19 173	2 132
0,3,0	17 506	465	0,2,4	19 310	2 269
0,0,1	17 562	521	0,0,5	19 404	2 363
0,4,0	17 663	622	3,0,0	19 484	2 443
0,1,1	17 723	682	0,1,5	19 575	2 534
1,0,0	17 873	832	3,1,0	19 660	2 619
0,2,1	17 888	847		19 691	2 650
0,0,2	18 026	985	0,2,5	19 738	2 697
1,1,0	18 026	985	3,2,0	19 816	2 775
1,2,0	18 181	1 140		19 851	2 810
0,1,2	18 193	1 152	0,3,5	19 907	2 866
1,3,0	18 336	1 295	3,3,0	19 982	2 941
0,2,2	18 357	1 316	0,4,5	20 107	3 066
0,0,3	18 476	1 435	3,4,0	20 147	3 106
0,3,2	18 518	1 477	0,5,5	20 274	3 233
0,1,3	18 643	1 602	4,0,0	20 323	3 282
2,0,0	18 706	1 655	4,1,0	20 494	3 453
0,2,3	18 806	1 755	4,2,0	20 663	3 622
2,1,0	18 863	1 822	4,3,0	20 819	3 778
0,0,4	18 998	1 957			

<sup>a</sup> Shift from the 17 041  $\text{cm}^{-1}$  band.

using the assigned vibrational quantum numbers. The features which were measured with  $0.1 \text{ cm}^{-1}$  dye laser using laser induced fluorescence (LIF) [7] were assigned a weight three times that of the features recorded with low resolution [1+1'] REMPI. Various combinations of the anharmonic terms  $\chi_{ik}$  were attempted. Ultimately, a fit of the excitation spectra was obtained by varying only  $\chi_{12}$ ,  $\chi_{23}$ , and  $\chi_{33}$  in addition to  $\omega_1$ ,  $\omega_2$ , and  $\omega_3$  for the  $A^1B_2$  state. The vibrational parameters for the  $A^1B_2$  state of  $^{90}\text{Zr}^{16}\text{O}_2$  are determined to be  $T_{000} = 17,050(13) \text{ cm}^{-1}$ ,  $\omega_1 = 819(3) \text{ cm}^{-1}$ ,  $\omega_2 = 149(3) \text{ cm}^{-1}$ ,  $\omega_3 = 518(4) \text{ cm}^{-1}$ ,



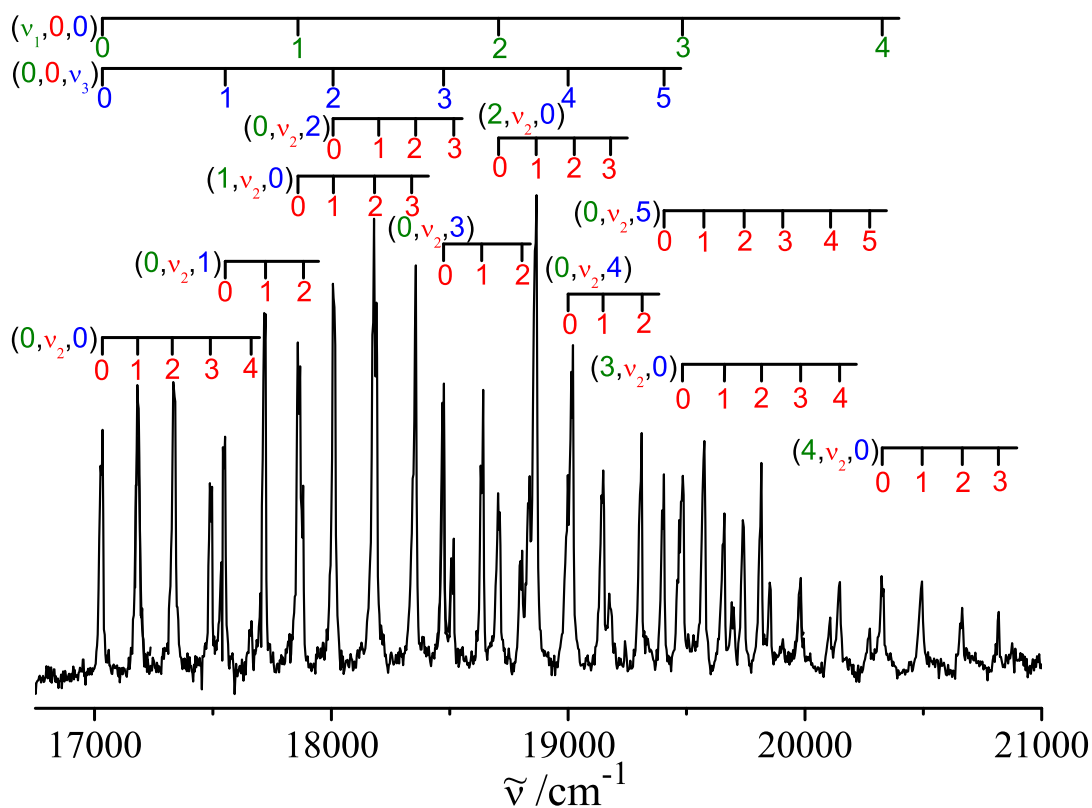


Figure 6.1: Mass-selected  $[1+1']$  resonance enhanced multi-photon ionization spectrum of the  $A^1B_2 - X^1A_1$  electronic transition of  $^{90}\text{Zr}^{16}\text{O}_2$ .

Table 6.2: Vibrational parameters (in  $\text{cm}^{-1}$ ) for the  $A^1B_2$  state of  $^{90}\text{Zr}^{16}\text{O}_2$ .

Parameter	Value
$T_{000}$	17 050(13)
$\omega_1$	819(3)
$\omega_2$	149(3)
$\omega_3$	518(4)
$\chi_{12}$	2(1)
$\chi_{23}$	4.4(8)
$\chi_{33}$	-8.5(8)

$\chi_{12} = 2(1) \text{ cm}^{-1}$ ,  $\chi_{23} = 4.4(8) \text{ cm}^{-1}$ , and  $\chi_{33} = -8.5(8) \text{ cm}^{-1}$ . The energy of the  $A^1B_2$  state is determined to be  $16\,304(16) \text{ cm}^{-1}$  by combining the zero point

energies for the  $A^1B_2$  and  $X^1A_1$  states with  $T_{000}$ . The optimized vibrational parameters are presented in Table 6.2.

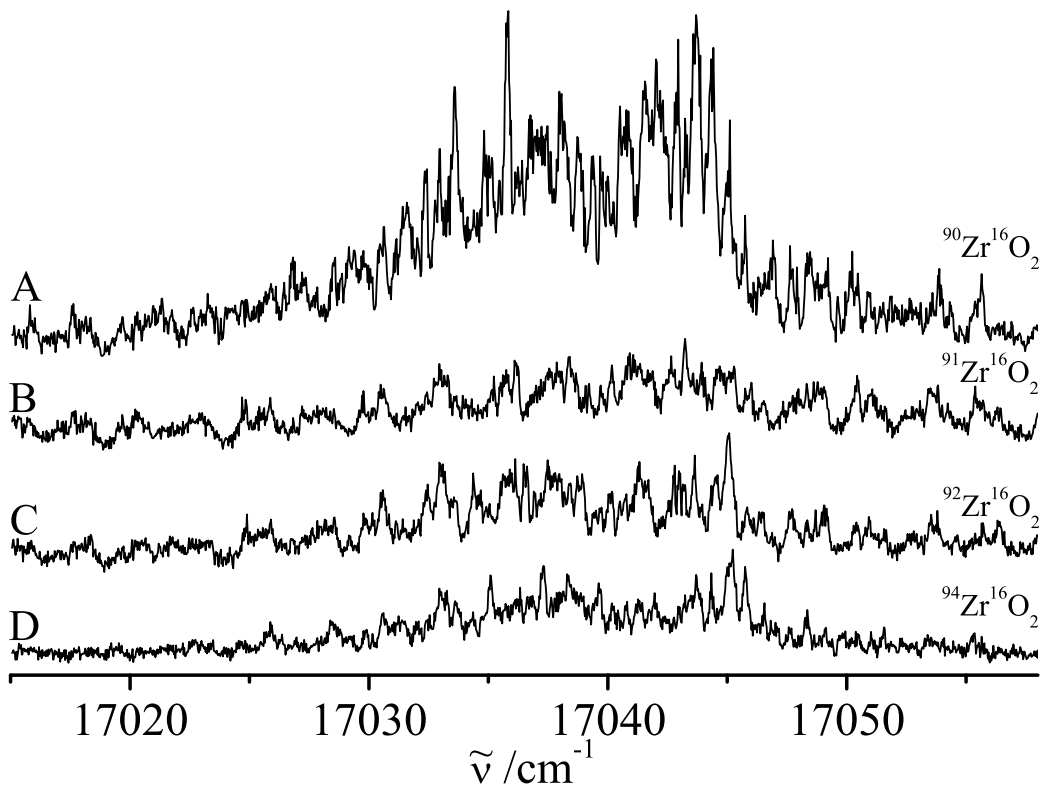


Figure 6.2: The rotational contours for the  $A^1B_2(0,0,0) - X^1A_1(0,0,0)$  transition of (A)  $^{90}\text{Zr}^{16}\text{O}_2$ ; (B)  $^{91}\text{Zr}^{16}\text{O}_2$ ; (C)  $^{92}\text{Zr}^{16}\text{O}_2$ ; (D)  $^{94}\text{Zr}^{16}\text{O}_2$ .

The  $A^1B_2 - X^1A_1$  vibronic spectrum of  $\text{TiO}_2$  and  $\text{ZrO}_2$  look very similar. However, there is one significant difference: the observation of odd  $\nu_3$  quanta transitions in the case of  $\text{ZrO}_2$ . This provides an evidence of vibronic coupling between the  $A^1B_2$  and  $B^1A_1$  electronic states, which is discussed in Ref. 7.

The rotational contours of seven different bands were recorded by [1+1'] REMPI with a dual-grating dye laser ( $\Delta\nu = 0.06 \text{ cm}^{-1}$ ) but the rotational lines could not be resolved. Based on these measurements, high resolution ( $0.001 \text{ cm}^{-1}$ ) spectrum of the origin band was recorded at Arizona State University using LIF [9]. However, the rotational lines could not be assigned due to overlap from

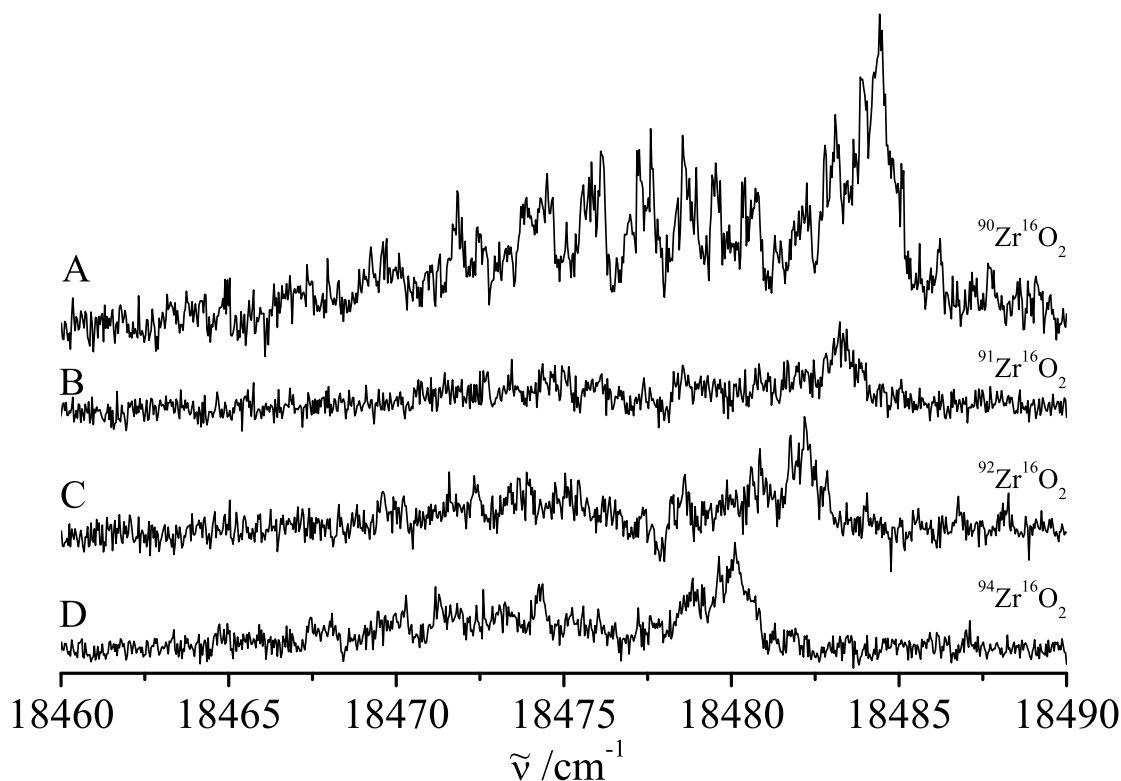


Figure 6.3: The rotational contours for the  $A^1B_2(0,0,3) - X^1A_1(0,0,0)$  transition of (A)  $^{90}\text{Zr}^{16}\text{O}_2$ ; (B)  $^{91}\text{Zr}^{16}\text{O}_2$ ; (C)  $^{92}\text{Zr}^{16}\text{O}_2$ ; (D)  $^{94}\text{Zr}^{16}\text{O}_2$ .

five  $\text{ZrO}_2$  isotopologues ( $^{90}\text{Zr}$ (51.5%),  $^{91}\text{Zr}$ (11.2%),  $^{92}\text{Zr}$ (17.2%),  $^{94}\text{Zr}$ (17.4%), and  $^{96}\text{Zr}$ (2.8%)). The rotational contours for the  $A^1B_2(0,0,0) - X^1A_1(0,0,0)$  and  $A^1B_2(0,0,3) - X^1A_1(0,0,0)$  transition of the four most abundant isotopologues of  $\text{ZrO}_2$  are presented in Figure 6.2 and Figure 6.3, respectively. In the case of  $A^1B_2(0,0,3) - X^1A_1(0,0,0)$  transition, a significant isotopic shift can be observed.

### 6.2.2 Electronic transitions in the ultraviolet

The mass-selected  $[1+1']$  REMPI spectrum of  $^{90}\text{Zr}^{16}\text{O}_2$ , recorded in the  $23\,000\text{ cm}^{-1}$  to  $35\,000\text{ cm}^{-1}$  region, is presented in Figure 6.4. Based on ab initio predictions [7, 8], the band at  $23\,550\text{ cm}^{-1}$  is assigned to the  $B^1A_1(0,0,0) - X^1A_1(0,0,0)$  transition. Analysis of the spectrum in the lower en-

ergy region leads to identification of three distinct progressions with spacing  $\sim 835$   $\text{cm}^{-1}$ ,  $215$   $\text{cm}^{-1}$  and  $545$   $\text{cm}^{-1}$ . These are assigned to the symmetric stretch ( $\nu_1$ ), symmetric bend ( $\nu_2$ ) and asymmetric stretch ( $\nu_3$ ) modes, respectively. The assigned spectrum of  $^{90}\text{Zr}^{16}\text{O}_2$  in the  $23\,000$   $\text{cm}^{-1}$  to  $30\,000$   $\text{cm}^{-1}$  region is shown in Figure 6.5. Many vibronic features could not be assigned due to the complexity of the spectrum. The unassigned features might arise from the transitions between the  $X^1A_1$  ground state and the next higher excited states or as a result of vibronic coupling between electronic states. The transition wavenumbers and assignments for the observed features are given in Table 6.3.

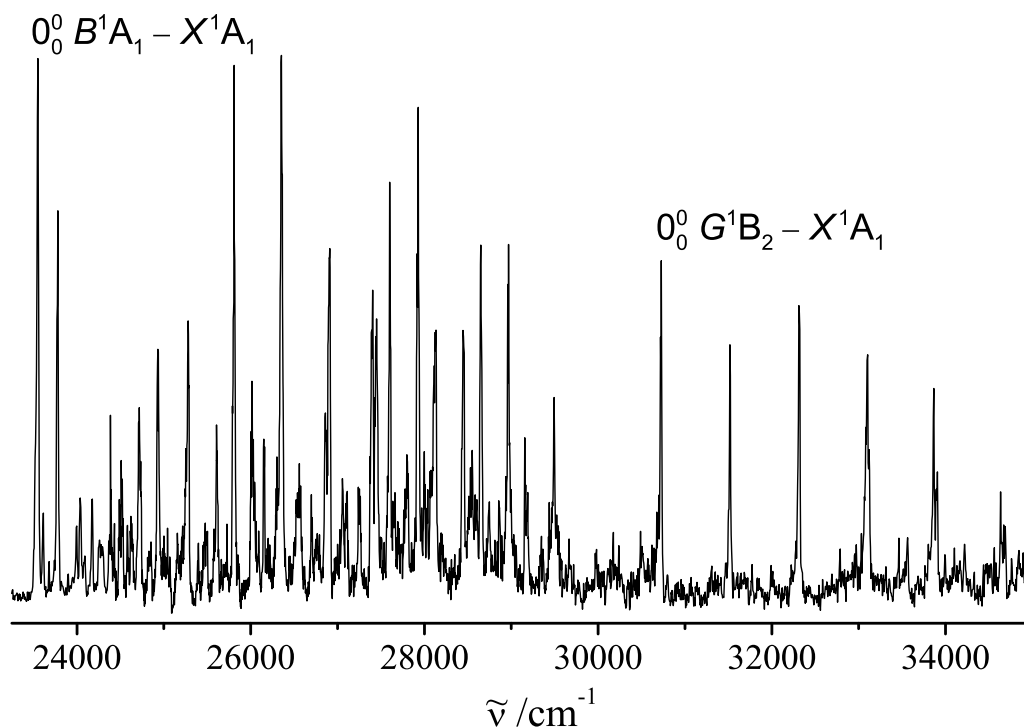


Figure 6.4: Mass-selected  $[1+1']$  resonance enhanced multi-photon ionization spectrum of  $^{90}\text{Zr}^{16}\text{O}_2$  in the  $23\,000$   $\text{cm}^{-1}$  to  $35\,000$   $\text{cm}^{-1}$  region.

The bands observed in the  $30\,000$   $\text{cm}^{-1}$  to  $35\,000$   $\text{cm}^{-1}$  region are tentatively assigned to  $G^1B_2 - X^1A_1$  transition based on ab initio calculations [8], with  $0_0^0$  at  $30\,727$   $\text{cm}^{-1}$ . A progression with a spacing  $\sim 790$   $\text{cm}^{-1}$  can be observed

Table 6.3: Band maxima (in  $\text{cm}^{-1}$ ) for the  $B^1A_1(\nu_1, \nu_2, \nu_3) - X^1A_1(0,0,0)$  electronic transition of  $^{90}\text{Zr}^{16}\text{O}_2$ .

Assignment $\nu_1, \nu_2, \nu_3$	Observed wavenumber	Offset <sup>a</sup>	Assignment $\nu_1, \nu_2, \nu_3$	Observed wavenumber	Offset <sup>a</sup>
0,0,0	23 550	0		26 301	2 751
	23 612 <sup>b</sup>	62	0,0,5	26 353	2 803
	23 679 <sup>c</sup>	129	0,1,5	26 560	3 010
0,1,0	23 780	230	1,0,4	26 698	3 148
0,2,0	23 997	447		26 860	3 310
	24 037	487	0,0,6	26 910	3 360
0,0,1	24 090	540		27 056	3 506
	24 171	621	0,1,6	27 111	3 561
0,1,1	24 300	750	1,0,5	27 240	3 690
1,0,0	24 386	836		27 404	3 854
	24 509	959	0,0,7	27 450	3 900
	24 581	1 031		27 601	4 051
	24 630	1 080	0,1,7	27 662	4 112
0,0,2	24 718	1 168	1,0,6	27 797	4 247
	24 853	1 303		27 929	4 379
0,1,2	24 931	1 381	0,0,8	27 995	4 445
1,0,1	25 002	1 452		28 133	4 583
	25 156	1 606	0,1,8	28 205	4 655
2,0,0	25 217	1 667		28 445	4 895
0,0,3	25 280	1 730		28 551	5 001
	25 399	1 849		28 604	5 054
0,1,3	25 493	1 943		28 649	5 099
1,0,2	25 607	2 057		28 748	5 198
	25 726	2 176		28 816	5 266
0,0,4	25 809	2 259		28 969	5 419
0,1,4	26 014	2 464		29 155	5 605
3,0,0	26 092	2 542		29 494	5 944
1,0,3	26 150	2 600		29 665	6 115

<sup>a</sup> Shift from the 23 550  $\text{cm}^{-1}$  band.

<sup>b</sup>  $B^1A_1(0,1,0) - X^1A_1(0,1,0)$

<sup>c</sup>  $B^1A_1(0,2,0) - X^1A_1(0,2,0)$

(Figure 6.6) and is assigned to the  $\nu_1$  symmetric stretch mode. The transition wavenumbers and assignments are given in Table 6.4.

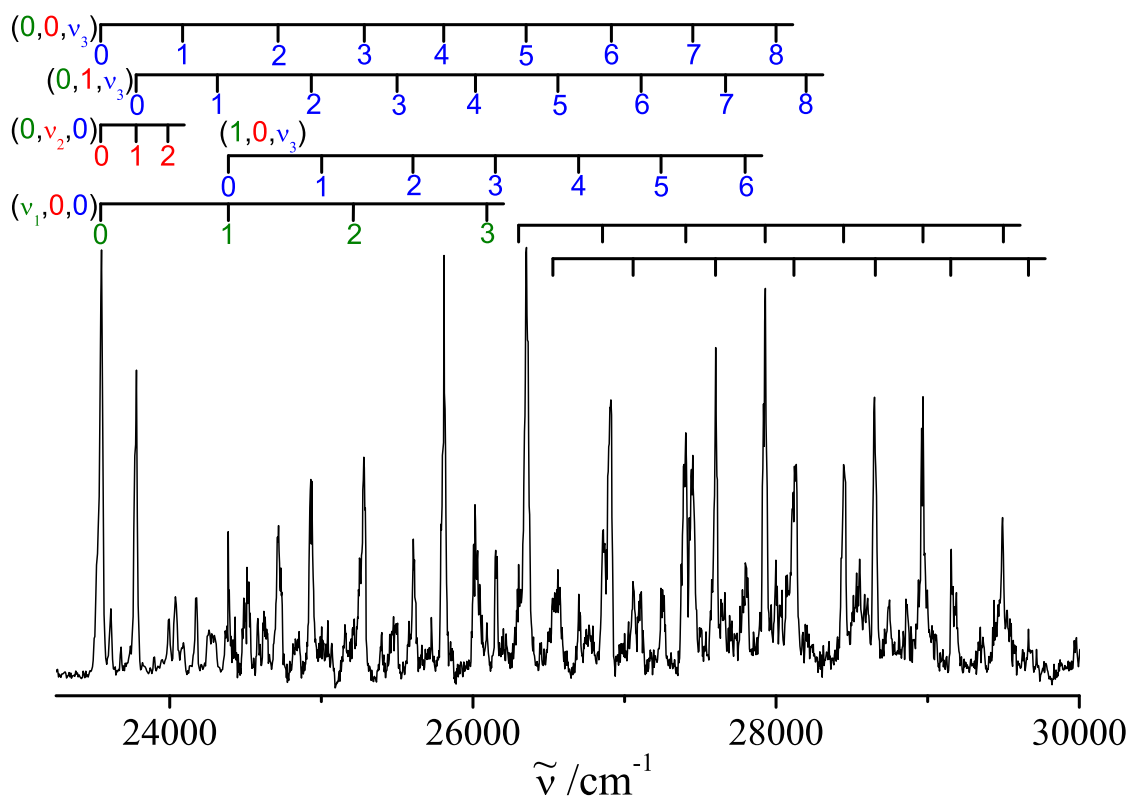


Figure 6.5: Assignment for the  $B^1A_1(\nu_1, \nu_2, \nu_3) - X^1A_1(0, 0, 0)$  electronic transition of  $^{90}\text{Zr}^{16}\text{O}_2$ .

Table 6.4: Band maxima (in  $\text{cm}^{-1}$ ) for the  $G^1B_2(\nu_1, \nu_2, \nu_3) - X^1A_1(0, 0, 0)$  electronic transition of  $^{90}\text{Zr}^{16}\text{O}_2$ .

Assignment $\nu_1, \nu_2, \nu_3$	Observed wavenumber	Offset <sup>a</sup>	Assignment $\nu_1, \nu_2, \nu_3$	Observed wavenumber	Offset <sup>a</sup>
0,0,0	30 727	0	0,0,3	33 103	2 376
0,0,1	31 517	790	0,0,4	33 865	3 138
0,0,2	32 311	1 584	0,0,5	34 634	3 907

<sup>a</sup> Shift from the 30 727  $\text{cm}^{-1}$  band.

## 6.3 Conclusion

Electronic transitions of  $\text{ZrO}_2$  in the visible and UV regions have been detected and analysed. The  $A^1B_2 - X^1A_1$  transition has origin band at 17 041  $\text{cm}^{-1}$  and

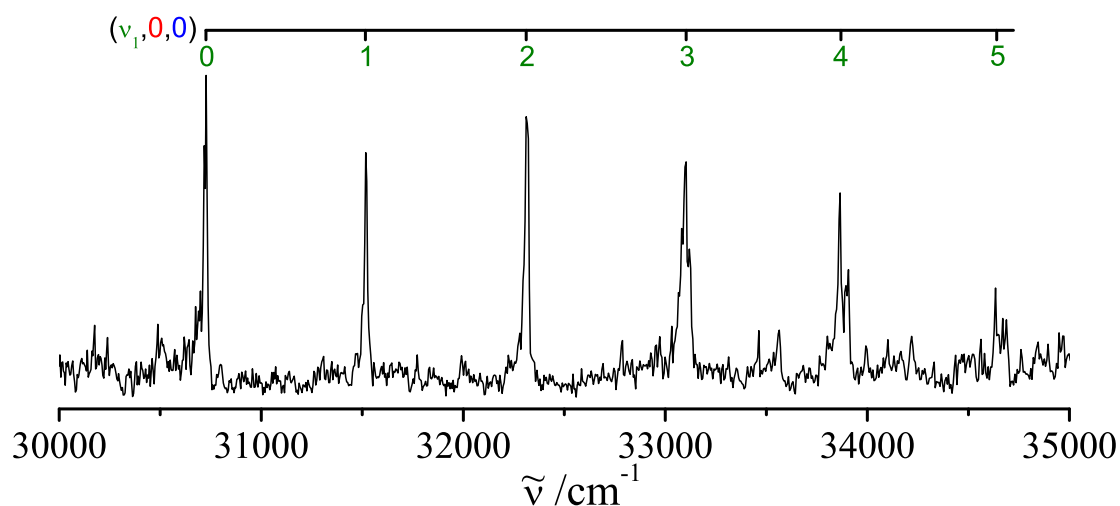


Figure 6.6: Assignment for the  $G^1B_2(\nu_1, \nu_2, \nu_3) - X^1A_1(0, 0, 0)$  electronic transition of  $^{90}\text{Zr}^{16}\text{O}_2$ .

the vibrational frequencies for the  $A^1B_2$  state are determined as  $\omega_1 = 819(3) \text{ cm}^{-1}$ ,  $\omega_2 = 149(3) \text{ cm}^{-1}$  and  $\omega_3 = 518(4) \text{ cm}^{-1}$ . The observation of odd  $\nu_3$  quanta transitions in the spectrum provide evidence of vibronic coupling. The precisely determined vibrational frequencies and term energies are a benchmark for future electronic structure calculations. The spectrum in the UV region indicate transitions arising from many different electronic levels. Band origins have been identified for two electronic systems at  $23550 \text{ cm}^{-1}$  and  $30727 \text{ cm}^{-1}$  and these are tentatively assigned to  $B^1A_1 - X^1A_1$  and  $G^1B_2 - X^1A_1$  transitions based on ab initio calculations [8].

# Bibliography

- [1] M. Kaufman, J. Muentner, and W. Klemperer. Geometry of some refractory metal dioxides. *Journal of Chemical Physics*, 47:3365–3366, 1967.
- [2] G. V. Chertihin and L. Andrews. Reactions of laser ablated titanium, zirconium, and hafnium atoms with oxygen molecules in condensing argon. *Journal of Physical Chemistry*, 99:6356–6366, 1995.
- [3] D. J. Brugh, R. D. Suenram, and W. J. Stevens. Fourier transform microwave spectroscopy of jet-cooled  $\text{ZrO}_2$  produced by laser vaporization. *Journal of Chemical Physics*, 111:3526–3535, 1999.
- [4] W. Zheng, K. H. Bowen Jr., J. Li, I. Dąbkowska, and M. Gutowski. Electronic structure differences in  $\text{ZrO}_2$  vs  $\text{HfO}_2$ . *Journal of Physical Chemistry A*, 109:11521–11525, 2005.
- [5] D. K. W. Mok, F. Chau, J. M. Dyke, and E. P. F. Lee. A combined ab initio and Franck–Condon simulation study of the photodetachment spectrum of  $\text{ZrO}_2^-$ . *Chemical Physics Letters*, 458:11–14, 2008.
- [6] S. Li and D. A. Dixon. Molecular structures and energetics of the  $(\text{ZrO}_2)_n$  and  $(\text{HfO}_2)_n$  ( $n = 1 - 4$ ) clusters and their anions. *Journal of Physical Chemistry A*, 114:2665–2683, 2010.
- [7] A. Le, T. C. Steimle, V. Gupta, C. A. Rice, J. P. Maier, S. H. Lin, and C. K. Lin. The visible spectrum of zirconium dioxide,  $\text{ZrO}_2$ . *Journal of Chemical Physics*, 135:104303:1–11, 2011.



- [8] C. K. Lin. Calculated geometric and energetic data and simulated absorption spectrum of  $\text{ZrO}_2$  molecule. private communication, 2012.
- [9] T. C. Steimle. Rotational analysis of the  $A^1B_2 - X^1A_1$  transition of  $\text{ZrO}_2$ . private communication, 2011.

# 7 Silicon Trimer

There have been numerous theoretical studies to investigate the structure and properties of silicon trimer [1–9]. Ab initio calculations [1–6] indicate that  $\text{Si}_3$  is strongly bent with two close lying electronic states:  ${}^1\text{A}_1(\text{C}_{2v})$  and  ${}^3\text{A}'_2(\text{D}_{3h})$ .  ${}^1\text{A}_1(\text{C}_{2v})$  is predicted to be the ground state with  ${}^3\text{A}'_2(\text{D}_{3h})$  state lying within 0.05 eV.

The ground state electronic configuration of  $\text{Si}_3$  in the high symmetry  $\text{D}_{3h}$  geometry is  $(5a'_1)^2(2a''_2)^2(6e')^2(2e'')^0$  [9].  $e' \otimes e'$  results in electronic states:  ${}^3\text{A}'_2$ ,  ${}^1\text{A}'_1$  and  ${}^1\text{E}'$ ; amongst which the triplet  ${}^3\text{A}'_2$  has been calculated [8,9] to be the ground state in  $\text{D}_{3h}$  geometry. Theory predicts a very small Jahn-Teller effect (JTE) [10] in the  ${}^1\text{E}'$  state, but a strong pseudo-JTE (PJTE) [10] between the singlets  ${}^1\text{A}'_1$  and  ${}^1\text{E}'$  [8]. Because of this strong PJT coupling, the  ${}^1\text{A}'_1$  component of the  ${}^1\text{E}'$  term is stabilized and crosses the undistorted ground  ${}^3\text{A}'_2$  state to produce the global minimum with a  $\text{C}_{2v}$  geometry [8].

The first experimental insight into the electronic structure of  $\text{Si}_3$  was provided by low resolution ( $\sim 1000 \text{ cm}^{-1}$ ) photoelectron spectroscopy (PES) of  $\text{Si}_3$  [11]. However, this resolution was not sufficient to discern any vibrational information from the electronic bands. This information was partially obtained by subsequent PES measurements [12,13] at a much better resolution of  $\sim 80 \text{ cm}^{-1}$ . A laser energy of 4.6 eV was sufficient to access six electronic states of  $\text{Si}_3$  [13]. The lowest energy band, corresponding to the ground electronic state of  $\text{Si}_3$  had a complex profile and it was proposed to result from a convolution of features from the  ${}^1\text{A}_1(\text{C}_{2v})$  and  ${}^3\text{A}'_2(\text{D}_{3h})$  states, which was supported by an ab initio study of the  $\text{Si}_3^-$  PES [6]. This band was vibrationally resolved by near threshold photodetachment zero-electron kinetic energy (ZEKE) spectroscopy of  $\text{Si}_3^-$  [14]. It was

assigned to transitions from the JT distorted anion to the  $D_{3h}$  neutral and the frequencies of the symmetric stretch ( $a_1'$ ) and degenerate ( $e'$ ) modes in the  ${}^3A_2'$  state were determined as  $501 \pm 10 \text{ cm}^{-1}$  and  $337 \pm 10 \text{ cm}^{-1}$ , respectively, in good agreement with the earlier calculated values [15, 16]. The transitions to the singlet state were very weak in the ZEKE spectrum which was attributed to a small photodetachment cross section for the  ${}^1A_1(C_{2v})$  state near the detachment threshold. A recent high level ab initio simulation of the PES confirmed that the major contribution to the lowest energy band of  $\text{Si}_3$  is from the  ${}^3A_2'$  electronic state [9].

The infrared absorption spectrum of the  $C_{2v}$  isomer of  $\text{Si}_3$  was first recorded in rare gas matrices and vibrational frequencies were determined as approximately  $550 \text{ cm}^{-1}$  and  $525 \text{ cm}^{-1}$ , in agreement with the calculated values for the symmetric ( $a_1$ ) and asymmetric ( $b_2$ ) stretching modes, respectively [17]. In another study involving neon matrices [18], four electronic transitions of  $\text{Si}_3$  were observed: one in the near-IR, two in the visible and one in the UV. All of them were assigned to the  $C_{2v}$  form with  ${}^1A_1$  state as the lower energy terminus. The origin of the near-IR and UV bands were identified at  $12\,839 \text{ cm}^{-1}$  and  $25\,753 \text{ cm}^{-1}$ , respectively. In the visible, the more intense system with an origin at  $17\,250 \text{ cm}^{-1}$  and a vibrational spacing ( $\nu_2$ ) of  $230\text{--}280 \text{ cm}^{-1}$  was assigned to the  ${}^1A_1 - {}^1A_1$  transition. A progression in a  $\sim 360 \text{ cm}^{-1}$  vibrational mode was observed in the case of second system which was assigned to the  ${}^1B_1 - {}^1A_1$  transition, but the origin could not be definitively identified. The band at  $19\,146 \text{ cm}^{-1}$  was tentatively assigned as the origin. Recently, the rotational spectrum of the  $C_{2v}$  form was recorded and analysed to obtain a Si–Si bond length of  $217.7 \pm 0.1 \text{ pm}$  and an apex angle of  $78.10^\circ \pm 0.03^\circ$  [19]. The frequency for the bend mode,  $\nu_2$  was estimated as  $178 \pm 11 \text{ cm}^{-1}$  using inertial defect.

## 7.1 Experimental

The experimental set-up is described in Chapter 3. A molecular beam of  $\text{Si}_3$  was generated by laser ablation of a silicon rod in the presence of a supersonically

expanding helium. Since the ionization potential of  $\text{Si}_3$  is  $\sim 8.50$  eV [20], ArF excimer laser (6.42 eV) is used for ionization.

## 7.2 Results and discussion

Figure 7.1 shows the mass selected [1+1'] resonant enhanced multi-photon ionization (REMPI) spectrum of  $^{28}\text{Si}_3$ . At least three overlapping progressions are visible: a stronger band system with an origin near  $18\,600\text{ cm}^{-1}$  and a spacing of  $\sim 445\text{ cm}^{-1}$ , and two weaker ones with spacings of  $\sim 280\text{ cm}^{-1}$  and  $\sim 350\text{ cm}^{-1}$ , lying to the red and the blue of  $18\,600\text{ cm}^{-1}$  band, respectively.

Ab initio calculations predict that all electronic transitions in the  $17\,000\text{ cm}^{-1}$  to  $22\,000\text{ cm}^{-1}$  region correspond to promotion of an electron from the  $6e'$  to the  $2e''$  orbital [21]. The possible lower electronic states are  ${}^3A_2'$ ,  ${}^1A_1'$  and  ${}^1E'$ , whereas both the singlets and triplets of  $A_1''$ ,  $A_2''$  and  $E''$  are possible for the upper state.

### 7.2.1 The triplet $D_{3h}$ system

In the triplet manifold, the transitions corresponding to promotion of electron from  $6e'$  to  $2e''$  orbital have  ${}^3A_2'$  lower state. Although,  ${}^3A_1''$ ,  ${}^3A_2''$  and  ${}^3E''$  upper states are possible for this electronic excitation,  ${}^3A_1'' - {}^3A_2'$  is the only dipole allowed process available to the triplet.

Ab initio calculations using the equation-of-motion coupled-cluster (EOM-CCSD) approach predict  ${}^3A_1'' - {}^3A_2'$  transition at 2.34 eV [21]. For the  ${}^3A_2'$  state, the calculated CCSD/cc-pwCTZ equilibrium structure has an Si–Si bond length of 228.0 pm which increases to 229.4 pm in the  ${}^3A_1''$  state [21]. Unlike many of the states in the singlet manifold, neither triplet state is JT active. The  ${}^3A_1'' - {}^3A_2'$  transition is expected to have a simple spectrum consisting only of a short progression in the symmetric stretch as the degenerate mode,  $\nu_2$ , is Franck-Condon inactive.

The features at  $18\,600\text{ cm}^{-1}$ ,  $19\,045\text{ cm}^{-1}$  and  $19\,507\text{ cm}^{-1}$ , which form a progression in  $\sim 445\text{ cm}^{-1}$ , each have a band to the red, shifted by approximately

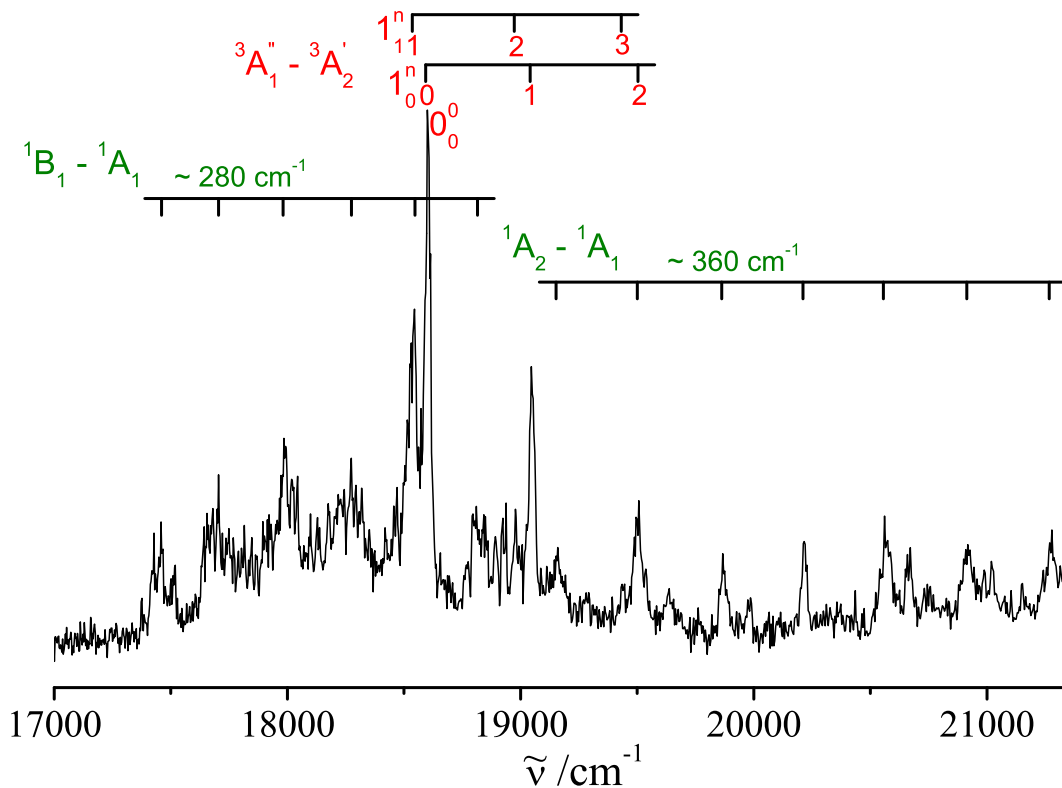


Figure 7.1: Mass-selected  $[1+1']$  resonance enhanced multi-photon ionization spectrum of  $\text{Si}_3$  in the  $17000 - 21500 \text{ cm}^{-1}$  region.

$60 \text{ cm}^{-1}$ . Assigning these red-shifted features as sequence bands of the  $445 \text{ cm}^{-1}$  progression yields a lower state frequency of  $\sim 505 \text{ cm}^{-1}$ , which is in excellent agreement with  $501 \pm 10 \text{ cm}^{-1}$  observed by ZEKE for the symmetric stretch ( $\nu_1$ ) of the  $D_{3h}$   ${}^3A_2'$  state [14]. The frequency for the symmetric stretch mode of the  ${}^3A_1'$  state was calculated as  $480 \text{ cm}^{-1}$  [21] which is quite close to the observed value of  $\sim 445 \text{ cm}^{-1}$ . Based on these agreements, the assignment of the  $\sim 445 \text{ cm}^{-1}$  progression to the  ${}^3A_1' - {}^3A_2'$  transition is secured. All the observed triplet bands have been marked in Figure 7.1 and the transition frequencies and assignments are listed in Table 7.1.

Table 7.1: Band maxima (in  $\text{cm}^{-1}$ ) for the  ${}^3A_1'' - {}^3A_2'$  electronic transition of  ${}^{28}\text{Si}_3$ .

Assignment	Observed wavenumber	Offset <sup>a</sup>	Assignment	Observed wavenumber	Offset <sup>a</sup>
$1_1^1$	18 534	-66	$1_0^1$	19 045	445
$0_0^0$	18 600	0	$1_1^3$	19 430	830
$1_1^2$	18 986	386	$1_0^2$	19 507	907

<sup>a</sup> Shift from the  $18\,600\text{ cm}^{-1}$  band.

### 7.2.2 The singlet $D_{3h}/C_{2v}$ system

Unlike the triplet manifold, in the singlet manifold there are number of possible transitions corresponding to promotion of electron from  $6e'$  to  $2e''$  orbital, all of which are strongly affected by the JT and PJT mechanisms [21]. In terms of  $D_{3h}$  symmetry, these are the  ${}^1A_2'' - {}^1A_1'$  and  ${}^1E'' - {}^1E'$  transitions.

Ab initio calculations predict a  ${}^1E'$  as the least energetic state arising from the ground electronic configuration, with a  ${}^1A_1'$  state lying  $0.23\text{ eV}$  above it [8,9]. The transition moment for the  ${}^1A_2'' - {}^1A_1'$  transition has been calculated to be  $\sim 1000$  times smaller than that of  ${}^1E'' - {}^1E'$  [22]. Thus,  ${}^1A_1'$  can be rejected as the lower state and the observed singlet system can be assigned to the  ${}^1E'' - {}^1E'$  transition in  $D_{3h}$  geometry, which correlates to  ${}^1B_1 - {}^1A_1$  and dark  ${}^1A_2 - {}^1A_1$  transitions from the JT distorted  $C_{2v}$  state.

In Figure 7.1 it can be seen that there is a system of broad features with  $\sim 280\text{ cm}^{-1}$  spacing to the red of triplet origin and another one with an interval of  $\sim 350\text{ cm}^{-1}$  towards the blue. These progressions start from the bands at  $17\,458\text{ cm}^{-1}$  and  $19\,159\text{ cm}^{-1}$ , respectively.

The observed gas phase  $[1+1']$  REMPI spectrum for the singlet manifold is distinctly similar to the neon matrix spectrum [18] (Figure 7.2), where two band systems from the  $C_{2v}$  singlet ground state were observed in this region. In the matrix study, one of the systems was assigned to the  ${}^1A_1 - {}^1A_1$  transition with an origin at  $17\,250\text{ cm}^{-1}$  and a  $230\text{--}280\text{ cm}^{-1}$  progression in the  $\nu_2$  mode. The second

system, with  $\sim 360 \text{ cm}^{-1}$  progression was assigned to the  ${}^1\text{B}_1 - {}^1\text{A}_1$  transition; the origin was tentatively assigned to the band at  $19\,146 \text{ cm}^{-1}$ .

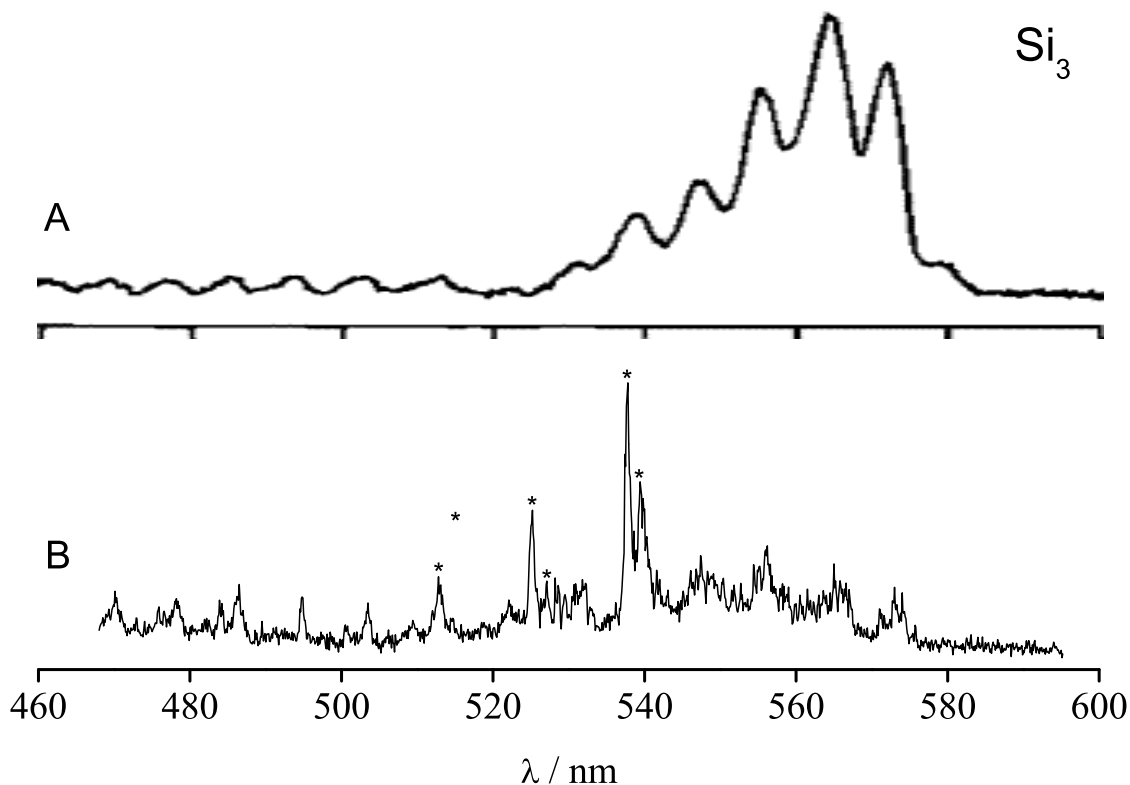


Figure 7.2: The  ${}^1\text{B}_1 - {}^1\text{A}_1$  and  ${}^1\text{A}_2 - {}^1\text{A}_1$  transition of  $\text{Si}_3$  in  $\text{C}_{2v}$  geometry, observed in (A) neon matrix [18]; (B) gas phase. The triplet transitions in gas phase spectrum are marked with an asterisk (\*).

Based on the recent theoretical studies [22] which take into account the JT and PJT interactions, the assignment of the singlet bands to  ${}^1\text{A}_1 - {}^1\text{A}_1$  and  ${}^1\text{B}_1 - {}^1\text{A}_1$  transitions in the previous neon matrix study [18] seems incorrect. Therefore, these singlet features are being re-assigned to the  ${}^1\text{B}_1 - {}^1\text{A}_1$  and  ${}^1\text{A}_2 - {}^1\text{A}_1$  transitions, respectively, arising from the JT distorted  $\text{C}_{2v}$  geometry; the symmetry forbidden  ${}^1\text{A}_2 - {}^1\text{A}_1$  transition becomes allowed due to strong vibronic coupling as a result of JT and PJT interactions. In view of absence of any band towards lower energy, the origin of the  ${}^1\text{B}_1 - {}^1\text{A}_1$  transition is tentatively assigned to the band

Table 7.2: Band maxima (in  $\text{cm}^{-1}$ ) for transitions of  $\text{Si}_3$  observed in the singlet manifold.

${}^1\text{B}_1 - {}^1\text{A}_1$		${}^1\text{A}_2 - {}^1\text{A}_1$	
Observed wavenumber	Offset <sup>a</sup>	Observed wavenumber	Offset <sup>b</sup>
17 428	0	19 159	0
17 705	277	19 507 <sup>c</sup>	348
17 985	557	19 867	708
18 274	846	20 216	1 057
18 545 <sup>c</sup>	1 117	20 561	1 402
18 810	1 382	20 918	1 759
		21 278	2 119

<sup>a</sup> Shift from the 17 428  $\text{cm}^{-1}$  band.

<sup>b</sup> Shift from the 19 159  $\text{cm}^{-1}$  band.

<sup>c</sup> Overlap with a triplet band.

at 17 428  $\text{cm}^{-1}$ . The transition frequencies of the bands in the singlet manifold are given in Table 7.2.

## 7.3 Conclusion

The gas phase electronic spectrum of  $\text{Si}_3$  has been recorded in the 17 000  $\text{cm}^{-1}$  to 22 000  $\text{cm}^{-1}$  region. In the spectrum, transitions arising from both, triplet  $\text{D}_{3h}$  and singlet  $\text{C}_{2v}$  isomers could be observed. In the triplet manifold, a progression in  $\sim 445 \text{ cm}^{-1}$  interval with origin at 18 600  $\text{cm}^{-1}$  is assigned to the  ${}^3\text{A}'_1 - {}^3\text{A}'_2$  transition. The singlet spectrum is much more complicated due to JT and PJT interactions. The observed features are assigned to  ${}^1\text{B}_1 - {}^1\text{A}_1$  and dark  ${}^1\text{A}_2 - {}^1\text{A}_1$  transitions from the JT distorted  $\text{C}_{2v}$  geometry, based on the current theoretical knowledge. However, more work is required to completely understand the singlet manifold of  $\text{Si}_3$ .





# Bibliography

- [1] K. Raghavachari. Theoretical study of small silicon clusters: cyclic ground state structure of  $\text{Si}_3$ . *Journal of Chemical Physics*, 83:3520–3525, 1985.
- [2] R. S. Grev and H. F. Schaefer. The ground state of  $\text{Si}_3$ , two near degenerate isomers. *Chemical Physics Letters*, 119:111–118, 1985.
- [3] K. Raghavachari and V. Logovinsky. Structure and bonding in small silicon clusters. *Physical Review Letters*, 55:2853–2856, 1985.
- [4] K. Raghavachari. Theoretical study of small silicon clusters: Equilibrium geometries and electronic structures of  $\text{Si}_n$  ( $n = 2-7, 10$ ). *Journal of Chemical Physics*, 84:5672–5686, 1986.
- [5] K. Balasubramanian. CAS SCF/CI calculations of low-lying states and potential energy surfaces of  $\text{Si}_3$ . *Chemical Physics Letters*, 125:400–406, 1986.
- [6] C. M. Rohlfing and K. Raghavachari. Electronic structures and photoelectron spectra of  $\text{Si}_3^-$  and  $\text{Si}_4^-$ . *Journal of Chemical Physics*, 96:2114–2117, 1992.
- [7] J. A. Hayward-Sudarko, J. M. Hughes, E. I. von Nagy-Felsobuki, and L. P. Alderidge. Rovibrational states of the  $^1A_1$  ground electronic state of  $\text{Si}_3$ . *Molecular Physics*, 92:177–186, 1997.
- [8] P. Garcia-Fernandez, I. B. Bersuker, and J. E. Boggs. Orbital disproportionation and spin crossover as a pseudo Jahn-Teller effect. *Journal of Chemical Physics*, 125:104102:1–11, 2006.

- [9] P. Garcia-Fernandez, J. E. Boggs, and J. F. Stanton. Ab initio simulation of the vibrationally resolved photoelectron spectrum of  $\text{Si}_3^-$ . *Journal of Chemical Physics*, 126:74305:1–6, 2007.
- [10] I. B. Bersuker. *The Jahn-Teller Effect*. Cambridge University Press, Cambridge, 2006.
- [11] O. Cheshnovsky, S. H. Yang, M. J. Craycraft, Y. Liu, and R. E. Smalley. Ultraviolet photoelectron spectroscopy of semiconductor clusters: silicon and germanium. *Chemical Physics Letters*, 138:119–124, 1987.
- [12] T. N. Kitsopoulos, C. J. Chick, A. Weaver, and D. M. Neumark. Vibrationally resolved photoelectron spectra of  $\text{Si}_3^-$  and  $\text{Si}_4^-$ . *Journal of Chemical Physics*, 93:6108–6110, 1990.
- [13] C. Xu, T. R. Taylor, G. R. Burton, and D. M. Neumark. Vibrationally resolved photoelectron spectroscopy of silicon cluster anions  $\text{Si}_n^-$  ( $n = 3 - 7$ ). *Journal of Chemical Physics*, 108:1395–1406, 1998.
- [14] C. C. Arnold and D. M. Neumark. Threshold photodetachment zero-electron kinetic energy spectroscopy of  $\text{Si}_3^-$ . *Journal of Chemical Physics*, 100:1797–1804, 1994.
- [15] D. A. Dixon and J. L. Gole. The electronic structure of  $\text{Si}_3$  and  $\text{Ge}_3$  in the local density functional approximation. *Chemical Physics Letters*, 188:560–564, 1992.
- [16] R. Fournier, S. B. Sinnott, and A. E. DePristo. Density functional study of the bonding in small silicon clusters. *Journal of Chemical Physics*, 97:4149–4161, 1992.
- [17] S. Li, R. J. Van Zee, W. Weltner Jr., and K. Raghavachari.  $\text{Si}_3 - \text{Si}_7$ . Experimental and theoretical infrared spectra. *Chemical Physics Letters*, 243:275–280, 1995.

- [18] J. Fulara, P. Freivogel, M. Grutter, and J. P. Maier. Electronic absorption spectra of  $\text{Si}_n$  and  $\text{Si}_n^-$  ( $n = 2 - 4$ ) in neon matrices. *Journal of Physical Chemistry*, 100:18042–18047, 1996.
- [19] M. C. McCarthy and P. Thaddeus. Rotational spectrum and structure of  $\text{Si}_3$ . *Physical Review Letters*, 90:213003: 1–4, 2003.
- [20] K. Fuke, K. Tsukanoto, F. Misaizu, and M. Sanekata. Near threshold photoionization of silicon clusters in the 248–146 nm region: Ionization potentials for  $\text{Si}_n$ . *Journal of Chemical Physics*, 99:7807–7812, 1993.
- [21] N. J. Reilly, D. L. Kokkin, X. Zhuang, V. Gupta, R. Nagarajan, R. C. Fortenberry, J. P. Maier, T. C. Steimle, J. F. Stanton, and M. C. McCarthy. The electronic spectrum of  $\text{Si}_3$  I: Triplet  $D_{3h}$  system. *Journal of Chemical Physics*, 136:194307:1–7, 2012.
- [22] D. A. Matthews and J. F. Stanton. An ab initio model Hamiltonian for the  $e' \times e'$  and  $e' \times e''$  singlet states of  $\text{Si}_3$ . presented at the 67th Ohio State University International Symposium on Molecular Spectroscopy, Columbus, 2012.



## 8 Carbon chains, $C_n$ ( $n = 6 - 9$ )

The ground  $X^3\Sigma_g^-$  state of linear  $C_6$  and  $C_8$  was identified by ESR [1] and IR spectroscopy [2,3] in noble gas matrices and confirmed by high resolution gas phase IR measurements [4,5]. The  $(1)^3\Sigma_u^- - X^3\Sigma_g^-$  electronic transition for  $C_6$  and  $C_8$  was identified in solid neon with origin band at 511.3 and 639.8 nm, respectively [6]. An intense broad band and a weaker structured one towards slightly lower energy were observed in the neon matrix for both molecules in the UV [7]. The broad bands at 237.5 nm for  $C_6$  and 277.2 nm for  $C_8$  were assigned to the  $(2)^3\Sigma_u^- - X^3\Sigma_g^-$  electronic transition, whereas the vibrationally resolved system was considered to originate from  $^3\Pi_u - X^3\Sigma_g^-$ . Subsequent large-scale multi-reference configuration interaction calculations for  $C_6$  predict the  $^3\Sigma_u^- - X^3\Sigma_g^-$  transitions at 2.66 eV and 5.7 eV with oscillator strength  $f = 0.023$  and 2.8, respectively, and a  $^3\Pi_u - X^3\Sigma_g^-$  system at 4.9 eV ( $f = 0.03$ ) [8]. Both are consistent with the neon matrix measurements. These calculations give the lowest singlet state,  $(1)^1\Delta_g$  to lie only 0.17 eV above the  $X^3\Sigma_g^-$  ground state. The broad contour of the  $(2)^3\Sigma_u^- - X^3\Sigma_g^-$  electronic transition of  $C_6$  and  $C_8$  was identified in the gas phase using [1+1] resonance enhanced multiphoton ionization (REMPI) and dissociative hole-burning techniques [9].

Theoretical calculations predict the ground state of linear  $C_7$  and  $C_9$  to be  $^1\Sigma_g^+$ , which was confirmed by gas phase IR diode laser spectroscopy [10–13]. The first study on the excited electronic states of these molecules was performed in a neon matrix and led to the identification of the  $^1\Pi_u - X^1\Sigma_g^+$  electronic transition of  $C_7$  with origin band at 542.3 nm, and that of the  $^1\Sigma_u^+ - X^1\Sigma_g^+$  system of  $C_7$  and  $C_9$  at 252.8 and 295.0 nm, respectively [14]. These assignments agree with the calculated vertical excitation energy for the higher electronic states of  $C_7$  and

$C_9$  [15,16]. The  ${}^1\Sigma_u^+ - X^1\Sigma_g^+$  electronic transition of  $C_9$  was later observed in the gas phase by a dissociative hole-burning approach but escaped detection with the [1+1] REMPI method [9]. None of the electronic transitions of  $C_7$  have previously been identified in the gas phase.

## 8.1 Experimental

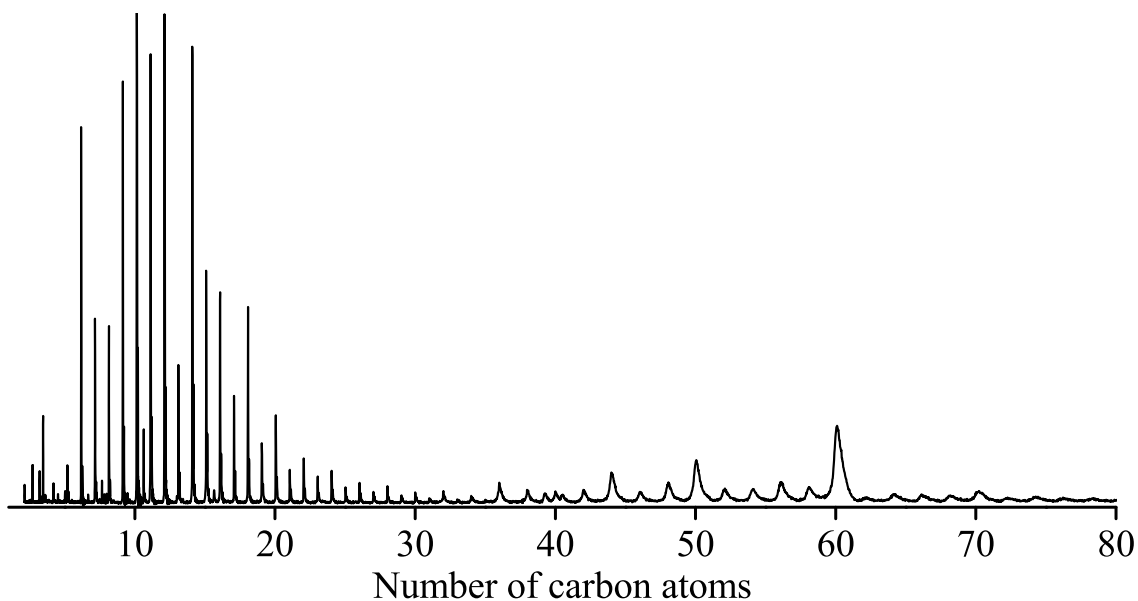


Figure 8.1: Time-of-flight mass spectrum of laser ablated graphite, recorded using a 10.5 eV ionization source.

The details of the experimental set-up are given in Chapter 3. A  $\sim 50$  mJ, 5 ns laser pulse from the second harmonic of  $\text{Nd}^{3+}:\text{YAG}$  was focussed to  $\sim 300$   $\mu\text{m}$ , onto a rotating and translating graphite rod and ablated carbon was co-expanded in the presence of helium at a backing pressure of 8 bar. A laser with 30 ps pulses, operating at 10 Hz repetition rate was used for all the experiments. The mass spectrum of the laser ablation products, recorded using 10.5 eV photons produced by tripling the 355 nm radiation in a Xe/Ar gas cell (Figure 8.1), allowing one photon ionization for species  $C_n$  ( $n \geq 6$ ). A [1+1] REMPI technique was applied

in the 210–310 nm range to record the spectra. For experiments involving [1+1] REMPI, the tunable UV wavelength excited the molecule and 266 nm was used for subsequent ionization.

## 8.2 Results and discussion

### 8.2.1 $(2)^3\Sigma_u^- - X^3\Sigma_g^-$ electronic transition of $C_6$ and $C_8$

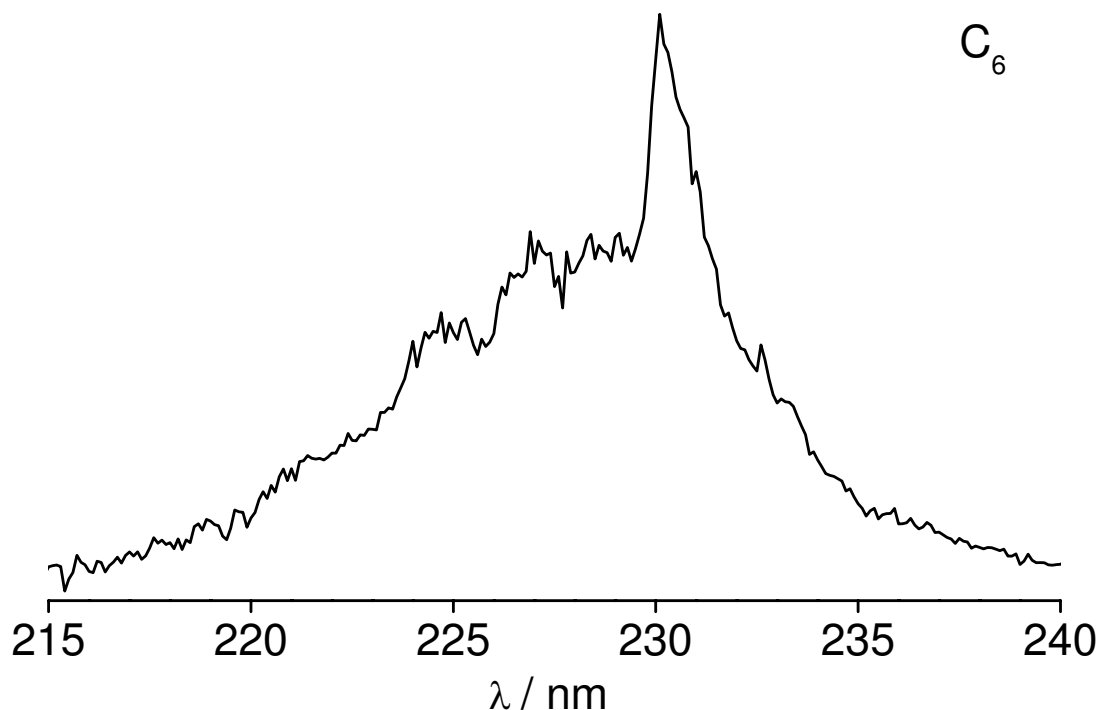


Figure 8.2:  $(2)^3\Sigma_u^- - X^3\Sigma_g^-$  electronic spectrum of linear  $C_6$  in the gas phase measured by [1+1] resonance enhanced multiphoton ionization method using 30 ps laser.

The  $(2)^3\Sigma_u^- - X^3\Sigma_g^-$  electronic spectrum of linear  $C_6$  recorded with the 30 ps laser using the [1+1] REMPI method is presented in Figure 8.2. It is similar to the one obtained earlier with a 10 ns laser [9]. A broad absorp-



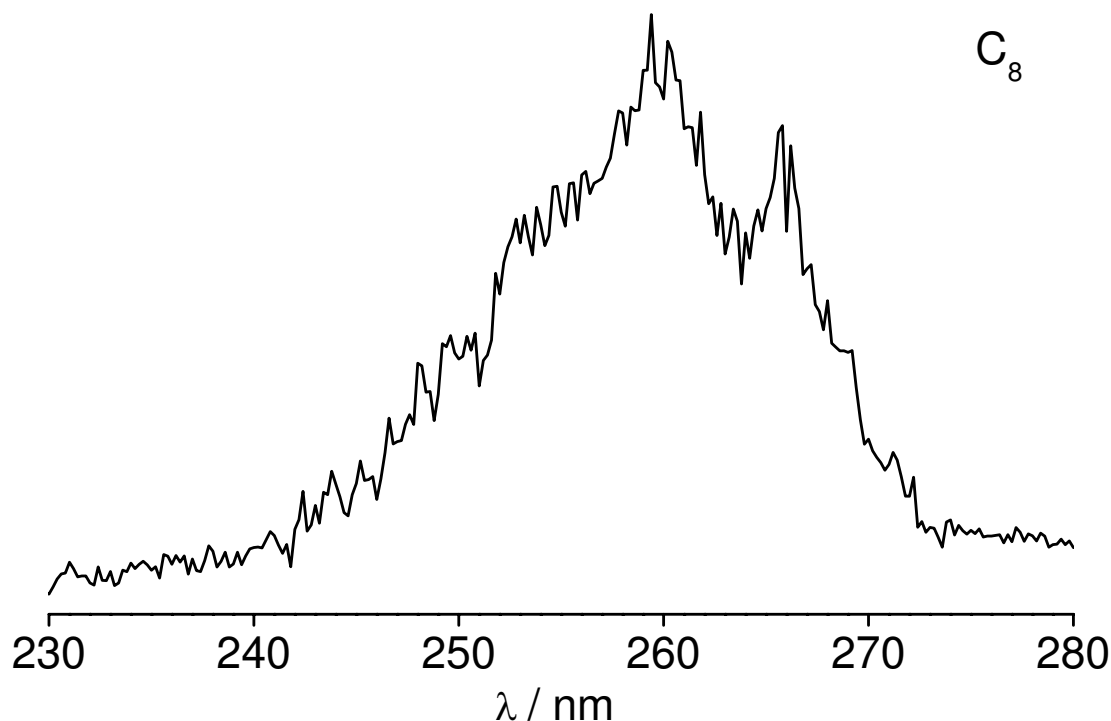


Figure 8.3:  $(2)^3\Sigma_u^- - X^3\Sigma_g^-$  electronic spectrum of linear  $C_8$  in the gas phase measured by [1+1] resonance enhanced multiphoton ionization method using a 30 ps laser.

tion with a maximum at 230.2 nm is observed, indicating a short-lived excited state due to fast internal conversion. Dissociation via the de-excitation channel has been proven by previous observation of the  $(2)^3\Sigma_u^- - X^3\Sigma_g^-$  transition using a dissociative hole burning technique [9]. A theoretical study on the photodynamics of linear  $C_6$  predicts the least energetic dissociation channel,  $C_6(X^3\Sigma_g^-) \rightarrow C_3(X^1\Sigma_g^+) + C_3(X^1\Sigma_g^+)$ , at  $\sim 3.50$  eV [23]. This is a spin forbidden process which can arise from the  $B^1\Sigma_g^+$  excited state of  $C_6$  ( $D_e \sim 3.16$  eV). However, the next pathway,  $C_6(X^3\Sigma_g^-) \rightarrow C_3(X^1\Sigma_g^+) + C_3(a^3\Pi_u)$ , at  $\sim 5.44$  eV is spin allowed. The molecule undergoes fast interconversion ( $<30$  ps, *vide infra*) from the  $(2)^3\Sigma_u^-$  excited state to highly excited vibrational levels of the ground

$X^3\Sigma_g^-$  electronic state, lying above the dissociation threshold and subsequently dissociates via  $C_3(X^1\Sigma_g^+) + C_3(a^3\Pi_u)$ .

A [1+1'] REMPI experiment was undertaken to determine the lifetime of the  $(2)^3\Sigma_u^-$  excited electronic state. A 30 ps, 266 nm radiation was used for ionization. The observed spectrum of  $C_6$  was similar to Figure 8.2. The excited-state lifetime was determined by setting the first photon at 230.2 nm, the band maxima of the  $(2)^3\Sigma_u^- - X^3\Sigma_g^-$  electronic transition, and then varying the temporal delay between the 230.2 and 266 nm photons. A decrease in the  $C_6^+$  signal intensity with delay was observed, which, however, was similar to the autocorrelation curve of both laser pulses. This indicates a  $(2)^3\Sigma_u^-$  lifetime of  $\leq 30$  ps.

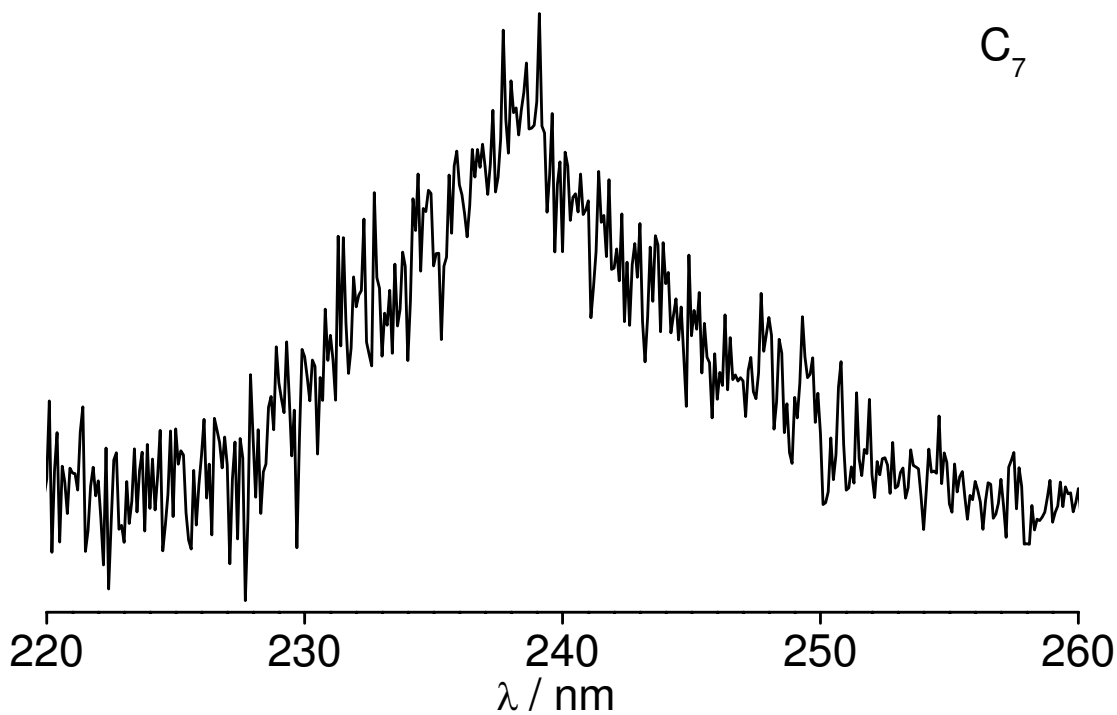


Figure 8.4:  ${}^1\Sigma_u^+ - X^1\Sigma_g^+$  electronic spectrum of linear  $C_7$  measured by [1+1] resonance enhanced multiphoton ionization method using a 30 ps laser.

Figure 8.3 presents the  $(2)^3\Sigma_u^- - X^3\Sigma_g^-$  electronic spectrum of linear  $C_8$  recorded with the 30 ps laser using the [1+1] REMPI method. As for  $C_6$ , the absorption has a rather broad contour indicating a lifetime of  $\leq 30$  ps for the  $(2)^3\Sigma_u^-$  electronic state.

### 8.2.2 $^1\Sigma_u^+ - X^1\Sigma_g^+$ electronic transition of $C_7$ and $C_9$

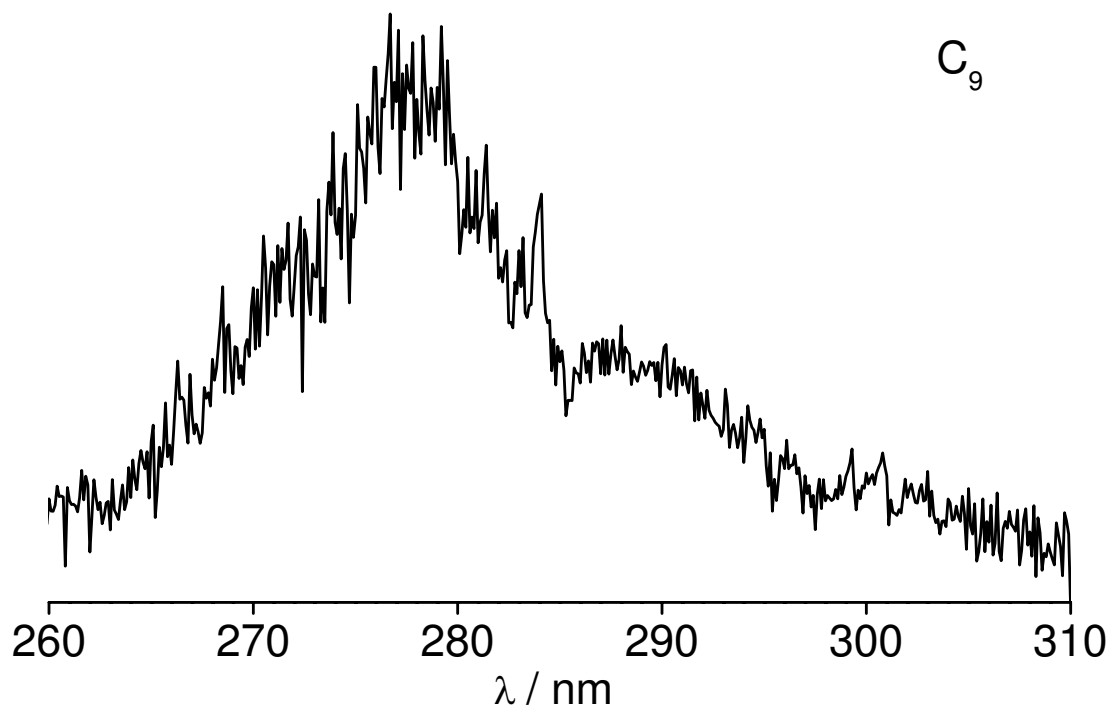


Figure 8.5:  $^1\Sigma_u^+ - X^1\Sigma_g^+$  electronic spectrum of linear  $C_9$  measured by [1+1] resonance enhanced multiphoton ionization method using a 30 ps laser.

The  $^1\Sigma_u^+ - X^1\Sigma_g^+$  transition (Figure 8.4) is the first electronic spectrum of linear  $C_7$  observed in the gas phase. There was an earlier attempt to record this spectrum, employing a ns laser, but it was unsuccessful [9]. It was assumed that the [1+1] REMPI spectrum could not be observed either because of inefficient production of linear  $C_7$  in the laser vaporization source or for energetic reasons as

two resonant photons might not be enough to ionize linear  $C_7$  or both. However, with the present observation of this transition, using a source similar to the one used in Ref. 9, both these reasons can be discarded. A more plausible explanation for previous non-observation is that the  $^1\Sigma_u^+$  excited state is short lived and the photon density within a 10 ns pulse was not high enough for a two-photon process to occur. This is consistent with the broad spectral contour observed with a ps laser indicating a fast decay from the excited state.

The ps [1+1] REMPI spectrum of the  $^1\Sigma_u^+ - X^1\Sigma_g^+$  electronic transition of linear  $C_9$  shows a broad contour (Figure 8.5), indicating a short lived excited state. The reason for non-detection of this transition earlier by a ns laser [9] is likely the same as in the case of  $C_7$ : initial fast internal conversion from the excited state.

### 8.3 Conclusion

The  $(2)^3\Sigma_u^- - X^3\Sigma_g^-$  electronic spectrum of  $C_6$  and  $C_8$  have been measured in the gas phase by mass-resolved [1+1] REMPI using a ps laser. The lifetime of the  $(2)^3\Sigma_u^-$  excited state of  $C_6$  is estimated to be  $< 30$  ps. Due to limitations of the experimental optics, a [1+1'] measurement could not be carried out for  $C_7$ ,  $C_8$  and  $C_9$ .



# Bibliography

- [1] R. J. Van Zee, R. F. Ferrante, K. J. Zeringue, and W. Weltner Jr. Electron spin resonance of the C<sub>6</sub>, C<sub>8</sub>, and C<sub>10</sub> molecules. *Journal of Chemical Physics*, 88:3465–3474, 1988.
- [2] R. H. Kranze and W. R. M. Graham. Fourier transform infrared isotopic study of the  $\nu_4$  and  $\nu_5$  stretching modes of linear C<sub>6</sub> in Ar at 10 K. *Journal of Chemical Physics*, 98:71–77, 1993.
- [3] P. Freivogel, M. Grutter, D. Forney, and J. P. Maier. Infrared bands of mass-selected carbon chains C<sub>n</sub> ( $n = 8 - 12$ ) and C<sub>n</sub><sup>-</sup> ( $n = 5 - 10, 12$ ) in neon matrices. *Chemical Physics*, 216:401–406, 1997.
- [4] H. J. Hwang, A. Van Orden, K. Tanaka, E. W. Kuo, T. R. Heath, and R. J. Saykally. Infrared laser spectroscopy of jet-cooled carbon clusters: structure of triplet C<sub>6</sub>. *Molecular Physics*, 79:769–776, 1993.
- [5] P. Neubauer-Guenther, T. F. Giesen, U. Berndt, G. Fuchs, and G. Winnewisser. The Cologne Carbon Cluster Experiment: ro-vibrational spectroscopy on C<sub>8</sub> and other small carbon clusters. *Spectrochimica Acta Part A: Molecular and Biomolecular Spectroscopy*, 59:431–441, 2003.
- [6] P. Freivogel, J. Fulara, M. Jakobi, D. Forney, and J. P. Maier. Electronic absorption spectra of linear carbon chains in neon matrices. II. C<sub>2n</sub><sup>-</sup>, C<sub>2n</sub>, and C<sub>2n</sub>H. *Journal of Chemical Physics*, 103:54–59, 1995.
- [7] M. Grutter, M. Wyss, E. Riaplov, J. P. Maier, S. D. Peyerimhoff, and M. Hanrath. Electronic absorption spectra of linear C<sub>6</sub>, C<sub>8</sub> and cyclic C<sub>10</sub>, C<sub>12</sub> in neon matrices. *Journal of Chemical Physics*, 111:7397–7401, 1999.

- [8] M. Hanrath, S. D. Peyerimhoff, and F. Grein. Theoretical studies on the electronic spectrum of linear  $C_6$ . *Chemical Physics*, 249:121–128, 1999.
- [9] A. E. Boguslavskiy and J. P. Maier. Gas phase electronic spectra of the carbon chains  $C_5$ ,  $C_6$ ,  $C_8$ , and  $C_9$ . *Journal of Chemical Physics*, 125:94308–1–7, 2006.
- [10] J. R. Heath, R. A. Sheeks, A. L. Cooksy, and R. J. Saykally. The  $C_7$  cluster: structure and infrared frequencies. *Science*, 249:895–897, 1990.
- [11] J. R. Heath, A. Van Orden, E. Kuo, and R. J. Saykally. The  $\nu_5$  band of  $C_7$ . *Chemical Physics Letters*, 182:17–20, 1991.
- [12] J. R. Heath and R. J. Saykally. The  $C_9$  cluster: structure and infrared frequencies. *Journal of Chemical Physics*, 93:8392–8394, 1990.
- [13] A. Van Orden, H. J. Hwang, E. W. Kuo, and R. J. Saykally. Infrared laser spectroscopy of jet-cooled carbon clusters: the bending dynamics of linear  $C_9$ . *Journal of Chemical Physics*, 98:6678–6683, 1993.
- [14] D. Forney, P. Freivogel, M. Grutter, and J. P. Maier. Electronic absorption spectra of linear carbon chains in neon matrices. IV.  $C_{2n+1}$   $n = 2–7$ . *Journal of Chemical Physics*, 104:4954–4960, 1996.
- [15] M. Kolbuszewski. Ab initio study of the optical spectra of  $C_3$ ,  $C_5$ , and  $C_7$  chains. *Journal of Chemical Physics*, 102:3679–3684, 1995.
- [16] M. Mühlhäusera, G. E. Froudakisb, and S. D. Peyerimhoff. MRD-CI study of the electronic spectrum of linear  $C_9$ . *Chemical Physics Letters*, 336:171–176, 2001.
- [17] C. C. Arnold, Y. Zhao, T. N. Kitsopoulos, and D. M. Neumark. Study of  $C_6^-$  and  $C_6$  with threshold photodetachment spectroscopy and autodetachment spectroscopy. *Journal of Chemical Physics*, 97:6121–6135, 1992.
- [18] C. Xu, G. R. Burton, T. R. Taylor, and D. M. Neumark. Photoelectron spectroscopy of  $C_4^-$ ,  $C_6^-$ , and  $C_8^-$ . *Journal of Chemical Physics*, 107:3428–3436, 1997.

- 
- [19] J. M. L. Martin and P. R. Taylor. Structure and vibrations of small carbon clusters from coupled-cluster calculations. *Journal of Physical Chemistry*, 100:6047–6056, 1996.
- [20] S. Schmatz and P. Botschwina. A theoretical investigation of four electronic states of  $C_6^-$  and the ground state of linear  $C_6$ . *Chemical Physics Letters*, 235:5–12, 1995.
- [21] J. M. L. Martin, J. El-Yazal, and J. P. François. Structure and vibrational spectra of carbon clusters  $C_n$  ( $n = 2 - 10, 12, 14, 16, 18$ ) using density functional theory including exact exchange contributions. *Chemical Physics Letters*, 242:570–579, 1995.
- [22] J. M. L. Martin, J. P. François, and R. Gijbels. Ab initio study of the infrared spectra of linear  $C_n$  ( $n = 6 - 9$ ). *Journal of Chemical Physics*, 93:8850–8861, 1990.
- [23] Z. Cao, M. Mühlhäusera, M. Hanrath, and S. D. Peyerimhoff. Study of possible photodissociation channels in linear carbon clusters  $C_n$  ( $n = 4 - 6$ ). *Chemical Physics Letters*, 351:327–334, 2002.
- [24] A. E. Douglas. Origin of diffuse interstellar lines. *Nature*, 269:130–132, 1977.
- [25] E. B. Jochnowitz and J. P. Maier. Electronic spectroscopy of carbon chains. *Annual Review of Physical Chemistry*, 59:519–544, 2008.





## 9 Conclusion

This work describes the experimental measurements and spectroscopic analysis of several transient molecules. These species were produced using pulsed laser ablation or electric discharge coupled with supersonic expansion and their electronic spectra were recorded using resonance enhanced multiphoton ionization (REMPI) technique coupled with time-of-flight (TOF). A combination of REMPI and TOF provides a powerful tool for unambiguous identification of the carrier of any spectral feature, with a particular mass signature.

Silver monosulfide has been spectroscopically characterized in the gas phase for the first time and electronic transitions were detected in the near-infrared and ultraviolet. Bands in the  $10\,000\text{ cm}^{-1}$  to  $11\,000\text{ cm}^{-1}$  region are assigned to the  $A^2\Sigma^+ - X^2\Pi_i$  electronic transition, based on a rotational analysis. The small change in the rotational constant between the  $X^2\Pi$  ground and  $A^2\Sigma^+$  excited states indicate only a small change in Ag–S bond length on electron promotion. This is consistent with the dominant Frank-Condon factor for the 0–0 transition in the vibronic spectra. The spin-orbit coupling constant for the ground state gives an insight into the contribution of various electronic configurations to bonding in AgS. In the UV, band origin and vibronic progressions have been identified for seven different systems. The lower energy terminus for all the UV transitions has been assigned to  $X^2\Pi$  ground state, but the excited electronic state can only be determined from rotational analysis of high resolution spectra. Efforts are under way to analyse overlapping band systems in the  $25\,500 - 26\,500\text{ cm}^{-1}$  region, for which high resolution spectra have been recorded.

Electronic spectra of transition metal dioxides,  $\text{TiO}_2$  and  $\text{ZrO}_2$  have been recorded in the visible and UV regions. The visible transition for both the

molecules has been assigned to  $A^1B_2 - X^1A_1$  electronic system. There are many similarities in their spectra, such as a significant decrease in  $\omega_2$  and  $\omega_3$  and a slight decrease in  $\omega_1$  upon excitation from the  $X^1A_1$  to  $A^1B_2$  state. Also, a long progression in both the cases are observed, suggesting a significant geometry change between the states. There is one striking difference, the observation of odd- $\nu_3$  quanta in the case of  $ZrO_2$ , which provides an evidence for vibronic coupling between  $A^1B_2$  state and the next higher state, due to a breakdown of Born-Oppenheimer approximation. The observed UV transitions for these molecules are distinct, suggesting a different electronic manifold in each case, as has been predicted by theory.

Silicon trimer provides another interesting case for a breakdown of the Born-Oppenheimer approximation. The ground state electronic configuration of  $Si_3$  in the high symmetry  $D_{3h}$  geometry is  $(5a_1')^2(2a_2'')^2(6e')^2$ , which gives rise to  $^3A_2'$ ,  $^1A_1'$  and  $^1E'$  lower states. According to calculations, and as predicted by Hund's rule,  $^3A_2'$  is the least energetic state. However, due to Jahn-Teller and pseudo Jahn-Teller effects, the  $^1A_1'$  component of the  $^1E'$  term is stabilized and crosses the undistorted  $^3A_2'$  ground state to produce a global minimum of  $C_{2v}$  geometry. The  $^3A_2'$  and  $^1A_1'$  are nearly iso-energetic and both get populated even under supersonic expansion conditions, complicating the spectrum in the  $17\,000\text{ cm}^{-1}$  to  $22\,000\text{ cm}^{-1}$  region. A progression of  $\sim 445\text{ cm}^{-1}$  interval with origin at  $18\,600\text{ cm}^{-1}$  is assigned to the  $^3A_1' - ^3A_2'$  transition. The transitions in the singlet manifold are more difficult to assign due to the presence of non-adiabatic effects. Based on the current theoretical knowledge, absorption features are assigned to  $^1B_1 - ^1A_1$  and dark  $^1A_2 - ^1A_1$  transitions from the JT distorted  $C_{2v}$  geometry, however, better understanding is required to fully understand the singlet manifold of  $Si_3$ .

UV electronic transitions of linear carbon chains,  $C_{6-9}$  were measured by [1+1] REMPI technique, using a picosecond laser; it is the first detection of an electronic transition of  $C_7$  in the gas phase. The  $(2)^3\Sigma_u^- - X^3\Sigma_g^-$  electronic spectra of  $C_6$  and  $C_8$ , and the  $^1\Sigma_u^+ - X^1\Sigma_g^+$  ones for  $C_7$  and  $C_9$  display broad contours, indicating an excited state lifetime less than the temporal width of the laser pulse (30 ps).

---

The intramolecular dynamics of the excited electronic states of the studied carbon chains are considered.

Spectroscopic measurements, other than providing information about the fundamental properties of molecules, can enrich the understanding of the universe. Laboratory data can be compared against the spectral lines from stars, comets, dust clouds, etc. to determine their composition and to understand the molecular chemistry taking place in these environments. TiO [1, 2] and ZrO [3, 4] have previously been detected in stellar atmospheres via their optical transitions; the presented gas phase spectra of TiO<sub>2</sub> and ZrO<sub>2</sub> provide a guide for optical detection of these molecules in stellar environments. Similarly, SiC<sub>2</sub> [5–7] and C<sub>3</sub> [8, 9] have been detected in molecular clouds by their electronic spectra, and the study of isovalent Si<sub>3</sub> has an astronomical interest.

Carbon chains have been considered as potential carriers of Diffuse Interstellar Bands (DIBs) [10]. Research on the electronic transitions of such chains in the laboratory and in comparison with astronomical data have led to the conclusion that the smaller carbon chains C<sub>n</sub> ( $n < 15$ ) can not be responsible for the stronger DIBs [11], as the oscillator strength and column densities considered in combination are insufficient for the species absorbing in the usual 400–900 nm DIB range. However, the concept of intramolecular broadening affects the absorption profiles, even for the smaller chains C<sub>n</sub> ( $n = 6 - 9$ ). This has been demonstrated in the study using a picosecond pump-probe technique. The internal conversion leads to ps lifetimes of the excited electronic states and corresponding broadened absorptions.

In summary, REMPI coupled with TOF has been successfully applied to spectroscopically characterise several transient molecules. In addition to giving an insight into the fundamental properties of studied molecules, the laboratory spectra provide a lead for their astronomical detection.



# Bibliography

- [1] W. W. Morgan, P. C. Keenan, and E. Kellman. *An atlas of stellar spectra with an outline of spectral classification*. University of Chicago Press, Chicago, U. S. A., 1943.
- [2] R. E. S. Clegg, D. L. Lambert, and R. A. Bell. Isotopes of titanium in cool stars. *Astrophysical Journal*, 234:188–199, 1979.
- [3] D. N. Davis. The spectrum of  $\beta$  pegasi. *Astrophysical Journal*, 106:28–75, 1947.
- [4] G. H. Herbig. Identification of a molecular band at  $\lambda$ 3682 in the spectra of late-type stars. *Astrophysical Journal*, 109:109–115, 1949.
- [5] P. W. Merrill. Note on the spectrum of UV Aurigæ. *Publications of the Astronomical Society of the Pacific*, 38:175–176, 1926.
- [6] R. F. Sanford. Two bands in spectra of class N. *Publications of the Astronomical Society of the Pacific*, 38:177–179, 1926.
- [7] B. Kleman. Laboratory excitation of the blue-green bands observed in the spectra of N-type stars. *Astrophysical Journal*, 123:162–165, 1956.
- [8] K. W. Hinkle, J. J. Keady, and P. F. Bernath. Detection of C<sub>3</sub> in the circumstellar shell of IRC+10216. *Science*, 241:1319–1322, 1988.
- [9] J. P. Maier, N. M. Lakin, G. A. H.Walker, and D. A. Bohlender. Detection of C<sub>3</sub> in diffuse interstellar clouds. *Astrophysical Journal*, 553:267–273, 2001.
- [10] A. E. Douglas. Origin of diffuse interstellar lines. *Nature*, 269:130–132, 1977.

- [11] E. B. Jochowitz and J. P. Maier. Electronic spectroscopy of carbon chains. *Annual Review of Physical Chemistry*, 59:519–544, 2008.

# Curriculum Vitae

## Personal Details

Name: Varun Gupta  
Born: May 31, 1986; Kanpur, India  
Nationality: Indian  
Contact: varunkg@gmail.com

## Education

10/2008 - 04/2013 Doctor of Philosophy in Physical Chemistry  
University of Basel, Switzerland  
Thesis: *Electronic spectroscopy of transient molecules by mass-selected resonance enhanced multi-photon ionization*  
Supervisor: *Prof. Dr. John P. Maier*

07/2003 - 06/2008 Master of Sciences (5 year integrated) in Photonics  
Cochin University of Science and Technology, India  
Thesis: *Laser ablated carbon plasma at low irradiance*  
Supervisor: *Prof. Dr. Raj K. Thareja*  
At: Indian Institute of Technology, Kanpur

## Teaching Experience

02/2009 - 01/2013 Undergraduate laboratory courses in Physical Chemistry  
University of Basel, Switzerland



## Peer Reviewed Publications

- **V. Gupta**, F. J. Mazzotti, C. A. Rice, R. Nagarajan, and J. P. Maier. The  $A^2\Sigma^+ - X^2\Pi_i$  electronic transition of AgS. *Journal of Molecular Spectroscopy*, 286–287:52–55, 2013.
- X. Chen, M. Steglich, **V. Gupta**, C. A. Rice, and J. P. Maier. Gas phase electronic spectroscopy of carbon chains,  $C_n$  ( $n = 6 - 9$ ). *Physical Chemistry Chemical Physics*, xx:xxx–xxx, 2013.
- N. J. Reilly, D. L. Kokkin, X. Zhuang, **V. Gupta**, R. Nagarajan, R. C. Fortenberry, J. P. Maier, T. C. Steimle, J. F. Stanton, and M. C. McCarthy. The electronic spectrum of  $Si_3$  I: Triplet  $D_{3h}$  system. *Journal of Chemical Physics*, 136:194307(1-7), 2012.
- A. Le, T. C. Steimle, **V. Gupta**, C. A. Rice, J. P. Maier, S. H. Lin, and C. -K. Lin. The visible spectrum of zirconium dioxide,  $ZrO_2$ . *Journal of Chemical Physics*, 135:104303(1-11), 2011.
- X. Zhuang, A. Le, T. C. Steimle, R. Nagarajan, **V. Gupta**, and J. P. Maier. Visible spectrum of titanium dioxide. *Physical Chemistry Chemical Physics*, 12:15018-15028, 2010.
- D. Yadav, **V. Gupta**, and R. K. Thareja. Evolution and imaging of nanoparticles observed in laser ablated carbon plume. *Journal of Applied Physics*, 106:64903(1-7), 2009.
- D. Yadav, **V. Gupta**, and R. K. Thareja. Ground state  $C_2$  density measurement in carbon plume using laser-induced fluorescence spectroscopy. *Spectrochimica Acta Part B*, 64: 986-992, 2009.